UNIVERSIDADE ESTADUAL DE CAMPINAS
Instituto de Física Gleb Wataghin

FRANCISCO MATEUS CIRILO DA SILVA

CORRELATIONS AMONG OPTICAL, STRUCTURAL AND MORPHOLOGICAL PROPERTIES OF HYBRID PEROVSKITES BY X-RAY NANOSCOPY WITH SYNCHROTRON LIGHT

CORRELAÇÕES ENTRE PROPRIEDADES ÓPTICAS, ESTRUTURAIS E MORFOLÓGICAS DE PEROVSKITAS HÍBRIDAS INVESTIGADAS POR NANOSCOPIAS DE RAIOS-X COM LUZ SÍNCROTRON

CAMPINAS
2024

FRANCISCO MATEUS CIRILO DA SILVA

CORRELATIONS AMONG OPTICAL, STRUCTURAL AND MORPHOLOGICAL PROPERTIES OF HYBRID PEROVSKITES BY X-RAY NANOSCOPY WITH SYNCHROTRON LIGHT

CORRELAÇÕES ENTRE PROPRIEDADES ÓPTICAS, ESTRUTURAIS E MORFOLÓGICAS DE PEROVSKITAS HÍBRIDAS INVESTIGADAS POR NANOSCOPIAS DE RAIOS-X COM LUZ SÍNCROTRON

Thesis presented to the Gleb Wataghin Institute of Physics of the University of Campinas in partial fulfillment of the requirements for the degree of DOCTOR IN SCIENCES, in the Area of APPLIED PHYSICS.

Tese apresentada ao Instituto de Física Gleb Wataghin da Universidade Estadual de Campinas como parte dos requisitos exigidos para a obtenção do título de DOUTOR EM CIÊNCIAS, na Área de FÍSICA APLICADA.

Supervisor: HELIO CESAR NOGUEIRA TOLENTINO
Co-supervisor: FRANCISCO DAS CHAGAS MARQUES

ESTE TRABALHO CORRESPONDE À VERSÃO FINAL DA TESE DEFENDIDA PELO ALUNO FRANCISCO MATEUS CIRILO DA SILVA E ORIENTADA PELO PROF. DR. HELIO CESAR NOGUEIRA TOLENTINO.

CAMPINAS
2024

Ficha catalográfica
Universidade Estadual de Campinas
Biblioteca do Instituto de Física Gleb Wataghin
Lucimeire de Oliveira Silva da Rocha - CRB 8/9174

Si38c

Silva, Francisco Mateus Cirilo da, 1994-
Correlations among optical, structural and morphological properties of hybrid perovskites by X-ray nanoscopy with synchrotron light / Francisco Mateus Cirilo da Silva. – Campinas, SP : [s.n.], 2024.

Orientador: Helio Cesar Nogueira Tolentino.
Coorientador: Francisco das Chagas Marques.
Tese (doutorado) – Universidade Estadual de Campinas, Instituto de Física Gleb Wataghin.

1. Síncrotron. 2. Perovskitas híbridas. 3. Imagens multiespectrais. 4. Pticografia. 5. Nanoscopia. I. Tolentino, Helio Cesar Nogueira. II. Marques, Francisco das Chagas, 1957-. III. Universidade Estadual de Campinas. Instituto de Física Gleb Wataghin. IV. Título.

Informações Complementares

Título em outro idioma: Correlações entre propriedades ópticas, estruturais e morfológicas de perovskitas híbridas investigadas por nanoscopias de raios-X com luz síncrotron
Palavras-chave em inglês:
Synchrotron
Hybrid perovskites
Multispectral imaging
Ptychography
Nanoscopy
Área de concentração: Física Aplicada
Titulação: Doutor em Ciências
Banca examinadora:
Helio Cesar Nogueira Tolentino [Orientador]
Mônica Alonso Cotta
Abner de Siervo
Maria Luiza Rocco Duarte Pereira
Florian Edouard Pierre Meneau
Data de defesa: 08-03-2024
Programa de Pós-Graduação: Física

Identificação e informações acadêmicas do(a) aluno(a)
- ORCID do autor: https://orcid.org/0000-0002-7054-2265
- Currículo Lattes do autor: http://lattes.cnpq.br/8438182437374888

MEMBROS DA COMISSÃO EXAMINADORA DA TESE DE DOUTORADO DO ALUNO FRANCISCO MATEUS CIRILO DA SILVA – RA 211788, APRESENTADA E APROVADA AO INSTITUTO DE FÍSICA GLEB WATAGHIN, DA UNIVERSIDADE ESTADUAL DE CAMPINAS, EM 08/03/2024.

COMISSÃO JULGADORA:

- Prof. Dr. Helio Cesar Nogueira Tolentino – Presidente e Orientador (Centro Nacional de Pesquisa em Energia e Materiais/Laboratório Nacional de Luz Síncrotron)

- Profa. Dra. Mônica Alonso Cotta (IFGW/ UNICAMP)

- Prof. Dr. Abner de Siervo (IFGW/ UNICAMP)

- Dr. Florian Edouard Pierre Meneau (Centro Nacional de Pesquisa em Energia e Materiais - Laboratório Nacional de Luz Síncrotron)

- Profa. Dra. Maria Luiza Rocco Duarte Pereira (Instituto de Química da Universidade Federal do Rio de Janeiro - UFRJ)

OBS.: Ata da defesa com as respectivas assinaturas dos membros encontra-se no SIGA/Sistema de Fluxo de Dissertação/Tese e na Secretaria do Programa da Unidade.

ESTE TRABALHO CORRESPONDE À VERSÃO FINAL DA TESE DEFENDIDA PELO ALUNO FRANCISCO MATEUS CIRILO DA SILVA E ORIENTADA PELO PROF. DR. HELIO CESAR NOGUEIRA TOLENTINO.

CAMPINAS
2024

Dedico esse trabalho a meu pai, minha mãe, meu irmão e minha irmã. Sem os quais nada disso seria possível e sequer teria sentido!

ACKNOWLEDGEMENTS

This work was carried out during the years 2020-2024 at the Brazilian Synchrotron Light Laboratory (LNLS), which is part of the Brazilian Center for Research in Energy and Materials (CNPEM), and at the “Gleb Wataghin” Institute of Physics (IFGW) of the University of Campinas (UNICAMP), both in Campinas/SP, Brazil.

I owe my most profound gratitude to my advisor, Helio Cesar Nogueira Tolentino. Without his continuous efforts concerning this work, the present study would hardly have been completed. His guidance into the coherent diffraction, synchrotron technology and methods of characterization his supervision in beamline experiments measurements and the discussions about scientific instrumentation also contributed to make this work complete.

I also want to express my warmest gratitude to my colleagues from LNLS, Maria Gabriella, Rodrigo Szostak, Carolina Camarda, Giovanni Lenzi, Itamar Neckel, Leonardo Kofukuda, Antonio Neto, Anna Paula, Verônica Teixeira, who were involved in some manner with the works I performed during this project.

I am deeply grateful to the group from the Nanotechnology and Solar Energy Laboratory which provide all the support and the guidance in the sample preparation. I acknowledge CNPEM, UNICAMP, and the founding agency, namely, CNPq - Conselho Nacional de Desenvolvimento Científico e Tecnológico.

The most special of all thanks to my girlfriend and best friend, Jéssica Diniz, for her assistance and friendship, for all the moments, for all her support and especially for everything that is yet to come. O mais especial de todos os obrigados à minha namorada e melhor amiga, Jéssica Diniz, pela assistência e amizade, por todos os momentos, por todo o apoio e principalmente por tudo que ainda está por vir.

And finally, for the absolute support and love, I owe my last and most important thanks to my parents, Francisco and Eni, my brother Rafael, and my sister Fabiane, because for sure they are the most important people in my life and without whom I would never be able to do nothing in my life. E por fim, pelo apoio e carinho absoluto, devo meu último e mais importante agradecimento aos meus pais, Francisco e Eni, ao meu irmão Rafael, e à minha irmã Fabiane, pois com certeza eles são as pessoas mais importantes da minha vida e sem os quais eu nunca teria sido capaz de realizar nada grande, pequeno, ou significativo na minha vida.

Compre pipoca só pra comer o queijinho!

(Povo taubateano)

ABSTRACT

Metal halide perovskite (MHP) compounds have emerged as promising candidates for next-generation optoelectronic devices, offering exceptional photovoltaic and light-emitting properties. The thesis explores hybrid organic-inorganic MHP thin films, employing cutting-edge multispectral synchrotron techniques to unveil micro-to-nanoscale heterogeneities and their relation to optoelectronic properties. The primary focus is manipulating cesium (Cs) content within the composition, a key variable impacting structural and optoelectronic characteristics. Through commissioning and developing advanced techniques such as X-ray ptychography, X-ray nanodiffraction, X-ray fluorescence, and X-ray Excited Optical Luminescence, the study aims to provide unprecedented insights into the intricate heterogeneity of hybrid perovskite thin films. A comprehensive investigation was conducted on $Cs_xFA_{1-x}Pb(Br_{0.38}I_{0.62})_3$ perovskite thin films, which exhibited a distinctive wrinkled morphology, deposited on Mylar substrates, utilizing advanced the X-ray nanoscopy techniques at the CARNAUBA beamline of SIRIUS source at the LNLS/CNPEM.

The challenges posed by focused X-ray beams causing damage to metal halide perovskites were tackled through a comprehensive multi-technique approach. The irradiation-induced damage predominantly affected iodine and organic components, reducing their relative quantity. The morphological transformation of the sample was observed, manifesting as an excavated area with altered local optical properties, indicative of the formation of an optically inactive metal layer. Intriguingly, the bulk of the material remained unchanged under the excavated area, maintaining the initial halide proportion as evidenced by stable photoluminescence emission energy. A strategic approach involved controlling both the beam dose and the surrounding environment to mitigate the detrimental effects of the X-ray dose. This entailed the combination of a precisely controlled X-ray dose with an inert N_2 atmosphere, establishing conditions to probe properties while efficiently minimizing damage.

The investigation extended to diverse compositions of $Cs_xFA_{1-x}Pb(Br_{0.38}I_{0.62})_3$, x=10,20,30,40, emphasizing the relevance of the Mylar substrate as a cost-effective alternative for X-ray transmission techniques. The CARNAÚBA beamline provides an X-ray nanobeam with precise characteristics, facilitating simultaneous or correlative measurements of morphology, chemical distribution, and optoelectronic response. X-ray fluorescence analysis revealed heterogeneities in Br:Pb ratios correlated with the wrinkled morphology, providing insights into stoichiometric variations at the micrometer to nanometer scale. X-ray excited optical luminescence confirmed the impact of composition on the luminescence response, emphasizing the role of Cs content in enhancing sample resilience to X-ray irradiation. Nanodiffraction experiments contributed valuable information on lattice parameters, while ptychography offered detailed insights into micro and nanoscale morphology and grain structures.

The comprehensive approach also employed non-synchrotron techniques, like electron and atomic force microscope, photoluminescence, and infrared spectroscopy, shedding light on the intricate interplay between composition, morphology, structure, and optoelectronic properties in Cs-rich perovskite thin films. The work in this thesis paves the way for advancements in the high-resolution imaging techniques of beam-sensitive materials for future device applications.

Keywords: Metal halide perovskite, Organic-inorganic hybrid perovskite, synchrotron, X-ray nanoprobe, Coherent diffraction, Ptychography, nanodiffraction, X-ray excited optical luminescence.

RESUMO

Os compostos de perovskita de haleto metálico (MHP) surgiram como candidatos promissores para dispositivos optoeletrônicos de próxima geração, oferecendo propriedades fotovoltaicas e de emissão de luz excepcionais. A tese explora filmes finos híbridos orgânico-inorgânicos de MHP, empregando técnicas síncrotron multiespectrais de ponta para revelar heterogeneidades de micro a nanoescala e sua relação com propriedades optoeletrônicas. O foco principal é a manipulação do conteúdo de césio (Cs) na composição, uma variável chave que afeta as características estruturais e optoeletrônicas. Através do comissionamento e desenvolvimento de técnicas avançadas, como pticografia de raios X, nanodifração de raios X, fluorescência de raios X e luminescência óptica excitada por raios X, o estudo visa fornecer insights sem precedentes sobre a heterogeneidade intrincada de filmes finos de perovskita híbrida. Uma investigação abrangente foi conduzida em filmes finos de perovskita $Cs_xFA_{1\text{-}x}Pb(Br_{0.38}I_{0.62})_3$, que exibiam uma morfologia enrugada distinta , depositados em substratos Mylar, utilizando técnicas avançadas de nanoscopia de raios X da linha de luz CARNAUBA da fonte SIRIUS do LNLS/CNPEM.

Os desafios colocados pelos feixes de raios X focados que causam danos às perovskitas de iodetos metálicos foram enfrentados através de uma abordagem multitécnica abrangente. Os danos induzidos pela irradiação afetaram predominantemente o iodo e os componentes orgânicos, reduzindo sua quantidade relativa. Foi observada a transformação morfológica da amostra, manifestando-se como uma área escavada com propriedades ópticas locais alteradas, indicativo da formação de uma camada metálica opticamente inativa. Curiosamente, a maior parte do material permaneceu inalterada sob a área escavada, mantendo a proporção inicial de haleto, conforme evidenciado pela energia estável de emissão de fotoluminescência. Uma abordagem estratégica envolveu o controle da dose do feixe e do ambiente circundante para mitigar os efeitos prejudiciais da dose de raios X. Isso implicou a combinação de uma dose de raios X controlada com precisão com uma atmosfera inerte N_2, estabelecendo condições para sondar as propriedades e, ao mesmo tempo, minimizar os danos de forma eficiente.

A investigação estendeu-se a diversas composições de $Cs_xFA_{1\text{-}x}Pb(Br_{0.38}I_{0.62})_3$, x=10,20,30, 40, enfatizando a relevância do substrato Mylar como alternativa econômica para técnicas de transmissão de raios X. A linha de luz CARNAÚBA fornece um nanofeixe de raios X com características precisas, facilitando medições simultâneas ou correlativas de morfologia, distribuição química e resposta optoeletrônica. A análise de fluorescência de raios X revelou heterogeneidades nas proporções Br:Pb correlacionadas com a morfologia enrugada, fornecendo insights sobre variações estequiométricas na escala micrométrica a nanométrica. A luminescência óptica excitada por raios X confirmou o impacto da composição na resposta de luminescência, enfatizando o papel do conteúdo de Cs no aumento da resiliência da amostra à irradiação de raios X. Experimentos de nanodifração contribuíram com informações valiosas sobre os parâmetros da rede, enquanto a pticografia ofereceu insights detalhados sobre a morfologia e estruturas de grãos em micro e nanoescala.

A abordagem abrangente também empregou técnicas não síncrotron, como microscópio eletrônico e de força atômica, fotoluminescência e espectroscopia infravermelha, lançando luz sobre a intrincada interação entre composição, morfologia, estrutura e propriedades optoeletrônicas em filmes finos de perovskita ricos em Cs. O trabalho nesta tese abre caminho para avanços nas técnicas de imagem de alta resolução de materiais sensíveis ao feixe para futuras aplicações de dispositivos.

Palavras-chave: Perovskita de iodetos metálicos, Perovskita híbrida orgânica-inorgânica, síncrotron, nanossonda de raios X, Difração coerente, Pticografia, nanodifração, luminescência óptica excitada por raios X.

List of Figures

LIST OF TABLES

LIST OF SYMBOLS

Symbol	**Unit**	**Description**
λ	[Å]	Wavelength
h	[Js]	Planck's constant
c	[m/s]	Light speed
E	[keV]	Energy
d_{hkl}	[Å]	Interplanar distance of the hkl plane
2θ	[°]	Scattering angle
Ψ, ψ		Wavefunction
$\mathcal{O}$		Oversampling criteria
R	[m]	Sample to detector distance
Δx	[m]	Pixel size of detector
σ	[m]	Pixel size of ptychography reconstruction
ΔT_{Total}	[s]	Total time spend per point in step scan map
ΔT_{Sum}	[s]	Total of detector integration per point in step scan map
$\Delta T_{Irradiation}$	[s]	Total of irradiation per point in step scan map
δ	[s]	Delay time between starting moment of cycle and irradiation

CONTENTS

CHAPTER 1

INTRODUCTION

In recent years, metal halide perovskite (MHP) materials have emerged as promising candidates for next-generation optoelectronic devices, offering exceptional photovoltaic and light-emitting properties. This thesis embarks on a comprehensive exploration of hybrid organic-inorganic MHP thin films, employing cutting-edge multispectral synchrotron techniques to unveil micro to nanoscale heterogeneities within the samples. The primary focus is manipulating cesium (Cs) content within the composition, a key variable impacting the material's structural and optoelectronic characteristics. Through the commissioning and development of advanced techniques such as X-ray ptychography, X-ray nanodiffraction (nXRD), X-ray fluorescence (XRF), and X-ray Excited Optical Luminescence (XEOL), this study aims to provide unprecedented insights into the intricate heterogeneity of hybrid perovskite thin films.

Incorporating cesium in hybrid perovskite compositions introduces a dynamic dimension to the material's properties, influencing its crystalline structure, electronic behavior, and overall performance. As we delve into the micro-to-nanoscale regime, the multispectral synchrotron techniques, including ptychography and nanodiffraction, enable the high-resolution imaging and mapping of structural features. Additionally, XRD facilitates the analysis of crystallographic phases, while XEOL offers a unique window into the luminescent properties of these materials. The investigation spans the entire thin film spectrum, from macroscopic compositional variations to the intricate details of localized heterogeneities.

Throughout this thesis, the concurrent development and application of these state-of-the-art synchrotron techniques will not only deepen our understanding of hybrid perovskite thin films but will also contribute to the refinement of experimental methodologies in the field of advanced materials characterization. By elucidating the impact of cesium content on the micro to nanoscale heterogeneities, this research endeavors to propel the optimization and design of hybrid perovskite materials for enhanced performance in a myriad of optoelectronic applications.

In the inaugural chapter of this thesis, a revision exploration into the perovskites realm is undertaken, providing a comprehensive overview of the current status of hybrid perovskite materials. This chapter will delve into the nuanced properties tunable through halide composition, shedding light on the intricate interplay between structural variations and optoelectronic characteristics. Furthermore, a focused examination of the cesium (Cs) effect will be presented, specifically addressing its impact on stability and morphology within hybrid perovskite thin films. This foundational chapter aims to establish a robust understanding of the material system under investigation, laying the groundwork for subsequent analyses and interpretations.

Moving forward, the second chapter introduces the intricate world of synchrotron technology and techniques, unveiling the experimental setup that forms the backbone of this study. Synchrotron radiation provides unparalleled capabilities for probing materials at the nanoscale, and this chapter elucidates the specifics of how ptychography, nanodiffraction, XRD, and XEOL are harnessed to extract valuable insights from hybrid perovskite thin films. The aim is to provide readers with a clear understanding of the advanced synchrotron methodologies employed throughout the subsequent experimental chapters.

The third chapter embarks on a methodological investigation into beam damage, a critical consideration when employing synchrotron techniques for material characterization. This chapter will systematically explore the beam's impact on samples with a chosen composition, different from the main composition of the work, delving deep into the intricacies of beam-sample interactions. The goal is to unravel the effects of the beam on structural and optoelectronic properties, ultimately determining the optimal experimental conditions to mitigate beam-induced alterations.

The fourth chapter unfolds the culmination of this research effort, presenting the actual experiments conducted at the synchrotron facility. The focus will be on hybrid perovskite thin films with varying Cs content, allowing for the systematic analysis of micro to nanoscale heterogeneities. In the Appendixes, the characterization spectrum is broadened, encompassing non-synchrotron techniques to complement, reinforce, and corroborate the findings derived from the advanced synchrotron methodologies. This holistic approach ensures a robust and comprehensive exploration of the hybrid perovskite materials, contributing to the evolving landscape of advanced materials research. The fifth chapter discusses the overall outcomes of the thesis and presents some prospects.

CHAPTER 2

HYBRID METAL HALIDE PEROVSKITES

The modern lifestyle and the increase in world population have dramatically increased the energy demand, pushing the development of new energy sources, such as sunlight, biomass, geothermal resources, water, and wind. Among new photovoltaic materials for sunlight harvesting, metal halide perovskites (MHP) (ABX_3, where $A=CH_3NH^{3+}$, $CH(NH_2)^{2+}$ or Cs, $B=Pb^{2+}$, $X= I^-$ or Br^-) (Figure 2.3) are the most promising for solar cells and detectors owing to their low processing cost, [5] easy fabrication, [6] [7] [8] high-power conversion efficiency, [9] [10] and high scintillation yield. [11] [12] [13] Despite that, several aspects of morphology, chemical composition, and optoelectronic properties are to be uncovered from the micro to the nanoscale in order to understand and better harness these materials properties. [2] [14] To fill these holes in the knowledge about the hybrid perovskites, the synchrotron techniques are very promissing tools to investigate the physics and chemistry involved in this family of materials, from its fundamental properties [15], interaction and response to different forms of radiations [16], synthesis methods and their dynamics [17] [18], and behaviour during *in situ* and *in operando* [14] conditions. Figure 2.1 depicts this concept.

With the arising of the new 4th generation synchrotron light sources [19] and its inherent high brilliance and coherence, a huge number of new techniques and possibilities to apply already well established techniques, that were until this moment unachievable in some spatial and temporal scales, are now available for use.

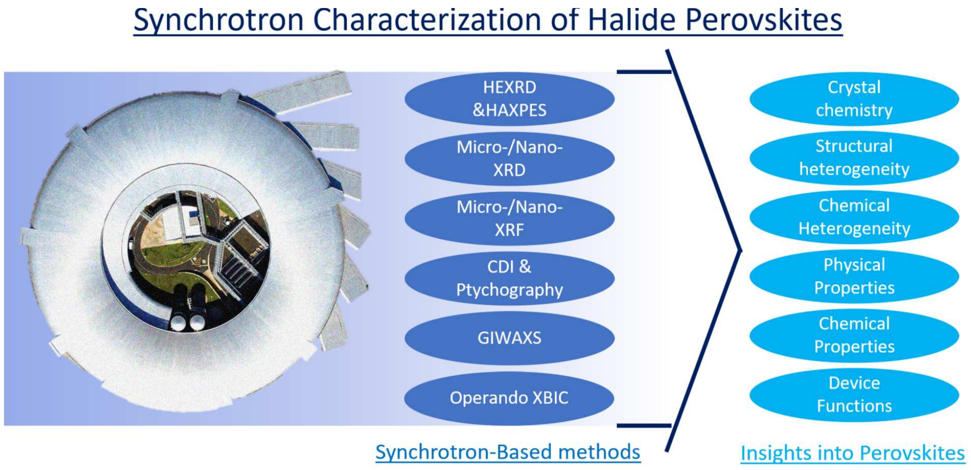

Figure 2.1: Synchrotron characterization of Halide perovskites. Adapted from: [1]

2.1 Photovoltaic hybrid metal halide perovskite

The hybrid halide perovskites (PVSK) are being considered as one of the most promising candidates for a cheap and efficient material to the role of charge absorbers or charge donors to be applied in photovoltaic and LED devices. The main features of this class of materials are: the relatively high tolerance to defects, the long carrier diffusion lengths, the slow recombination rate when compared to the energy relaxation rate within each band, the sharp absorption onset [20] and the high tunability of the bandgap, over the range 1.6 - 2.3 eV with the substitution of the I^- (iodine) in the X-site by Br^- (bromine) (the band-gap value increases with increasing the proportion Br:I) [21]. In fact, this last attribute makes the PVSK not only a reasonable but also a very versatile material for the applications in both narrower band-gaps single-junction and larger band-gaps tandem solar cells. One of the main drawback of PVSK with respect to the conventional Silicon based solar cells is the photo-structural-chemical instability. Hoke's group noted that under illumination, the PVSK segregates into higher band-gap (rich in Br) and lower band-gap (rich in I) regions [22]. This segregation is attenuated with the substitution of the organic part in the A-site by Cs, which has shown to optically stabilize the perovskites [23]. This effect has been heavily studied by groups in different working conditions [24] [25] [26].

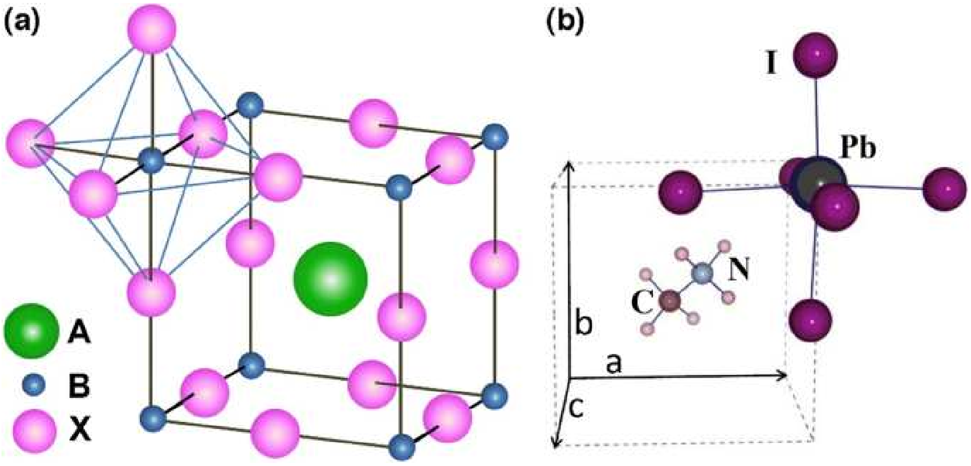

Figure 2.2: Perovskite strucutre. (a) General ABX_3 perovksite strucuture. (b) Hybrid perovksite unity cell of $FAPbI_3$. Adapted from: [2]

In the early stages of research, hybrid metal halide perovskites were primarily studied for their potential in solar cells. Their unique crystalline structure and favorable optoelectronic properties contributed to a rapid surge in photovoltaic efficiency. [27] [28] This efficiency evolution has been particularly noteworthy, with perovskite-based solar cells achieving efficiency levels that rival traditional silicon-based counterparts. [29] The ease of fabrication and cost-effectiveness further fueled the interest in perovskite solar cells. [30]

Beyond solar cells, the versatility of metal halide perovskites became evident as researchers explored applications in lasers and detectors. Their excellent light-emitting properties make them promising candidates for optoelectronic devices. [31] [32] Perovskite lasers have shown potential for applications in communication and imaging, while perovskite-based detectors have demonstrated sensitivity across the electromagnetic spectrum. [33]

However, this rapid progress has been accompanied by challenges and limitations. Stability issues have been a persistent concern, with metal halide perovskites exhibiting sensitivity to moisture, temperature, and light. [16] [34] [35] [36]Addressing these stability issues is crucial for the commercial viability of perovskite-based technologies.

The importance of stability becomes particularly pronounced in the context of their application in solar cells. While perovskite solar cells exhibit exceptional efficiency, concerns about long-term stability and degradation mechanisms need resolution for widespread adoption. Researchers are actively engaged in developing strategies to enhance the stability of perovskite materials, ranging from encapsulation techniques to novel material formulations. [37] [38]

The journey of metal halide perovskites from early research stages to multifaceted applications is a testament to their exceptional properties. The evolution in efficiency, coupled with applications in solar cells, lasers, and detectors, underscores their versatility. However, challenges in stability must be overcome for these materials to fulfill their promise of revolutionizing various technological landscapes. The ongoing efforts to solve these challenges will play a pivotal role in determining the enduring impact of metal halide perovskites in the realm of advanced materials and devices.

Perovskite structures (Figure 2.3), notably ABX_3, where A and B are cations and X is an anion, exhibit a distinctive crystal lattice that offers remarkable versatility in electronic and optical properties. In the context of hybrid perovskites, the A-site is typically occupied by an organic cation like methylammonium (MA) or formamidinium (FA), and the B-site is usually occupied by a metal cation, such as lead (Pb). The organic cations contribute to the unique electronic and optical characteristics of hybrid perovskites, enabling tunability for various applications. The organic-inorganic coupling in these materials provides advantages in terms of bandgap engineering, making them particularly appealing for optoelectronic devices.

2.2 Compositional control for properties optimization

Compositional control is a pivotal consideration in the optimization of hybrid metal halide perovskites (MHPs) for diverse applications. The choice of halide ions—iodide, bromide, or chloride—profoundly influences the electronic structure, dictating the bandgap and absorption characteristics of MHPs. Halide mixing provides a dynamic avenue for compositional control, allowing precise adjustments in the ratio of different halides to finely tune the perovskite's properties, particularly its bandgap. [39] Transitioning from smaller to larger halides, such as from iodide to bromide, induces a red-shift in the absorption spectrum. This results in a decreased bandgap, altering the optical and electronic properties of the

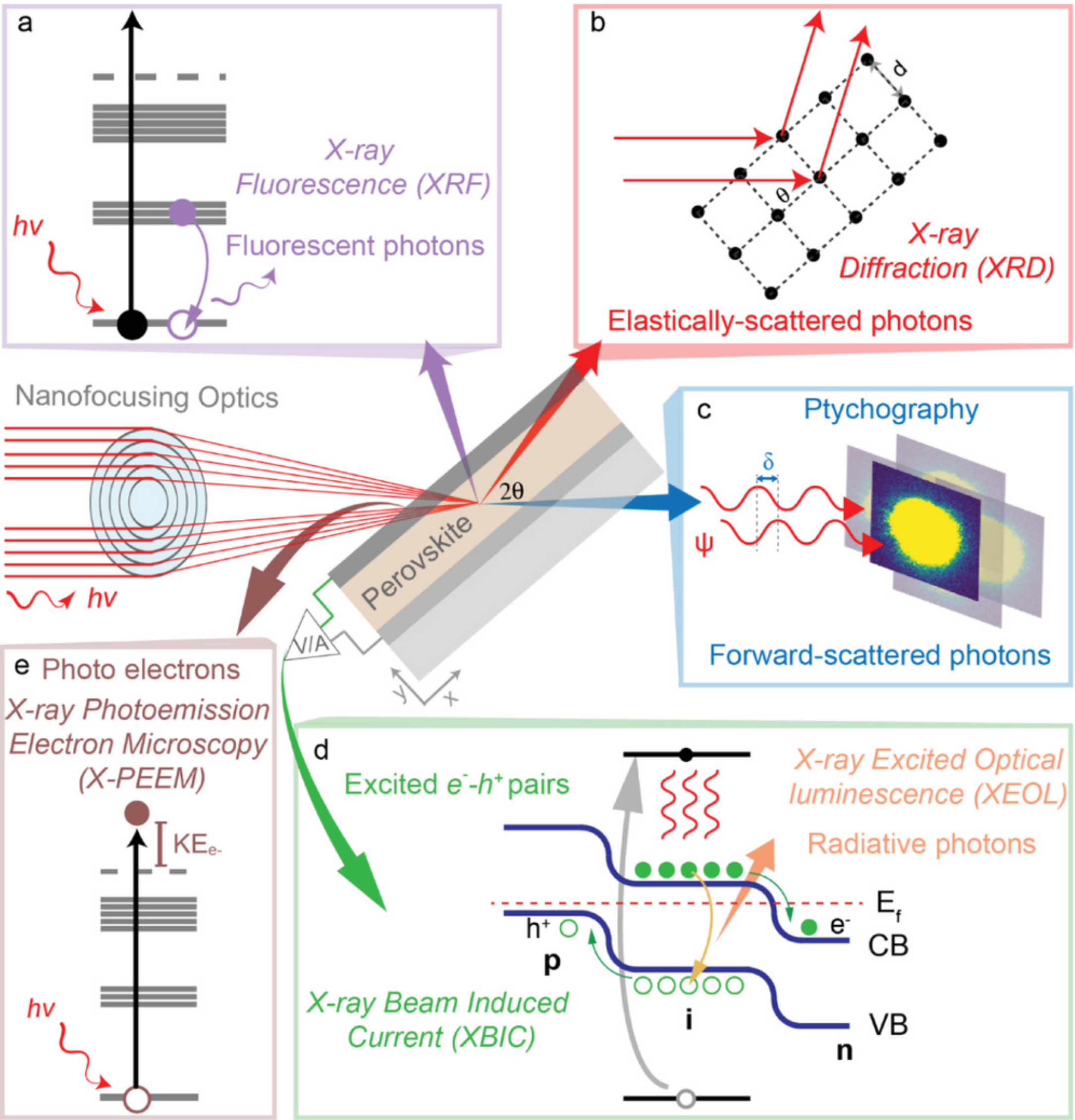

Figure 2.3: X-ray synchrotron techniques for halide perovskites. Reproduced from: [2].

perovskite. However, maintaining the correct stoichiometry is paramount in compositional control. Deviations from the ideal cation-to-halide ratio can lead to phase segregation, impacting overall performance. [21]

Researchers explore the concept of graded bandgap layers by introducing a gradual change in halide composition within a single perovskite film. This approach creates multiple bandgaps within the same material, enhancing its versatility in light absorption and energy conversion. Compositional control is intricately linked to phase transitions in MHPs. Understanding these transitions is crucial for optimizing material properties and ensuring stability under varying conditions. However, achieving specific optical and electronic properties often involves trade-offs. While certain halide compositions may enhance light absorption, they could simultaneously impact the material's stability. Researchers navigate these trade-offs to find optimal compositions for targeted applications. [40]

The stability of MHPs is a central concern linked to compositional control. Changes in halide composition can influence the material's structural integrity and performance over time. Thus, balancing the quest for improved properties with material stability is a constant consideration in the pursuit of tailoring hybrid metal halide perovskites for effective applications. [40]

2.3 The halide proportion effect

Halide mixing is a sophisticated strategy extensively employed in the realm of hybrid perovskite materials to meticulously control and optimize their electronic properties, with a primary focus on bandgap tuning. This approach enables a continuous and precise adjustment of the bandgap across a broad energy spectrum. Typically, transitioning from bromine (Br-) to iodine (I-) in the perovskite composition induces a red-shift in the absorption spectrum, leading to a corresponding decrease in the bandgap. [21] This fine-tuning capability is instrumental in tailoring perovskite materials for specific applications, such as solar cells and light-emitting devices. [40]

In the context of halide mixing, the balance between achieving desired optical and electronic properties is critical. While the red-shift in absorption enhances sunlight capture in solar cells, maintaining optimal charge transport properties is equally essential for efficient device performance. Hybrid perovskites with mixed halides, often referred to as mixed-halide perovskites, have gained prominence due to their superior stability and enhanced optoelectronic properties compared to their single-halide counterparts. [40]

The substitution of halide ions in hybrid perovskites induces a profound impact on the orbital superposition of the constituent elements, subsequently altering the band structure of the material. This phenomenon is rooted in the electronic interactions between the metal cations and halide anions within the perovskite lattice. [41]

The electronic structure of a perovskite is essentially determined by the energy levels and spatial distribution of its orbitals. Different halides possess distinct electronegativities and atomic sizes, leading to variations in the nature of their chemical bonds with the metal cations. This halide-dependent interaction influences the degree of orbital overlap between the metal and halide atoms. [42]

As the halide is changed, the orbital superposition between the metal and halide atoms adjusts. For example, transitioning from smaller to larger halides, such as from iodide to bromide, results in an increased spatial overlap of orbitals. This altered orbital superposition directly affects the electronic configuration of the material. In essence, the tunability of the band structure through halide substitution provides a versatile means to engineer the electronic properties of hybrid perovskites. This understanding of the intricate interplay between orbital superposition and band structure is pivotal for designing perovskite materials with optimized functionalities. [41]

Researchers also explore gradient compositions, where the halide content varies gradually across the perovskite film. This results in a gradient bandgap within the material, contributing to improved light absorption and charge collection efficiency. However, the impact of halide mixing on the structural stability of the perovskite must be considered, as certain compositions may lead to phase segregation or undesirable crystal structures, affecting long-term stability. [43]

Despite its powerful capabilities in bandgap engineering, challenges related to material stability, reproducibility, and scalability persist. Ongoing research is dedicated to addressing these challenges to fully unlock the potential of mixed-halide perovskites and propel advancements in solar cell and optoelectronic technologies. [40]

2.4 Cs incorporation for perovskite stability

Cesium (Cs) plays a pivotal role in metal halide perovskites, exerting a multifaceted influence on their properties with profound implications for stability. One of the pronounced positive effects of Cs incorporation is the observed improvement in the stability of perovskite structures. The introduction of Cs in the A site has been associated with an increased resistance to environmental factors such as moisture, heat, and light, thereby contributing to the longevity and durability of perovskite-based devices, especially in critical applications like solar cells.

In addition to its stabilizing role, Cs has proven effective in reducing ion migration within the perovskite lattice and inhibts the formation of the hexagonal phases leading to the improvement of devices [44] [45]. This reduction is particularly significant in mitigating performance degradation and hysteresis, a common challenge faced by perovskite solar cells. By curbing ion migration, Cs incorporation aids in maintaining the structural integrity and electronic properties of the perovskite material over extended periods, enhancing the overall operational efficiency of devices.

Moreover, the presence of Cs in perovskites holds promise in enhancing the structural tolerance factor. [46] The Goldschmidt tolerance factor [47] (t) is a key parameter in perovskite structures that affects their stability and properties. It is a ratio that considers the sizes of the 'A,' 'B,' and 'X' ions, calculated as $t = \frac{R_A+R_X}{\sqrt{2}(R_B+R_X)}$, where, R_A, R_B, R_C are the ionic radii of A, B and X ions, as shown in Figure 2.3, respectively. The tolerance factor provides insight into the distortion of the perovskite structure from an ideal cubic shape. [48] This modification contributes to the stabilization of the crystal structure, reinforcing the improved stability observed in Cs-containing perovskites. [25] [49] [50] However, finding the optimal balance of Cs content is crucial, as excessive amounts may lead to phase instabilities, a consideration that warrants careful attention in material design to avoid compromising the long-term structural and functional integrity of the material. Literature commonly indicate that tolerance factor value must be in the range of $0.813 < t < 1.107$ for ideal cubic structures or a distorted perovskite structure with tilted octahedra. [51] Outside this range, the perovskite is no longer considered stable.

Furthermore, the impact of Cs on the bandgap of perovskites is a critical aspect to explore. Cs incorporation can induce changes in the bandgap, potentially affecting the optical properties of the material. Managing this bandgap shift becomes pivotal in maintaining the desired properties for specific applications. Careful consideration and optimization of Cs content are essential to harness its stabilizing benefits while mitigating potential drawbacks, ensuring that perovskite materials meet the demands of diverse technological applications.

In summary, Cs demonstrates a multifaceted influence, playing a dual role in enhancing the stability of metal halide perovskites. Through mechanisms like improved stability, reduced ion migration, and enhanced structural tolerance factor, Cs incorporation holds significant promise for advancing the reliability and longevity of perovskite-based devices, reaching the optimal value for devices performance between 5% and 10% in the Cs content. [26] [52] [53] Ongoing research endeavors focus on fine-tuning these effects, providing valuable insights for optimizing Cs content tailored to specific practical applications in the field of solar energy and beyond.

2.5 Corrugations in the morphology

The incorporation of a substantial amount of cesium (Cs) in metal halide perovskites during the annealing process induces a fascinating phenomenon—wrinkling or corrugation in the material that is a intrinsic property for Cs-rich perovskites. This occurrence arises as a consequence of strain relief mechanisms activated during the annealing process. The large presence of Cs introduces structural perturbations, leading to a dynamic interplay between the perovskite lattice and the stress generated during the annealing phase. [54]

As Cs atoms become integral components of the perovskite structure, their incorporation induces local distortions and alterations in the crystal lattice. These modifications trigger strain within the material, and during annealing, the perovskite undergoes a process of self-adjustment to relieve this strain. The formation of wrinkles or corrugations emerges as a visible manifestation of this strain relief mechanism.

The intricacies of this phenomenon are tied to the unique interactions between Cs and the perovskite matrix. The strain relief process becomes particularly pronounced when a significant quantity of Cs is introduced. The resulting corrugated morphology can have implications for the material's optoelectronic properties and its performance in devices. Comparing the cation in the A site of the perovskite structure, involving formamidinium (FA), methylammonium (MA), and Cs, the varying ionic radii of these cations play a crucial role. Cs, having a smaller size compared to FA and MA, [26] introduces additional strain and distortions to the lattice. This difference in cation size contributes to the observed wrinkle formation during annealing, as different size in the cations may require more extensive lattice adjustments, leading to the distinctive corrugated morphology. [54]

Understanding the dynamics of wrinkle formation in Cs-rich metal halide perovskites is not only scientifically intriguing but also holds practical significance. The ability to manipulate and control these structural features during the annealing process could open avenues for tailoring the properties of perovskite materials for specific applications, providing insights into the delicate balance between strain, Cs incorporation, and the resulting morphological characteristics. [54] Ongoing research in this area seeks to elucidate the underlying mechanisms and optimize the annealing conditions for the controlled development of wrinkles in Cs-containing perovskites, offering valuable contributions to the evolving field of perovskite-based technologies. [55] [45]

CHAPTER 3

SYNCHROTRON LIGHT AND TECHNIQUES

The interaction of the X-ray with matter is composed of a rich variety of responses. But no matter the energetic range of the spectra, the manifested phenomena of their interaction are scattering, absorption, and, eventually, decay processes. The x-ray spectra go from the photon energy (E) of approximately 100 eV up to 1 MeV., which corresponds to a wavelength (λ) range of 124 Å down to 0.01 Å, respectively. [56] This relation is given by the identity:

$$E = h\nu = hc/\lambda, \tag{3.1}$$

in which, $h = 6.626 \times 10^{-34}$ Js is Planck's constant, ν is the frequency of the radiation in Hz, $c = 2.9979 \times 10^{8}$ m/s is the speed of light in vacuum, and λ is the wavelength of light. In practical numbers one can write: $E[keV] = 12.398/\lambda[\text{Å}]$. [56]

X-rays interacting with the material can undergo elastic (Thomson) or inelastic (Compton) scattering or be absorbed, resulting in the emission of electrons or lower-energy photons. If none of these interactions take place, the photon transmits through the sample. All this process (P) has a probability to occur, depending on the energy and the electronic density that can be mathematically calculated through the cross-section (σ_P) of each of these processes. These basic processes lead to the available techniques used to study matter. [56]

The generation of light through the acceleration of particles is a fascinating interplay of fundamental physics and cutting-edge technology. At the heart of this process lies the use of particle accelerators, where charged particles, typically electrons, are accelerated to relativistic speeds. As these high-energy electrons traverse curved trajectories within strong magnetic fields, they emit electromagnetic radiation known as synchrotron radiation. This phenomenon finds extensive applications in various scientific disciplines, from fundamental research in particle physics to advanced imaging techniques in medicine and it provides the most essential tool for this work. The main points about the synchrotron radiation generation and related technology is described Appendix C.

3.0.1 Carnaúba beamline

The inception of the CARNAÚBA beamline project dates back to 2015 when the initial conceptual design report was formulated, followed by the conclusive design in 2017, signaling the commencement of primary instrumental advancements. The assembly phase coincided with the SARS-Covid-19 pandemic in 2020, the beginning of the doctorate period. The beamline underwent technical and internal scientific commissioning from November 2020 to October 2021. By October 2021, it welcomed external users for scientific commissioning experiments. Presently, the beamline is fully operational for standard proposal submissions.

CARNAÚBA is among the first-phase beamlines at Sirius-LNLS [57]. It is meticulously designed to maximize the brilliance of the synchrotron source by converging the beam to the diffraction limit while retaining a substantial portion of the photon flux emitted by the undulator. An all-achromatic mirror-based optics system facilitates the generation of a nano-focused beam for raster-scanning the sample (Figure 3.1) [58]. A side-bounce cylindrical mirror (M1) positioned at 27 m focalizes the undulator source (at 0 m) onto a secondary source aperture (SSA) device at 54 m. The SSA, in turn, trims part of the horizontal emission, optimizing the compromise between flux and coherent fraction, thereby influencing spatial resolution. The scattered beam from the SSA slabs is captured by two opposing photodiodes, forming an X-ray beam position monitor (XBPM) system. This setup ensures control over the horizontal beam position at the SSA aperture with a precision of a few micrometers. The photodiode output guides the steering of the beam through the pitch control of the M1 mirror [59]. Post SSA, the beam retro-reflects to the original direction via the second side-bounce flat mirror (M2). A KB (Kirkpatrick-Baez) mirror system [60] achieves the final focus at one of the experimental stations, involving four reflections of the original beam (three in the horizontal and one in the vertical planes). The first two mirrors are coated with Rh, Si, and Ni stripes, while the KB mirror is coated with Ni. The beamline functions in pink (high flux) or monochromatic (high energy resolution) beam modes. The latter is facilitated by a 4-side-bounce Si(111) crystal monochromator (4CM) [61], providing a resolving power of $E/\Delta E \sim 10000$ across the entire energy spectrum. In contrast, the high-flux mode, achieved by setting the Bragg angle to zero and laterally sliding the monochromator by 2 mm, results in a bandpass of a few percent, leading to a four-order magnitude gain in flux. The transition between modes requires only a few minutes without altering focus conditions. Except for the KB mirrors, all critical optical elements are cryogenically cooled to ensure efficient heat load dissipation and thermo-mechanical stability [62].

The beamline accommodates two in-line workstations (Figure 3.1 – insets) situated at two hutches, positioned on separate floor slabs with special foundations and air-conditioning temperature control, maintaining approximately ± 0.05 °C around 24 °C. Given the extended distances from the insertion device to the stations and the minute beam sizes, the mechanical stability of all optomechanical systems along the beamline is of utmost importance. Vibration concerns were addressed through measurements affirming remarkable floor stability, showcasing integrated displacements between 2 and 450 Hz from 5 to 15 nm RMS (root mean square) in XYZ. Simultaneously, relative measurements over the extended distances demonstrated values below 10 nm RMS, partly constrained by sensor noise [63].

The first nanoprobe station, TARUMÃ (Tender to hArd x-ray foR sUb-Micro Analysis) [64] [3], boasts a substantial working distance of 450 mm, facilitating diverse sample environments for in situ, operando, in vivo, and cryogenic conditions. The second station, SAPOTI (Scanning Analysis by PtychO for Tomographic Imaging) [65], is designed to operate under high vacuum at cryogenic conditions to enhance spatial resolution and is anticipated to commence operations in early 2024. Both stations are tailored for combined multi-analytical X-ray techniques, encompassing XRD, XRF, XAS, XEOL, XBIC, forward ptychography, and Bragg CDI.

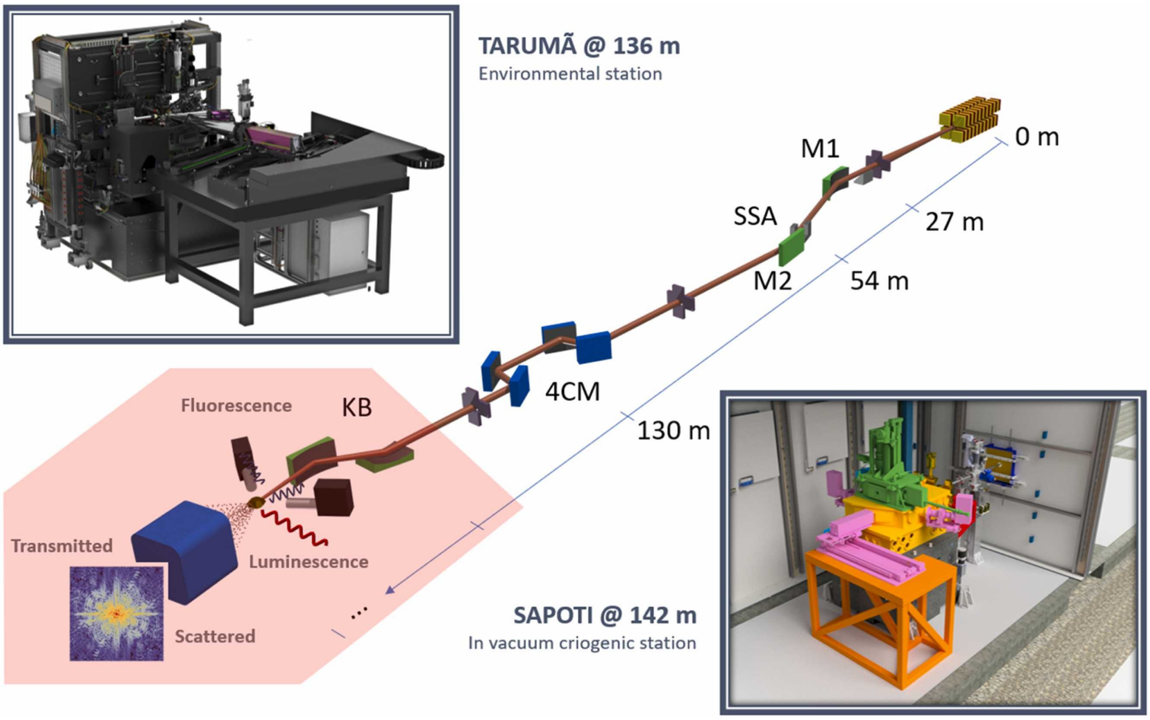

Figure 3.1: Carnaúba beamlin, showing the main optical components and the two experimental stations. Reproduced from: [3]

3.1 Synchrotron techniques

3.1.1 X-ray fluorescence - XRF

The x-ray absorption by the materials occurs in a discrete and well defined way, given the electronic distribution of the energy levels in the atom, just after the matter is hit by a photon with enough energy to surpass the biding energy of the electron to the nucleus. When this happens, the electron is removed from the atom, causing and abrupt increase in the absorption of the material. This threshold energy from which the absorption increases is called absorption edge of the shell from which the electron was expelled. Since the energies in which the electron is absorbed is unique for each element, the absorption edge is a distinctive property that identify each element. That is the principle of the x-ray absorption spectroscopy.

As soon as an electron from an inner shell of the atom is knocked out by the sufficiently energetic photon, an electron from a more exterior shell fills the vacancy left by the expelled one. In doing this transition from the outer to the inner level emits a photon with a characteristic energy, that is the difference between the energy levels, that corresponds to the fluorescence spectra of the inner level of energy. Consequently, the outer level is empty, and an electron from an even more exterior level fills this new vacancy, creating, subsequently, another emission series, as shown in Figure 3.2. Since the configuration of the energy levels in an atom is specific for an element, the fluorescence spectra are characteristic for each element and, because of this, it is experimentally used for chemical identification.

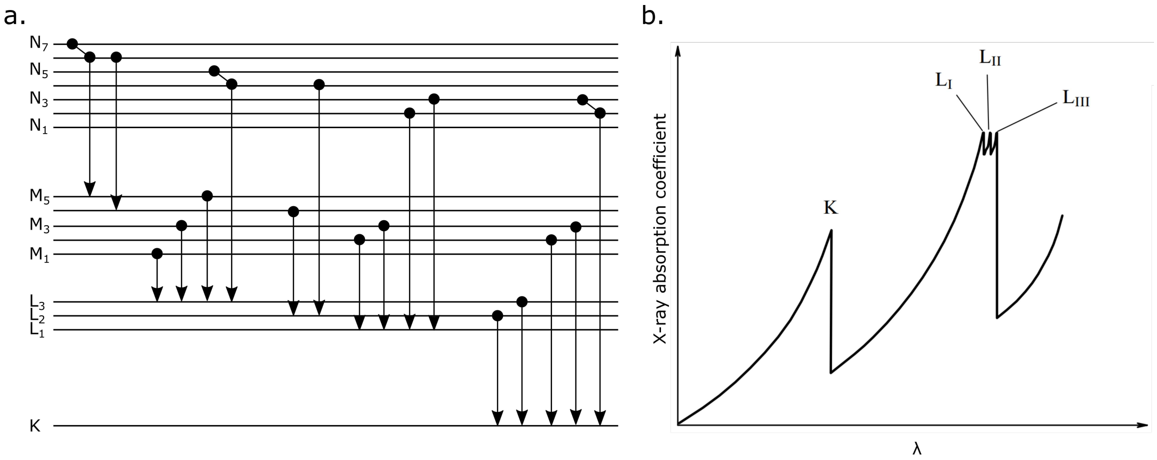

Figure 3.2: Energy level diagram and corresponding transitions. (b) X-ray absorption coefficient

Exploiting this process of photon-in-photon-out phenomena, one can scan the sample with a probe with dimensions smaller than the region of interest in a sample and acquire at each point fluorescence emission spectra. One example of a typical acquisition performed with this technique is shown in Figure 3.3, in which a Au Siemens standard (Applied Nanotools Inc.) was scanned with a 500(H) × 200(V) 12 keV beam at Carnaúba beamline. The summed spectra from the whole scan are shown in Figure 3.3.a with the emission lines of all the elements excited with the excitation energy. Figure 3.3 indicates the elastic scattering that emerges from the sample with the same energy similar to the incoming beam [56] and, just below, the inelastic Compton scattering [66] mostly due to the Si_3N_4 substrate. The peaks below in energy correspond to the fluorescence emission lines characteristic of the elements in the sample. Figure 3.3.b shows a fit performed in the fluorescence spectra from the region of 2500 eV up to 10300 keV (the Au-Lβ at 11442.3 keV was not included) using the software PyMCA [67]. One can observe the major presence of Au, corresponding to the 700

Fluorescence emission lines						
Atomic number	Element	Edge (eV)	Emission (eV)			Excitation energy (eV)
82	Pb	2484 (M5)	2345			7000
53	I	4557 (L3)	3937	3926	4220	10000
55	Cs	5012 (L3)	4286	4272	4620	10000
82	Pb	13035 (L3)	10551	10450	12613	14000
35	Br	13474 (L3)	11924	11877	13291	14000

Table 3.1: Fluorescence emission lines

nm deposited as the standard, and Cr deposited as the adhesion layer for Au over the Si. The second highest peak corresponds to Ar in the air (Kα and Kβ in 2957.7 eV and 3190.5 eV respectively). The minor elements (Fe, Cu, Ti, Ni, Mn) are attributed to the contamination signal from the experimental setup. Selecting a small fraction of the spectra corresponding to the emission lines and plotting the spatial distribution of the intensity of this region of interesting (ROI) in energy, one has the elemental distribution, what can be seen in Figure 3.3.c and .d for the Ar and Au fluorescence emissions. The ROI for the Ar was between 2080 eV and 3080 eV (green filled square in Figure 3.3.b), while the Au was between 9500 eV and 9800 eV (green filled square in Figure 3.3.b). The Ar spatial distribution is homogeneous, while the Au corresponds to the radial Siemens star pattern from the standard. All the fluorescence maps presented in this manuscript will follow the same procedure for analysis, with the energy of the emission lines and the ROIs will be explicit in the text, and the spectra will be summarized in Appendix D.

A fundamental property from the fluorescence signal is the fluorescence yield or fluorescence quantum yield which is the efficiency of fluorescence emission, roughly defined as the ratio of the number of fluorescent photons emitted to the number of incident photons absorbed by the material. Mostly it is determined by the element's intrinsic properties (cross section for a given absorption) and the energy of the excitation source. As the excitation energy increases, the cross-section for absorption edges at lower energies decreases. In simpler terms, this implies a reduced probability for transitions associated with lower energy absorption edges. Consequently, the fluorescence signal corresponding to these transitions becomes weaker compared to situations where the excitation energy is lower but still above the absorption edge, allowing the transition to occur more readily. [68] Other intrinsic factor is the probability of each transition to happen once it satisfies the selection rules from the quantum mechanics. [68] The fundamental details of these factors will not be discussed here. However, it raises the necessity to optimize the experimental conditions for the measurement of each element. The fluorescence lines in the perovskites that can be reached with Carnaúba beamline are summarized in Table 3.1 and the optimal excitation energies used for reaching the adequate statistics in the maps of each element are indicated.

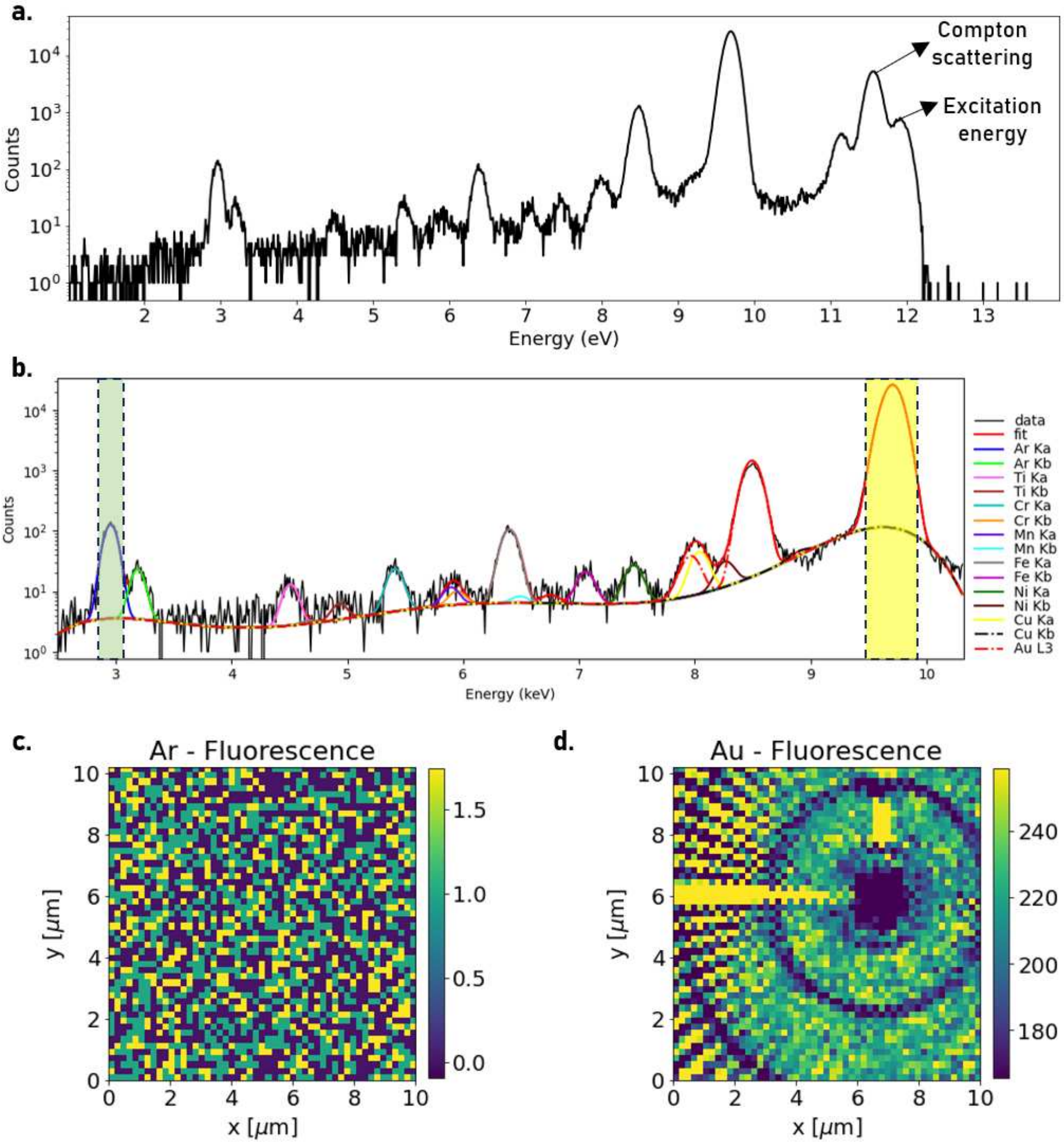

Figure 3.3: Fluorescence data. (a) Representative spectra of the Siemens star indicating Compton scattering and the elastic scattering (b) the fluorescence peak fit. (c) Ar fluorescence map (ROI integrated between 2080 eV and 3080 eV). (d) Au fluorescence map (ROI integrated between 9500 eV and 9800 e)

3.1.2 X-ray nanodiffraction - nXRD

The Bragg Law, formulated by the father-son duo William Henry Bragg and William Lawrence Bragg, is a fundamental principle in crystallography that describes the conditions for constructive interference of X-rays or neutrons scattered by a crystal lattice. According to this law, the path difference between waves scattered by crystal planes must be a multiple of the wavelength for constructive interference to occur [69], as depicted in Figure 3.4. Formally it relates the distance between the crystalline planes that are reflecting the incoming beam ($\vec{k}_{in}$) and outcome ($\vec{k}_{out}$) x-ray beams in the direction where a constructive interference will happen:

$$\lambda = 2d_{hkl}\sin\left(\frac{2\theta}{2}\right). \tag{3.2}$$

Or even more generally:

$$q = |\vec{Q}| = 2|\vec{k}|\sin\left(\frac{2\theta}{2}\right) = \frac{4\pi}{\lambda}\sin\left(\frac{2\theta}{2}\right), \tag{3.3}$$

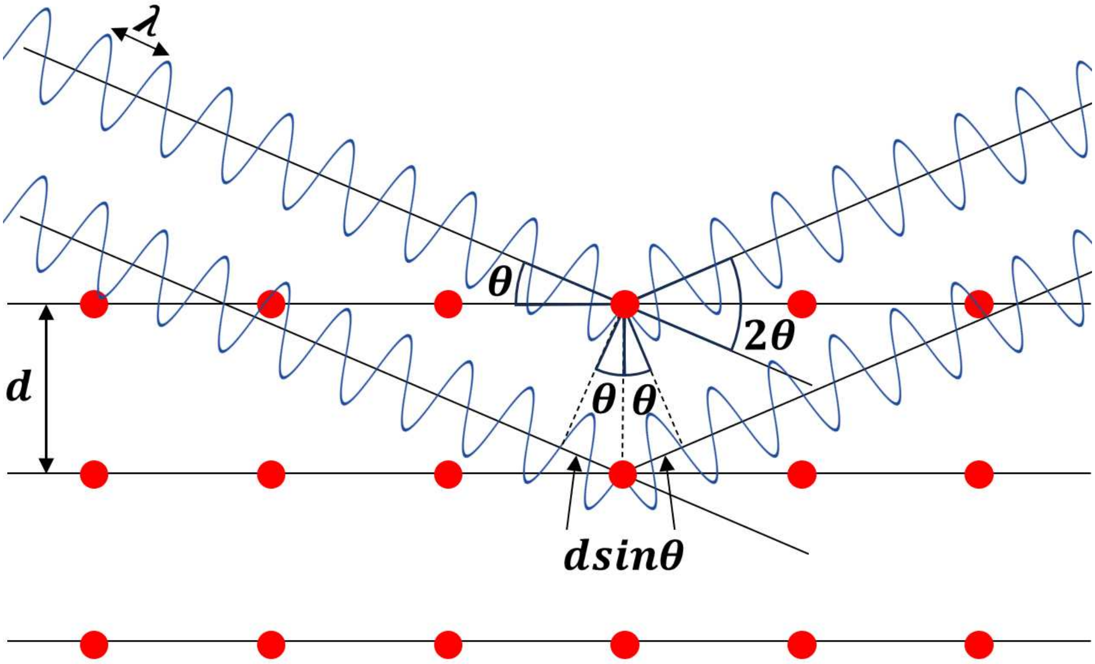

Figure 3.4: Illustration of Diffraction Condition in a Crystal Lattice.

What is known as Laue's equation, where one can relate $d = 2\pi/q$.

In a conventional X-ray diffraction (XRD) experiment made in synchrotrons or tabletop equipment, usually, at a fixed energy, the incidence angle θ of the beam at the surface of the sample is changed, and the detector goes to the correspondent 2θ position. The different points in which the diffraction signal appears are evidence of the interplanar distance between different families of planes at the crystal lattice. Other variations as polycrystalline samples in which the sample can be at a fixed position and only the detector moves, and even rotating samples when the polycrystal is randomly oriented. Not only this average interplanar spacing can be evaluated from this kind of analysis over the sections of the diffraction ring on the detector (Figure3.5.a), but, one can also know average strain, average size of grains, crystalline phases, preferred crystal orientations (texture), and crystallinity. [69] [70]

In the nanodiffraction, however, the crystalline structure distributions in materials are addressed with a spatial resolution of (hundreds to tens of) nanometers. [71] In this configuration, the x-ray probe crosses the sample acquiring the diffraction peak averaging only a small volume corresponding to the nanobeam interaction with each scanned point, making it possible to visualize the local variation in, for example, crystallinity, lattice parameter, texture, defects, between grains and gradients within grains larger than the nanobeam. The data analysis is in some sense similar to conventional diffraction, once the center of mass of the speckle encodes the information of the local lattice parameter as illustrated in Figure 3.5.b. The speckle's shape can give insightful information also about defects [72], symmetry, and morphology [73]. When the scattering crystallite is much larger than the beam the kinematics effects dominate. [74]

Figure 3.5 illustrates the principle in which a beam with dimensions smaller than the crystallites in the sample scans a region of interest. When the probe reaches a region of the sample with crystalline planes well oriented for the incident wavelength with respect to the Laue equation (Eq. 3.3), it produces a speckle in the area detector at the corresponding point in the reciprocal space. The fraction of the reciprocal space corresponding to the detector area is calculated as modeled in Appendix E and the speckle position is correlated to the angular position (scattering and azimuthal angles, 2θ and ϕ - Appendix F). The variation in the 2θ position from point to point encodes the lattice parameter gradient, and consequently the local strain field in the sample in that family of planes direction [73]. The variations in ϕ angle encode the mosaicity/texture/bending information of the material [75]. More detailed analysis of the speckle's symmetries and shape can still provide knowledge about defects [76] and shape [72], and in the case of a coherent nanobeam, morphology can also be investigated [77].

3.1.3 X-ray excited optical luminescence - XEOL

X-ray Excited Optical Luminescence (XEOL) is a spectroscopic technique that provides unique insights into the electronic and optical properties of materials at the nanoscale. This process involves the excitation of a material using X-rays, resulting in the emission of optical photons as the excited electrons recombine with holes in the electronic structure as illustrated in Figure 3.6.

When an X-ray photon is absorbed, it imparts energy to the inner-shell electrons, elevating them to higher energy states or ejecting them from the inner shells. The resulting

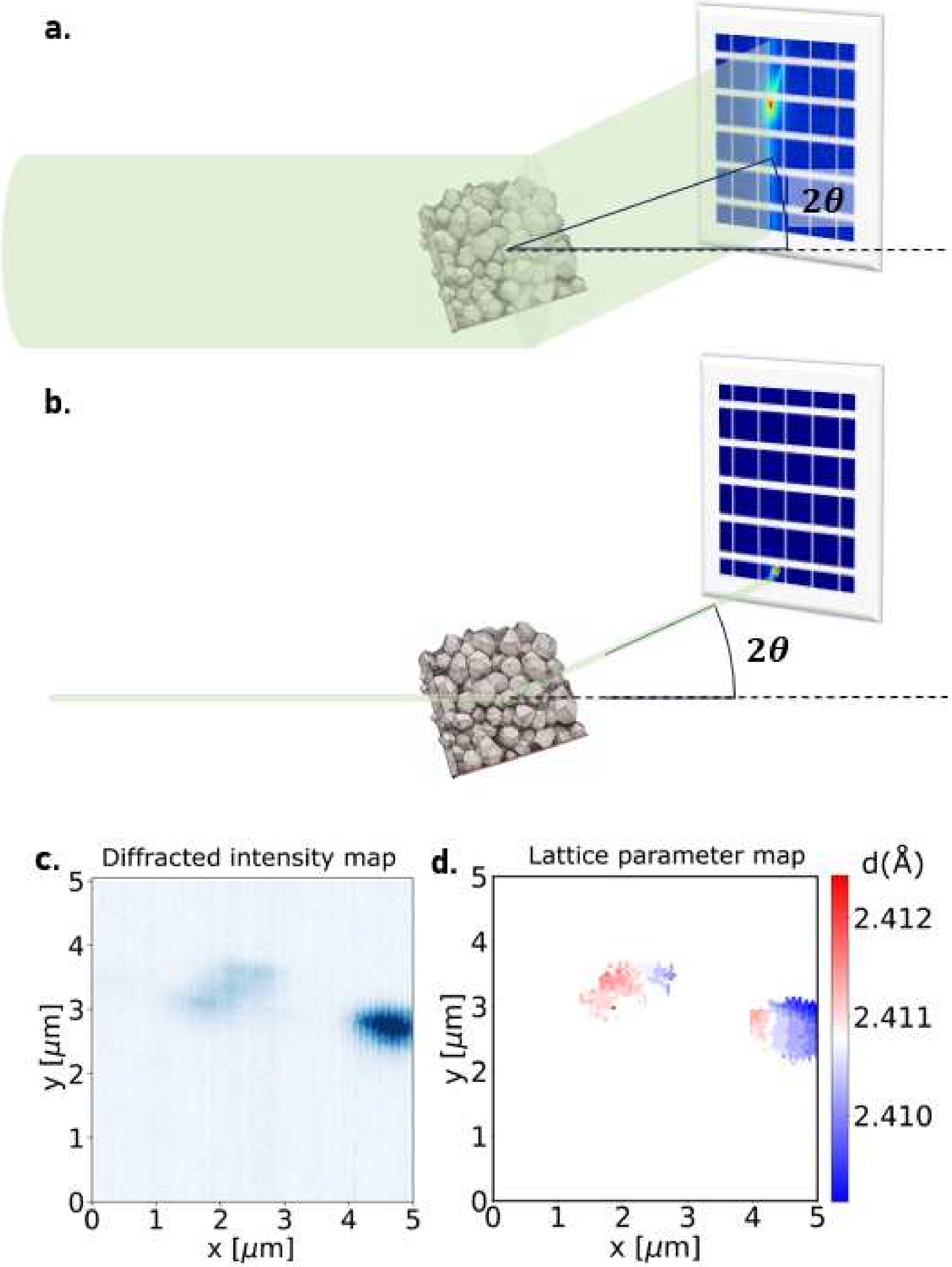

Figure 3.5: X-ray diffraction. (a) Conventional over-illuminated diffraction setup with powder ring in the detector position at the 2θ Bragg position. (b) Scanning nanodiffraction with focalized illumination diffraction setup with speckle in the detector position at the 2θ Bragg position.(c) Diffracted intensity map from scanning diffraction. (d) Lattice parameter map from scanning diffraction.

core holes create a cascade of electronic events as outer-shell electrons fill these vacancies, as previously described. This absorption triggers the generation of core holes when electrons are either elevated to higher energy states or expelled from inner electron shells, creating positively charged holes. Subsequently, these carriers, both electrons and holes, diffuse through the crystal lattice, moving toward regions of lower energy.

As electrons and holes arrive in the energy gap, the region between the valence and conduction bands, the conditions for recombination are established. Recombination is the process where electrons in higher energy states reunite with holes in lower energy states, resulting in the annihilation of electron-hole pairs. This intricate relaxation of the carriers culminates in the release of excess energy in the form of photons, manifesting as luminescence, often in the form of visible or ultraviolet light.

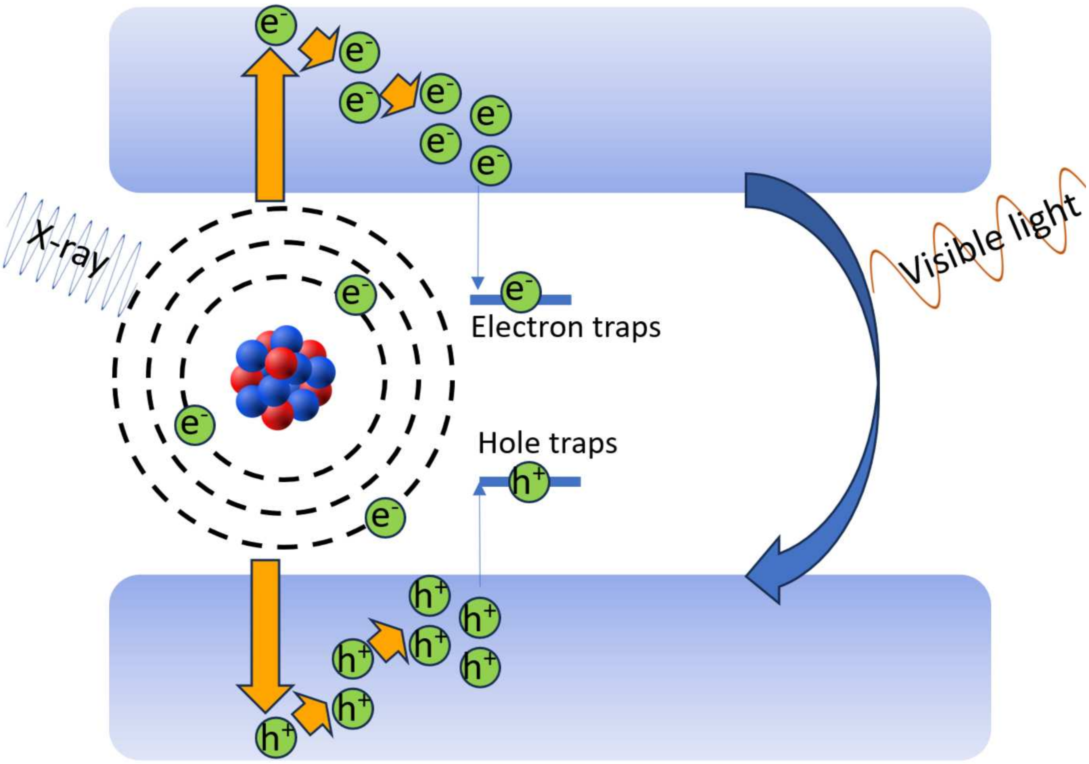

Figure 3.6: XEOL mechanism

The emitted optical photons carry information about the material's electronic structure, crystallographic properties, and defects. XEOL is particularly powerful for studying luminescence in materials with diverse applications, such as semiconductors, phosphors, and luminescent markers. The technique's ability to probe the local environment of specific elements (XANES-XEOL) [78] [79], investigating the luminescence as the energy varies around the absorption edges of a specific element, and capture information on electronic transitions makes it valuable for understanding the intricate details of materials' behavior.

One notable advantage of XEOL is its capability to provide spatially resolved information. By utilizing advanced X-ray microscopy techniques, researchers can create spatial maps of luminescence across a sample, enabling the visualization of variations in the electronic and optical properties at the nanoscale. This spatial resolution is crucial for investigating heterogeneous materials or nanostructured systems where properties may vary across different regions.

3.1.4 X-ray ptychography - Ptycho

A ptychography experiment consists of illuminating a sample with a coherent beam, systematically scanning it with overlap between the probed regions, and recording continuous diffraction patterns associated with each well-known position (formally, the position must be known with precision equal or better than the aimed resolution). The collected data is then computationally processed to reconstruct high-resolution images (not limited by the probe size, but by the numerical aperture collected in the detector) of both the amplitude and phase of the sample, making it versatile for various fields. Ptychography non-destructive nature, compatibility with different radiation types, and enhanced contrast have enabled breakthroughs in materials science, biology, and nanotechnology, especially due to the suitability for challenging low-absorption contrast materials. Typical experimental constraints are the beam coherence, sample stability, sample preparation, and the detector's pixel size, area, and dynamic range.

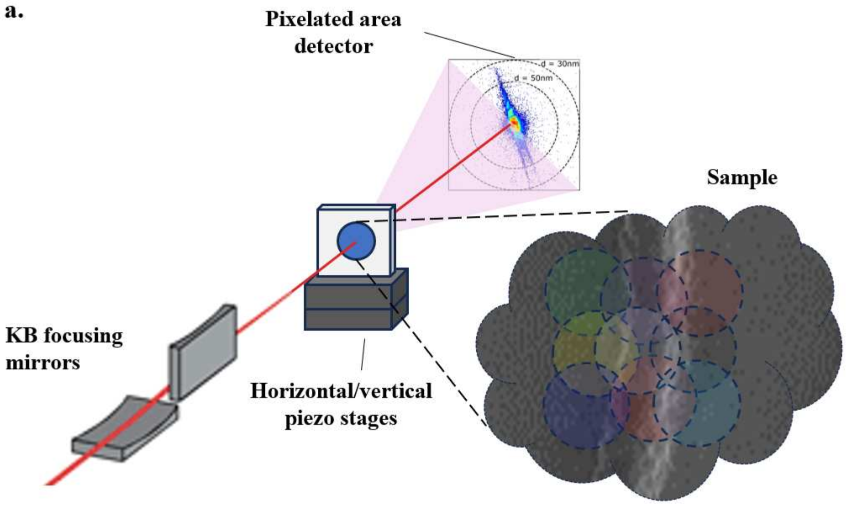

Figure 3.7: Ptychography setup and acquisition. Figure shows the experimental setup composed by a focusing optical element, represented by a Kirkpatrick–Baez (KB) mirror, sample translation stages in the perpendicular directions to the beam, and a pixelated area detector at the far-field regime. A zoom at a region of the sample highlights the beam positions (colored circles) where the diffraction patterns are acquire in which the position is precisely determined. Observe that adjacent regions are overlaped.

From a fundamental description of the technique, one needs to revisit the scalar wave equation or d'Alembert equation, directly derived from the Maxwell equations [80]:

$$\left(\frac{1}{c^2}\frac{\partial}{\partial t} - \nabla^2\right) \cdot \Psi(\vec{r}, t) = 0 \tag{3.4}$$

which accepts the solution as the monochromatic decomposition of the time-independent components Ψ_ω, $\Psi(\vec{r},t) = \int_0^\infty \Psi_\omega(\vec{r})e^{-i\omega t}d\omega$. [81] This decomposition applied to Eq. 3.4, we get the Helmholtz equation:

$$(\nabla^2 + k^2)\Psi_\omega(\vec{r}) = 0 \tag{3.5}$$

Assuming that the radiation sources are over a plane S_0, the solution to Eq. 3.5 is given by the Fresnel-Kirchhoff formula [81] (Figure 3.8.a):

$$\Psi(x) = \frac{k}{2\pi i}\int_{S_0} \Psi_0(\vec{x})\frac{e^{ik|\vec{r}|}}{|\vec{r}|}\cos(\vec{n},\vec{r})dS_0dS, \qquad r >> \lambda \tag{3.6}$$

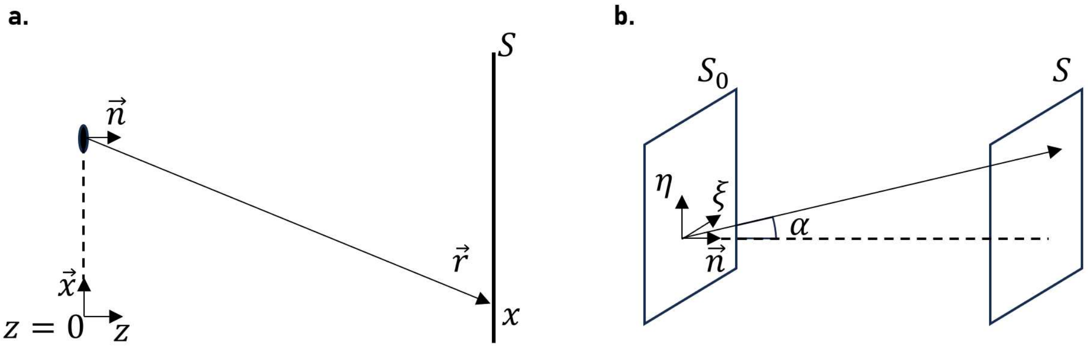

Figure 3.8: Ptychography mathematical modeling reference frame

Similarlly to what Thibault [82] did, we rewrite Equation 3.6 using the coordinates from the source plane S_0, ξ and η, and the incident plane S, x and y, as

$$\psi(x,y) = \frac{k}{2\pi i}\int_{S_0} \Psi_0(\xi,\eta)\frac{e^{ikr}}{r}cos(\alpha)d\xi d\eta$$

Where $r = \sqrt{z^2 + (x-\xi)^2 + (x-\eta)^2}$. So if, $\frac{|\xi - x|}{z} << 1$ and $\frac{|\eta - y|}{z} << 1$,

$$r = z\sqrt{1 + \frac{(x-\xi)^2}{z^2} + \frac{(y-\eta)^2}{z^2}}$$

$$r \approx z\left[1 + \frac{(x-\xi)^2 + (y-\eta)^2}{2z^2} - \frac{((x-\xi)^2 + (y-\eta)^2)^2}{8z^3}\right] \tag{3.7}$$

$$\begin{aligned}\psi(x,y) &\approx \frac{k}{2\pi i}\int_{S_0} \Psi_0(\xi,\eta)\frac{e^{ikr}}{r}\cos\alpha d\xi d\eta \\ &\approx \frac{k}{2\pi i}\int_{S_0} \Psi_0(\xi,\eta)\frac{e^{ikr}}{z}d\xi d\eta\end{aligned}$$

where it was used that for small α, $\cos\alpha \approx 1$ and, consequently, $z \approx r$
Then, focusing on the right side of the equation,

$$\begin{aligned}\frac{k}{2\pi i}\int_{S_0}\Psi_0(\xi,\eta)\frac{e^{ikr}}{z}d\xi d\eta &= \frac{k}{2\pi i}\frac{1}{z}\int_{S_0}\Psi_0(\xi,\eta)e^{ikr}d\xi d\eta\\ &= \frac{2\pi}{\lambda}\frac{1}{2\pi i}\frac{1}{z}\int_{S_0}\Psi_0(\xi,\eta)e^{ikr}d\xi d\eta\\ &= \frac{1}{i\lambda z}\int_{S_0}\Psi_0(\xi,\eta)e^{ikr}d\xi d\eta\end{aligned}$$

Using only the first two terms of the expansion of equation 3.7 for r,

$$\frac{k}{2\pi i}\int_{S_0}\Psi_0(\xi,\eta)\frac{e^{ikr}}{z}d\xi d\eta \approx \frac{1}{i\lambda z}\int_{S_0}\Psi_0(\xi,\eta)e^{ikz\left[1+\frac{(x-\xi)^2+(y-\eta)^2}{2z^2}\right]}d\xi d\eta$$

Which gives the approximation for $\psi(x,y)$:

$$\psi(x,y) \approx \frac{e^{ikz}}{i\lambda z}\int_{S_0}\Psi_0(\xi,\eta)e^{ik\left[\frac{(x-\xi)^2+(y-\eta)^2}{2z}\right]}d\xi d\eta$$

Expanding the exponential, we have:

$$e^{ik\left[\frac{(x-\xi)^2+(y-\eta)^2}{2z}\right]} = e^{\frac{ik}{2z}x^2}e^{\frac{-i\xi xk}{z}}e^{\frac{ik}{2z}\xi^2}e^{\frac{ik}{2z}y^2}e^{\frac{-i\eta yk}{z}}e^{\frac{ik}{2z}\eta^2}$$

And since $\frac{ik}{2z}x_i^2 = \frac{i}{2z}\frac{2\pi}{\lambda}x_i^2 = \frac{i\pi x_i^2}{\lambda z}$, in the limit $F << 1$ (Fraunhofer regime), where F is the Fresnel number defined as $F = \frac{a^2}{\lambda z}$, one can get, $1 \gg \frac{a^2}{\lambda z} \geq \frac{x_i^2}{\lambda z}$, in which case $e^{\frac{ikx_i^2}{2z}} \approx 1$. Where a is the largest dimension of the support of the function Ψ_0, or, experimentally, the largest dimension of a sample, and $x_i = x, y$. And since, $\frac{|\xi-x|}{z} \ll 1$ and $\frac{|\eta-y|}{z} \ll 1$, the last approximation to $\psi(x,y)$ is:

$$\psi(x,y) \approx \frac{e^{ikz}}{i\lambda z}\int_{S_0}\Psi_0(\xi,\eta)e^{-\frac{ik}{z}\xi x}e^{-\frac{ik}{z}\eta y}d\xi d\eta$$

And since outside S_0, Ψ_0 is null,

$$\begin{aligned}\int_{S_0}\Psi_0(\xi,\eta)e^{-\frac{ik}{z}\xi x}e^{-\frac{ik}{z}\eta y}d\xi d\eta &= \int_{S_0}\Psi_0(\xi,\eta)e^{-\frac{i}{z}\frac{2\pi}{\lambda}\xi x}e^{-\frac{i}{z}\frac{2\pi}{\lambda}\eta y}d\xi d\eta\\ &= \int_{-\infty}^{\infty}\int_{-\infty}^{\infty}\Psi_0(\xi,\eta)e^{-\frac{2\pi i}{\lambda z}\xi x}e^{-\frac{2\pi i}{\lambda z}\eta y}d\xi d\eta\end{aligned}$$

Therefore,

$$\psi(x,y) \approx \frac{e^{ikz}}{i\lambda z}\int_{-\infty}^{\infty}\int_{-\infty}^{\infty}\Psi_0(\xi,\eta)e^{-\frac{2\pi i}{\lambda z}\xi x}e^{-\frac{2\pi i}{\lambda z}\eta y}d\xi d\eta \tag{3.8}$$

What gives us, the final definition, through the Fourier transform operator:

$$\psi(x,y) \sim \mathscr{F}(\Psi_0(\xi,\eta)) \tag{3.9}$$

Therefore, if the detector is sufficiently far from the detector (Fraunhofer regime), the wave function acquired corresponds to the Fourier transform of the function that exists from the sample, naively, the product between the function of the object and the probe. If the wave is a unitary plane wavefront, the scattering signal is the Fourier transform of the object. Unfortunately, however, the detectors measure only the intensity of electromagnetic wave ($|\psi|^2$) in the X-ray regime, so that the phase information of ψ is lost. To solve that problem, Sayre [83] showed in 1952 that once one samples the scattered intensity with a factor of at least 2 of the Nyquist frequency (inverse of sample size), commonly known as the oversampling condition, or denser it can yield a unique real space image, as a direct implication of the Shannon theorem. [84] [85] This method was demonstrated as an imaging technique to reconstruct an object from the modulus of its Fourier transform by Fienup in 1978 [Reconstruction of an object from the modulus of its Fourier transform] through the application of an iterative algorithm based on the error reduction in the sense of the squared different between the experimentally acquired intensity (I) and the corresponding modulus of the Fourier transform of the reconstructed object (F), the R_F.

$$R_F = \frac{|I - |F|^2|^2}{|I|^2}.$$

The oversampling condition can be explicitly written as:

$$\mathscr{O} = \frac{R\lambda}{a\Delta x} > 2 \tag{3.10}$$

Where R is the detector sample distance, λ the wavelength of the light, a the size of the support of the sample and Δx is the pixel size of the detector. Practically, the mathematical expression for the oversampling can be interpreted as the ratio between the numbers of the pixels of the sample and the detector.

The iterative algorithms available in the literature [82] have the same main structure described in Figure 3.9. The initial known information that is inputted in the algorithm is the measured amplitude of the sample's Fourier transform (in fact what is measured is the intensity and the amplitude is calculated as the square roots of the measured intensity). A random phase is initially attributed to the inputted amplitude, and the function is inversely Fourier transformed. A few constraints are applied in the real space function and the resulting function in the real space is inversely transformed back to the Fourier space via a Fourier transform and the resulting amplitude is compared to the measured. In this initial iteration, the measured amplitude is probably far from the one obtained via the Fourier transform, and then the new calculated phase is applied to the measured Fourier amplitude and the resulting function is inversely Fourier transformed and this procedure of comparisons is repeated until the difference between reconstructed and measured amplitudes is less than a desired value or, typically, a limit of iterations is reached.

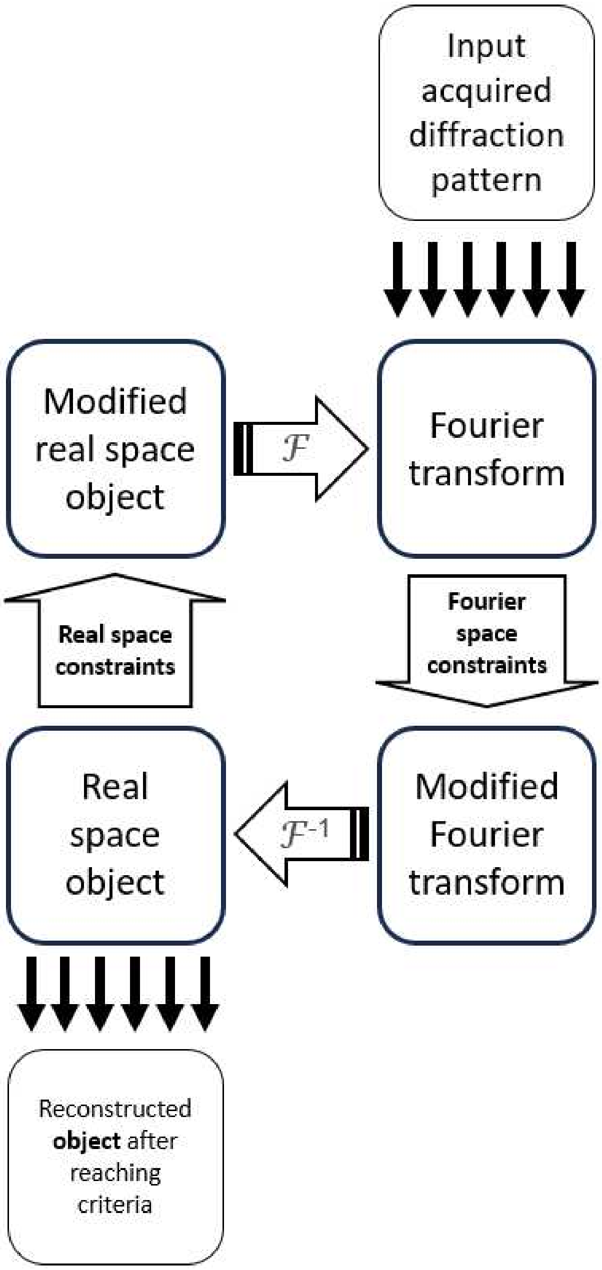

Figure 3.9: Iterative algorithm general structure for phase retrieval in CDI methods

The same phenomenology from diffraction described in the Diffraction subsection (3.1.2) is valid in the CDI experiments. The conventional diffraction experiment is, as discussed, also an interference phenomenon, such as CDI, with the only difference that the coherence is present at the sample (crystal) in the long-range order of the crystal lattice, while in the CDI experiments the coherent characteristics are defined by the X-ray beam. That is why the resolution of the minimum size of the structure can be defined using the same formulation that the Laue equation describes.

Formally, we assume an object with size σ at a distance R from the detector with N pixel with size Δx in each direction. (Figure 3.10) The maximum half angular aperture acquired by the detector is $2\theta = \arctan(N\Delta x/2R)$, and therefore the correspondent value for σ is:

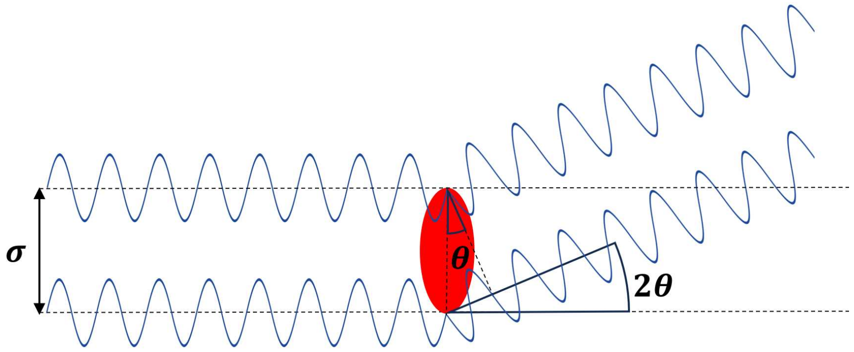

Figure 3.10: Scattering scheme for pixel size determination

$$q_{MAX} = \frac{4\pi \sin\left(\frac{2\theta}{2}\right)}{\lambda}$$

$$\sigma_{MIN} = \frac{d_{MIN}}{2} = \frac{\pi}{q_{MAX}} = \frac{\pi\lambda}{4\pi \sin\left(\frac{2\theta}{2}\right)} = \frac{\lambda}{4\sin\left(\frac{1}{2}\arctan\left(\frac{N\Delta x}{2R}\right)\right)}$$

That expression for σ gives the minimum size of the object that can be theoretically analyzed with the quantized form of the signal due to the pixelated nature of the detector and corresponds to the pixel size of the reconstructed object. An extra approximation using the information that $N\Delta x << 2R$ allows the estimative for the pixel size in the form:

$$\sin\left(\frac{1}{2}\arctan\left(\frac{N\Delta x}{2R}\right)\right) \approx \frac{N\Delta x}{4R}$$

$$\sigma \approx \frac{\lambda R}{N\Delta x} \tag{3.11}$$

That is the fundamental description of the coherent diffractive imaging (CDI) techniques, which can be separated in a few variations such as: plane-wave CDI (pwCDI), ptychography, BraggCDI, ptycho-tomography and others. This work will focus only in ptychography, and the other techniques can be reviewed elsewhere [86] [87] [88].

It is important to highlight however that this value for σ does not correspond to the final resolution of the reconstruction, only to the pixel size. The methods for evaluating the final resolution can be the same as used in other techniques, such as the edge width of the features of the reconstruction, the Fourier shell correlation [89], and others.

In the ptychography technique, an object is scanned by a probe with dimensions smaller than the object with an overlap between the adjacent points. At each point, the correspondent coherent diffraction pattern is acquired. The redundancy in the data created by the overlapping between the allows more robustness in the reconstruction algorithms, and it is applied as follows: during the obtaining of the real space object the constraint implied over the object is that within the overlapped region between two adjacent acquisition points must be the same. Different algorithms of reconstruction can be used with the same data set, and in combinations in order to achieve optimal reconstructions. In this work, we will exclusively use the alternating projections (AP) [90] and relaxed averaged alternating reflections (RAAR) [91].

3.1.5 Fourier transform infrared - FTIR

Fourier Transform Infrared Spectroscopy (FTIR) is a analytical technique employed for elucidating the molecular composition and structural characteristics of materials. Fundamentally, FTIR relies on the interaction between infrared (IR) radiation and molecular entities, resulting in the selective absorption of specific wavelengths of light. This interaction is predicated upon the vibrational and rotational modes inherent to molecules, which undergo alterations in energy states upon absorbing IR radiation. Notably, the vibrational frequencies of chemical bonds within molecules are distinctive, allowing for their identification within the resultant infrared absorption spectrum.

In FTIR spectroscopy, a broad spectrum of infrared wavelengths is directed through the sample under investigation. As the IR radiation traverses the sample, certain wavelengths are absorbed by the molecular bonds, leading to a diminution in their intensity within the transmitted light. The recorded data, typically in the form of an interferogram representing the amplitude of IR radiation over time, undergoes Fourier transformation to yield a frequency-domain spectrum. This spectrum encapsulates the intensity of IR radiation across different frequencies (or wavelengths), facilitating the identification and characterization of molecular vibrations.

FTIR spectroscopy offers flexibility in acquisition modes, primarily employing transmission and reflection configurations. In transmission mode, the IR radiation passes through the sample, enabling analysis of materials in various forms such as liquids, solids, and thin films. This mode is particularly suitable for transparent or semi-transparent samples. Conversely, reflection mode spectroscopy, the sample is positioned over a highly reflective surface, causing the infrared beam to cross the sample twice, effectively increasing the path length and enhancing absorption, in other words, it exploits the increased path length within the sample to enhance absorption. This increased path length allows for a more sensitive detection of absorption features, particularly beneficial when dealing with low absorption materials. In this work, data was solely acquired in reflection mode and the dataset were acquired at IMBUIA beamline at Sirius-LNLS synchrotron [92].

CHAPTER 4

DEVELOPED METHODOLOGY TO STUDY X-RAY DOSE EFFECTS AND TO MITIGATE DAMAGE

Metal halide perovskites (MHP) exhibit challenges related to their stability under diverse conditions, necessitating the utilization of sophisticated investigative tools. The impact of X-ray damages on halide perovskites has been a subject of both research interest and concern. Given that X-rays are high-energy photons, they can instigate various effects on materials, particularly halide perovskites [[16] [93] [94]]. A comprehensive understanding of these effects is imperative for the effective application of X-ray-based characterization techniques. A prominent concern pertains to radiation damage, where high-energy X-rays can generate defects in the crystal lattice of halide perovskites. This damage may manifest as the displacement of atoms or the creation of vacancies, thereby impacting the structural integrity of the material [[95]]. In instances where halide perovskites are employed in solar cells or optoelectronic devices, radiation-induced defects can adversely affect the long-term performance and stability of these devices [[16] [96]]. Furthermore, X-ray exposure can contribute to the degradation of halide perovskites, leading to alterations in their optical and electronic properties. The formation of defects, such as halide vacancies or interstitials, has the potential to modify the band structure and electronic properties, thereby influencing the optoelectronic performance of the material [[93]]. In efforts to mitigate X-ray damages in halide perovskites, researchers routinely optimize experimental conditions, adjusting parameters such as X-ray energies, exposure times, and the overall experimental setup. Additionally, protective measures, such as encapsulating perovskite samples or conducting experiments under controlled atmospheres, are implemented to minimize undesired effects.

This study explores the effects of focused X-ray beams on MHP through a multi-technique approach. The irradiation predominantly affects iodine and organic components, altering their quantities. A distinctive feature that we observed is the development of an excavated area, signaling the presence of an optically inactive metal layer. Notably, the bulk material remains unchanged, preserving the initial halide composition, as evidenced by stable photoluminescence emission energy. The controlled administration of X-ray doses and environmental conditions proves effective in mitigating damage. Consequently, it was employed these optimized conditions in X-ray ptychography, achieving an unprecedented 17.4-

nm spatial resolution.

Understanding and controlling X-ray-induced damages in halide perovskites are essential for advancing the reliability and applicability of X-ray-based characterization techniques in studying these promising materials.

4.1 Sample preparation

The CsFAMAPb(I,Br)$_3$ perovskite with composition $[(FAPbI_3)_{0.87}(MAPbBr_3)_{0.13}]_{0.92}\ (CsPbI_3)_{0.08}$ was deposited by the antisolvent method on polished Si substrates covered with 100 nm of Au. The substrates were cleaned with isopropanol and ultraviolet-ozone (UVO) treated for 30 min before the deposition. The perovskite solution was prepared using FAI (GreatCell Solar Materials), MABr (GreatCell Solar Materials), PbI_2 (TCI America), $PbBr_2$ (TCI America), and CsI (TCI America) with a concentration of 0.7 M regarding Pb component. The powders were dissolved in a mixture of anhydrous N, N-dimethylformamide (DMF, Sigma-Aldrich), and dimethyl sulfoxide (DMSO, Sigma-Aldrich) with a volume ratio of DMF:DMSO = 4:1 at room temperature. The solution was spin-coated at 2000 rpm for 12 s followed by 5000 rpm for 30 s. 15 s before the end of the spin-coating, 150 µL of chlorobenzene was dropped on the film. After deposition, the substrates were thermal annealed for 60 min at 100 °C. The $Cs_{0.05}FA_{0.95}PbI_3$ was deposited by the gas quenching method on the Mylar substrate. [97] The substrates were cleaned with UVO treated for 30 min before deposition. The perovskite precursor solution was prepared by solubilizing CsI (TCI America), FAI (GreatCell Solar Materials), PbI_2 (TCI America) and 40 mol% of MACl, with an excess of 5% of the lead source, in the mixture of solvents DMF (Sigma-Aldrich) and methylpyrrolidone (NMP, Sigma-Aldrich) (v:v = 4:1) with a concentration of 1.3 M. The solution was spin-coated at 4000 rpm for 60 s. A jet of N_2 was automatically blown during the final 50 s of the rotation to force the solvent's exit and the perovskite's subsequent crystallization. The film was then heated at 100 °C for 90 minutes in the air. All the samples were prepared at the LNES-IQ/UNICAMP by collaborators.

4.2 Beam damage

Metal halide perovskite (MHP) materials have garnered significant attention for their application in solar cells, [98] [99] photonic devices, [100] [101] and X-ray detectors. [102] However, many aspects of their properties must be elucidated to transition these technologies from the laboratory to the market. [103] The operational instabilities of MHPs and the associated photo-structural-chemical transformations necessitate advanced characterization tools, coupled with in situ and operando experiments, to achieve a comprehensive nanoscale understanding. [14] Focused beam X-ray fluorescence (XRF), [104] X-ray diffraction (XRD), [105] [106] X-ray beam-induced current (XBIC), [107] X-ray excited optical luminescence

(XEOL), [16] and coherent diffraction imaging (CDI), [108] increasingly sophisticated and accessible at fourth-generation synchrotron sources, serve as powerful tools for investigating MHPs, including complete perovskite solar cells (PSCs). However, in most cases, these tools strongly interact with the materials, leading to undesirable transformations. Despite their promise, focused X-ray-based techniques face challenges related to high radiation doses deposited on the samples, potentially causing damage to the materials and devices and altering their properties. Stuckelberger et al. [96] demonstrated that the electronic properties of perovskites are highly sensitive, resulting in a significant reduction in the XBIC signal under X-ray irradiation without evidence of changes in the element's composition. X-ray photoemission (XPS) experiments also highlighted the sensitivity of electronic properties, suggesting that the organic part of the perovskite (formamidinium (FA) and methylammonium (MA)) undergoes radiolysis, producing volatile species. [94] [109] Orri et al. revealed that the degradation mechanism induced by electrons and X-rays is similar and likely caused by the interaction of electrons, generated by X-rays, with the organic part of the MHP. Even low doses of electrons in defective grain boundaries lead to changes in grain orientation. [95] Additionally, the degradation appears to be facet-dependent, emphasizing the importance of sample crystalline quality in resilience to X-ray damage. [110] Intriguingly, cryogenic conditions do not prevent degradation but rather favor sample amorphization. [111] [112] Conversely, temperatures around 90 °C do not induce additional severe perovskite degradation. [111] Despite the critical insights gained, a comprehensive investigation of all aspects of X-ray doses on the morphological, structural, and chemical properties of MHP films extensively used in PSC devices is still lacking.

In this initial methodological section of the study, we employed a correlative multi-technique approach to examine the impact of a focused X-ray beam on the distribution of elements, morphology, structure, and optoelectronic properties of the $[(FAPbI_3)_{0.87}(MAPbBr_3)_{0.13}]_{0.92}(CsPbI_3)_{0.08}$ ($CsFAMAPb(Br,I)_3$) compound. This composition is significant as it is widely employed in fundamental studies and devices, representing a mixture of the main elements/molecules used in MHP. The samples underwent controlled X-ray irradiation under diverse atmospheres and temperatures, and the resulting damage was assessed using correlative multiple micro and nanoscale techniques. The correlative data revealed that the X-ray dose induced damage on the exposed surface, primarily affecting the iodine and organic elemental components, leading to topographical changes by extracting material and forming an excavated area. Local optical properties within this area indicated the formation of a metallic layer coating the surface. Surprisingly, the bulk material retained its optoelectronic properties even under more severe doses. As anticipated, reducing the X-ray dose and utilizing an inert atmosphere mitigated the damage. However, the selective extraction appeared independent of temperature conditions. We demonstrated that combining an inert atmosphere with a controlled dose reduction at room temperature is the optimal approach for investigating hybrid organic-inorganic MPHs with state-of-the-art X-ray nanoprobes. Finally, the optimized conditions were applied below the critical dose to showcase the feasibility of studying MHPs using the X-ray ptychography (CDI) technique, highlighting grain morphology and sample details with a 17.4-nm spatial resolution. Notably, this technique had not been reported before in these compounds.

The experiments employed the CsFAMAPb(I,Br)3 sample for all assessments, except for the ptychography measurements conducted on the $Cs_{0.05}FA_{0.95}PbI_3$ sample. Under consistent environmental conditions (RT-Air, RT-N2, or Cryo-N2), all X-ray measurements were conducted on the same compound, deposited on an Au-coated Si substrate, approximately 10×10 mm in size, which was sectioned into small pieces. Three distinct pieces were selected, each used for a specific environmental condition. Different areas spaced by 50 μm were measured, forming an array with varying doses. Positioned at the experimental station, the samples faced a 500×200 nm^2 X-ray beam at the Tarumã Station on the Carnaúba beamline. [3] The acquisition of nano-XRF involved irradiating the samples with 10 and 14 keV X-ray energies, employing a fly scan mode, where the beam continuously traversed the sample, collecting signals. For instance, a 10 μm beam walk with 100 collected points corresponded to 100 nm. The resulting data were referred to as steps of the fly scan. At each (x, y) coordinate, an XRF spectrum was obtained, and custom Python scripts were used to generate nano-XRF maps integrating selected XRF signal peak emissions. Maps were derived from emissions I-Lα1 (3938 eV), Pb-Lα1 (10551 eV), and Br-Kα1 (11924 eV). XRF spectra for 10 and 14 keV, along with corresponding peaks, are illustrated in Figure 4.1. The 10 keV facilitated beam damage assessment and I maps, while the 14 keV was utilized for obtaining Pb and Br maps. Cryogenic conditions for RT-N_2 and Cryo-N_2 experiments involved a constant N_2 flow at room temperature and cold N_2, respectively. [113] Experiments with reduced doses involved changing the undulator phase to reduce the X-ray flux. Following synchrotron experiments, samples were stored in a vacuum and dry box with a drying agent until subsequent characterizations. Three distinct X-ray fly scans were employed to obtain various doses in the same 5x5 um total area. For 2.9 GGy, the step size was 100 nm, exposure time 200 nm, and 750 ms per point. For 1.9 GGy, the step size was 60 nm with a exposure time of 58 ms. For 0.7 GGy, the step size was 50 nm, and exposure time was 8 ms. Areas subjected to irradiation were examined with a 10x10 um scan, step size of 100 nm, and exposure time of 7.5 ms. Further details about the scans are outlined in Table 4.1. The iodine reduction ratio was calculated by the average intensity of a 2×2 μm area at the center of the irradiated region, presenting an error of ± 15% estimated from multiple images due to statistical fluctuations.

Figure 4.2a illustrates a 5 × 5 μm^2 nano-XRF map of iodine obtained at room temperature in an air atmosphere (RT-Air). For sample irradiation and mapping, the fly-scan snake mode was employed, initiating the scan at the left-bottom corner of the image, with the beam spot moving up and down while sliding to the right relative to the sample. The X-ray dose post-irradiation corresponds to approximately 2.9 GGy deposited in the scanned region, where 1 Gy = 1 J/kg measures the total energy deposited per unit of material irradiated. [114] The estimated dose considers the compound's total absorption at the irradiation energy, ensuring doses deposited using different X-ray energies can be accurately compared. The total absorbed 10 keV photons by the 330 nm thick perovskite film amount to 2.53×10^{21} ph/m^2. The dose calculation and its Python code are presented in Appendix G.

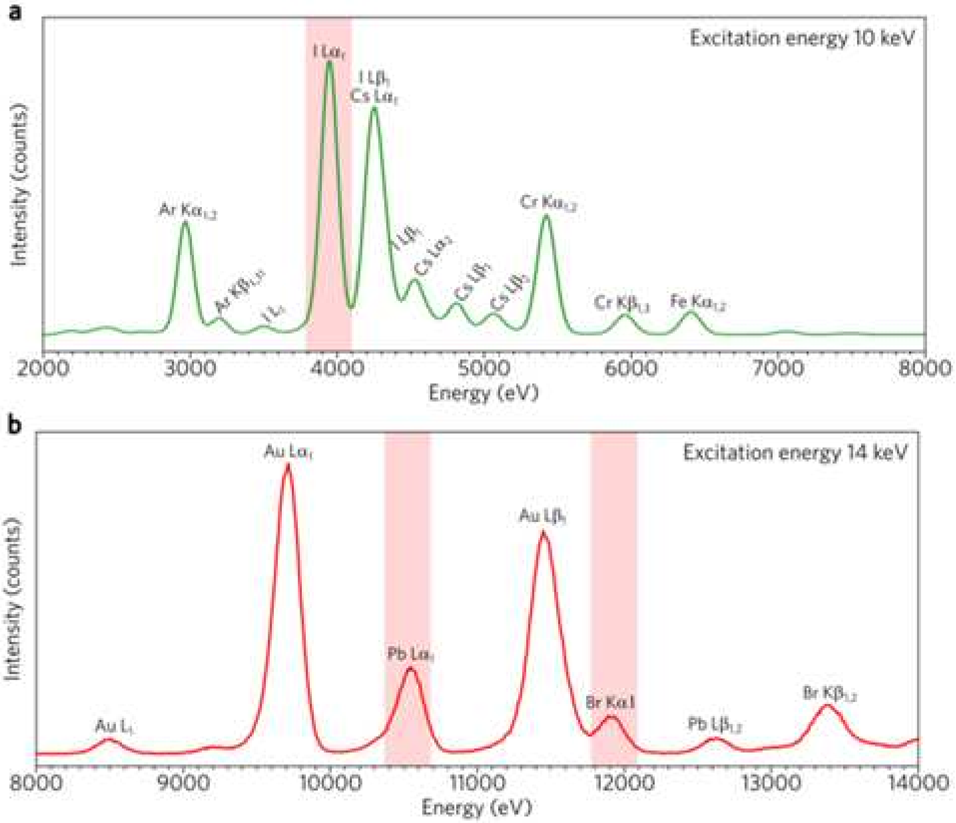

Figure 4.1: X-ray fluorescence spectrum obtained with X-ray excitation energy of (a) 10 keV and (b) 14 keV. The spectrum from each pixel was squeezed to obtain the spectrum shown here. The highlighted peak region was used to obtain the nano-XRF maps.

A noticeable effect in Figure 4.2a a is the diminishing iodine fluorescence emission in the left-to-right scan direction. This gradient is not incidental but consistently observed in different samples under comparable doses (Figure 4.3). It can be interpreted as a yanking-out effect caused by the X-ray beam on the surface, depleting iodine. Since the horizontal nanoprobe (500 nm in size) surpasses the fly-scan step (200 nm), the initial irradiation (first vertical lines) impacts a pristine sample. In contrast, the subsequent vertical lines have already encountered the beam, resulting in some material loss. The iodine consumption in the irradiated region is more pronounced in Figure 4.2b. To examine the irradiated region, a larger 10x10 μm^2 scan was performed, centered at the same point as the 5x5 µm^2 one but with a much lower dose, around 0.2 GGy in the entire scanned region, representing approximately 7% of the dose in the former scan. The iodine map reveals a reduction in the number of iodine atoms within a square of the exact dimensions of the previously irradiated region. The average fluorescence counts indicate about a 28% decrease. Interestingly, the Pb and Br

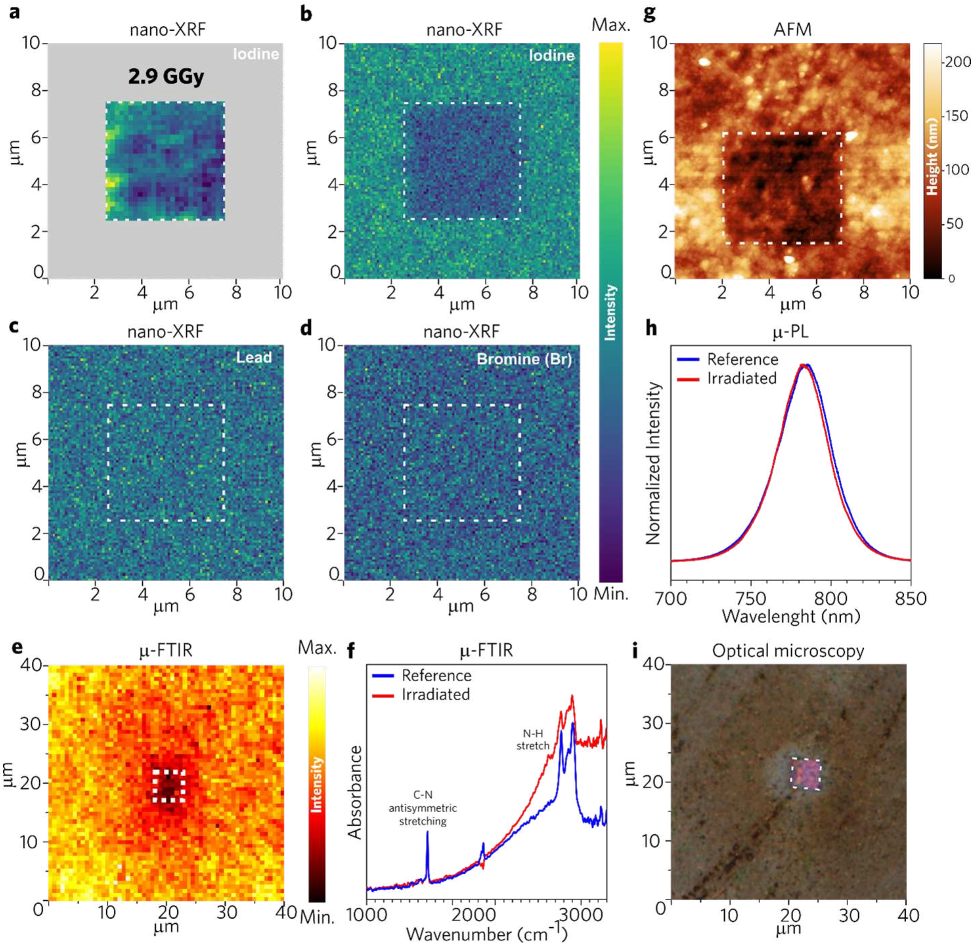

Figure 4.2: Effect of raster scan in a perovskite sample by an X-ray focused beam in the air at room temperature by multi techniques. (a) Iodine nano-XRF map with a high X-ray dose. (b-d) Iodide, lead, and bromide, respectively, nano-XRF maps of the irradiated area. (e) C-N antisymmetric strecting (1700 cm-1) μ-FTIR map, (f) FTIR spectra, (g) AFM topography image, (h) photoluminescence spectra, and (i) optical image of the irradiated sample.

maps exhibit no evidence of composition changes (Figure 4.2c-d).

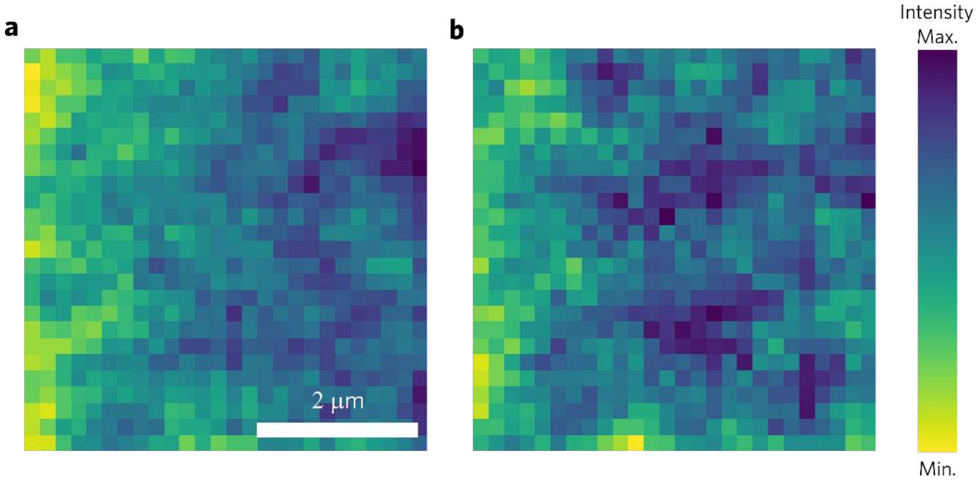

Figure 4.3: Iodine nano-XRF map obtained with the energy of 10 keV and total absorbed dose of 2.9 GGy in two different new regions of the sample.

Given that the hybrid organic-inorganic perovskite comprises a mixture of MA and FA, unobservable by XRF, the impact on the organic segment was assessed using µ-FTIR. Figure 4.2e displays a µ-FTIR map obtained by integrating the C-N antisymmetric stretching vibration (1700 cm^{-1}) of the FA molecules. [115] The reduced intensity in the X-ray irradiated region suggests the removal or degradation of FA molecules in the same area as iodine. A comparison of the complete FTIR spectra in the inner damaged region with the outer part (reference) reveals a change in the background for higher wavenumbers (Figure 4.2), indicating a compound with more metallic characteristics and a different refraction index on the sample surface. This hypothesis is also qualitatively supported by a distinct color observed in the optical microscopy image shown in Figure 4.2i. AFM measurements unveil the impact of the beam on the film topography (Figure 4.2g), displaying a reduction in film depth in the irradiated area, consistent with the material consumption observed for iodine and organic molecules. It was anticipated that the decline in iodine and organic cations content would induce a change in PL peak position. However, the PL peak in the irradiated region remains stable in shape and position, with decreased intensity attributed to a decrease in sample thickness. Figure 4.2h, illustrating the PL spectra acquired using a µ-PL instrument with a spot size of 1 µm, indicates that the remaining perovskite compound retains its bandgap properties. The decrease in intensity is visualized in a PL line scan through the damaged area, as shown in Figure 4.5.

4.3 Beam damage control

4.3.1 Dose effect

The impact of the total X-ray dose was initially examined under room temperature and air atmosphere (RT-Air) conditions, maintaining a constant photon flux resulting in an absorbed dose rate of 4.7 KGy/s over a film area of 5x5 μm^2. The irradiation time was adjusted to achieve three distinct dose levels in the samples: 2.9 GGy (as illustrated in previous results in Figure 4.2), 1.9 GGy, and 0.7 GGy. Additionally, the 10x10 μm^2 inspection, corresponding to 0.2 GGy, was performed, as mentioned earlier. The associated number of 10 keV photons is detailed in Table 4.1. The dataset in Figure 4.4a is identical to that in Figure 4.2 but is once again presented alongside two new datasets with medium and low doses (Figure 4.4b-c) for comparative analysis.

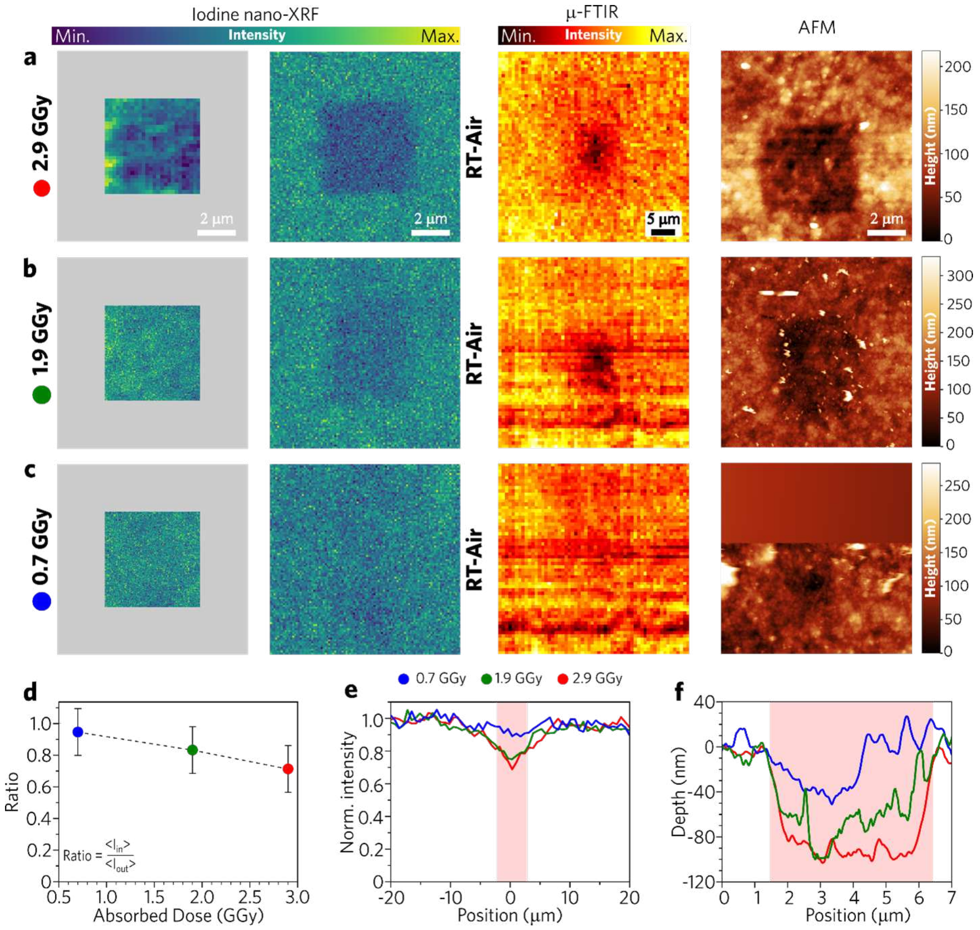

Figure 4.4: Absorbed dose effect in air atmosphere. From left to right, nano-XRF damage scan, nano-XRF probe scan, C-N antisymmetric stretching μ-FTIR, AFM and optical images for doses of (a) 2.9 GGy, (b) 1.9 GGy, and (c) 0.7 GGy. (d) Attenuation in the iodine content, (e) μ-FTIR intensity and (f) AFM profiles for the different doses.

The levels of 1.9 GGy and 0.7 GGy (Figure 4.4b and Figure 4.4c, respectively) result in a reduction of iodine consumption, with the diminishing effect becoming more pro-

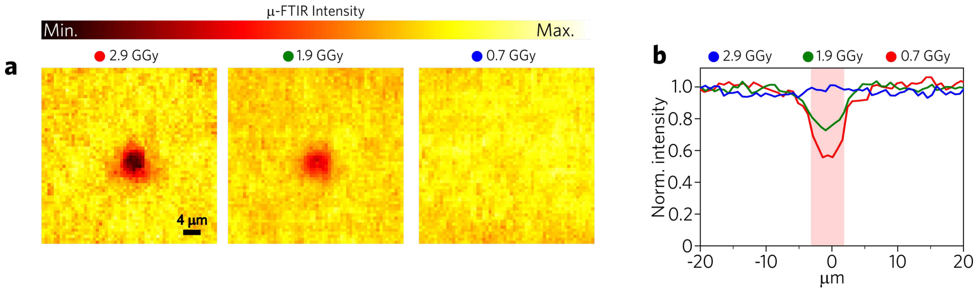

Figure 4.5: (a) μ-FTIR maps of the perovskite obtained integrating N-H stretch vibrations (3100-3400 cm-1) for different X-ray beam doses in air, and (b) profile of the damaged area. Despite the smaller spatial resolution of the μ-FTIR at resonance 1700 cm-1 it was chosen this one for a more quantitative analysis because the changes in the background in this region are negligible. On the other side, the 3100-3400 cm-1 region shows a change in the background, then becomes difficult for a quantitative analysis using these resonances.

Total absorbed dose for each scan				
Energy (keV)	Area($\mu m \times \mu m$)	Total time (s)	GGy	Total absorbed photons ($\times 10^{21}$ ph/m^2)
10	5 × 5	610	2.9	2.53
10	5 × 5	410	1.9	1.70
10	5 × 5	150	0.7	0.62
10	10 × 10	172	0.2	0.18
10	10 × 10	171	0.0015	0.0013
14	10 × 10	171	0.0013	0.0084

Table 4.1: Total absorbed dose for each scan

nounced as the total deposited dose decreases. Comparing the ratio of iodine fluorescence in a 1x1 µm² area in the inner and non-irradiated regions, it is evident that the highest dose causes iodine consumption of about 28%, reduced to 16% at 1.9 GGy, and further to 5% at 0.7 GGy (Figure 4.4d).

Regarding the organic cations, the μ-FTIR map (Figure 4.4a-c, FTIR column) exhibits the anticipated trend of decreasing beam damage with a smaller amount of energy deposited on the sample, showing mitigation as the beam is attenuated by a factor of 4 (0.7 GGy dose). This trend is evident when evaluating the integrated profile at the 1700 cm^{-1} resonance (C-N antisymmetric stretching) in the irradiated region, resulting in about a 30% decrease for the two highest doses and being absent for the smallest one (Figure 4.4e). The profile displays an intensity reduction broader than the irradiated area (pink column), attributed partially to the limited spatial resolution at 1700 cm

The decrease in iodine concentration in the irradiated region and the diminishing signal from FA align with the excavation observed in that area. The overall thickness of the perovskite, measured using a profilometer, is 330 nm and was compared to the depth observed in the AFM topographic images (Figure 4.4f). The total depth and the ratio of excavation relative to the entire film thickness are estimated to be 90 nm (27%), 70 nm (21%), and 15 nm (5%) from the highest to the smallest dose, respectively. These ratios align with the iodine attenuation shown in Figure 4.4d. It's worth noting that error bars for these measurements fall within 15%, as indicated by the statistical fluctuations outside the irradiated

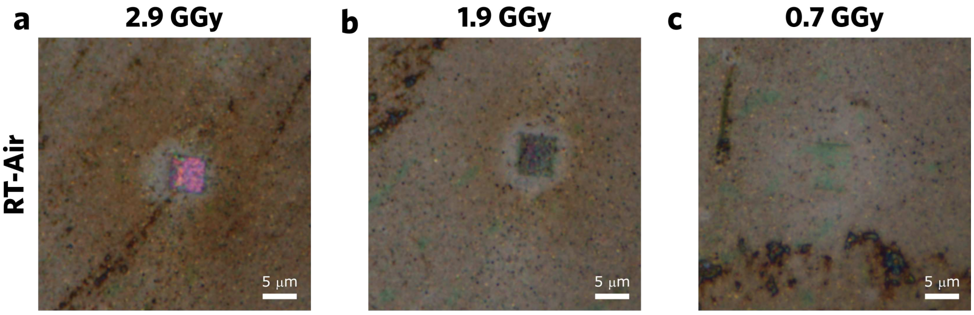

Figure 4.6: Optical microscopy images for different doses (a) 2.9 GGy, (b) 1.9 GGy and (c) 0.7 GGy obtained in air and room temperature.

area. Interestingly, a transition in color is observed from the highest to the lowest dose, shifting from a pinkish tone to a dark greenish hue to an almost imperceptible light green (Figure 4.7). Such color changes may result from a combination of effects, including variations in sample thickness and the formation of a thin metallic layer.

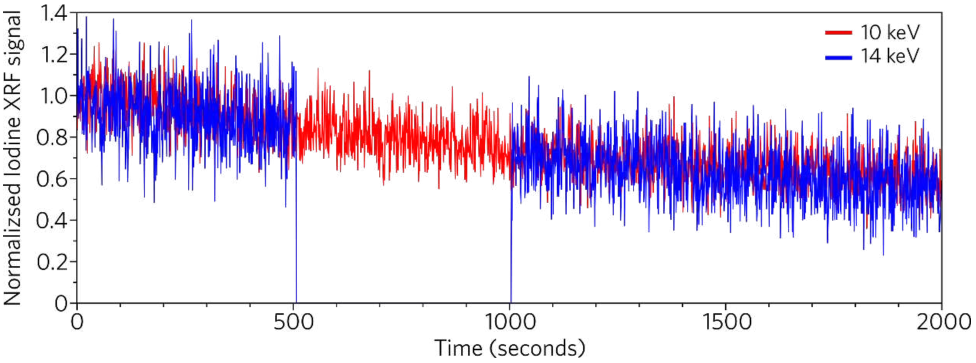

Figure 4.7: Optical microscopy images for different doses (a) 2.9 GGy, (b) 1.9 GGy and (c) 0.7 GGy obtained in air and room temperature.

These experiments were conducted with the same dose rate while varying the exposure time. To investigate the relevance of dose rate versus total dose, the iodine fluorescence signal was measured over time at a fixed sample position for two different dose rates (1.2 and 0.23 GGy/s) at an energy of 10 keV. Figure 4.8a reveals that the higher dose rate results in the expected faster decay in iodine content. However, when examining iodine consumption not as a function of time but as a function of the total absorbed dose (Figure 4.8b), it becomes apparent that the iodine decays for both dose rates overlap.

The decaying signal fits with two exponential components for both dose rates, yielding similar decay coefficients: 972 and 28 GGy^{-1} for 1.2 GGy/s; and 916 and 36 GGy^{-1} for 0.23 GGy/s. This suggests that two main processes occur independently of the dose rate. A plausible hypothesis is that free surface excavation is faster initially, but once a certain quantity of material is depleted and a thin coating layer is formed (evidenced by the FTIR broadband and optical images - Figure 4.9), the process slows down. However, additional experiments are required to confirm this hypothesis. This experiment also illustrates that reducing the dose rate is ineffective in mitigating beam damage in the air. What matters is the integrated absorbed dose needed to extract reliable information from X-ray techniques.

For completeness, a similar experiment was conducted at two different photon energies, 10 and 14 keV, below and above the Pb and Br absorption edges. The X-ray fluxes were controlled to achieve the same absorbed dose rate at both energies, accounting for absorption and photon energy variation. Figure 4.9 demonstrates that the variation in iodine content is the same for both X-ray energies when the absorbed dose is equal, affirming that the total dose absorbed by the material is the determining control factor for iodine consumption in air and at room temperature.

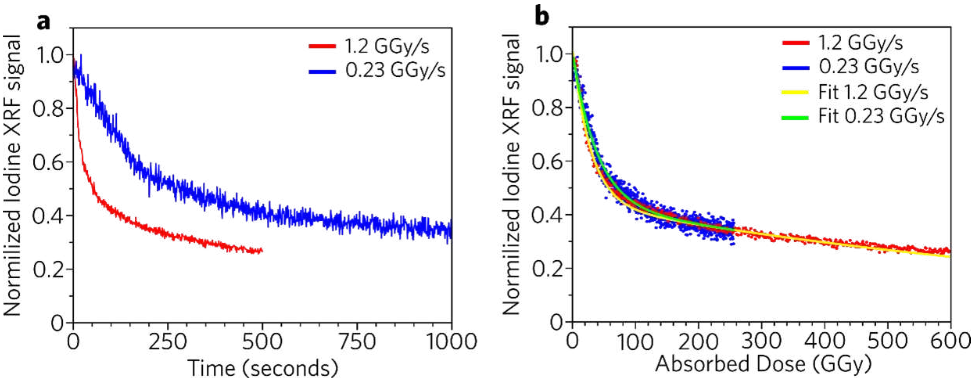

Figure 4.8: Effect of the absorbed dose rate on iodine signal with the X-ray beam in a fixed position for two different absorbed dose rates. (a) Normalized iodine XRF signal in function of (a) time and (b) the dose.

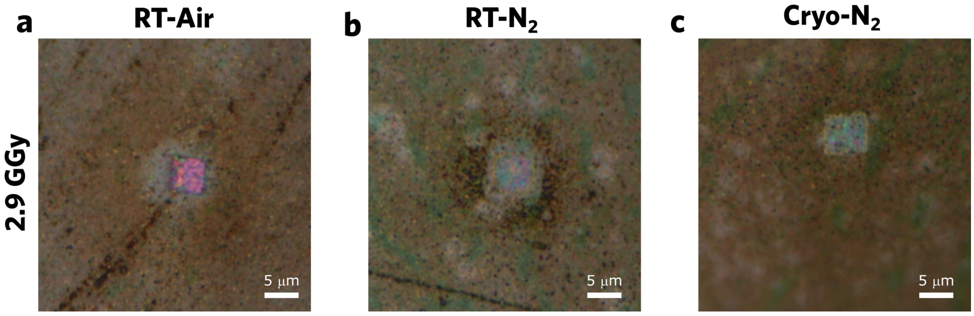

Figure 4.9: Optical microscopy images for environment and temperatures (a) RT-Air, (b) RT-N2 and (c) Cryo-N2 obtained with the dose of 2.9 GGy.

4.3.2 Environmental effect

The atmosphere and temperature conditions were investigated as an alternative strategy to mitigate the beam damage. The same dose conditions (2.9, 1.9, and 0.7 GGy) were applied in three different environmental conditions: room temperature and air atmosphere (RT-Air), RT and nitrogen flow (RT-N2), and cryogenic temperature (152K) and N2 flow (Cryo-N2). The RT-Air condition corresponds to previously discussed measurements (Figure 4.2 and Figure 4.4). At the 2.9 GGy and RT-N2 conditions, a faint irradiated area (with no lateral gradient) was observed (Figure 4.10a, XRF columns), yielding an iodine quantity reduced by about

16% (Figure 4.10c), which is less compared to the same dose and RT-Air conditions (Figure 4.4). The Cryo-N2 condition (Figure 4.10b, XRF columns) seems to mitigate the effect in the XRF maps, with no observable inorganic yanking out in the scanned region within the error bar of ±15%. The Cryo-N2 condition seems to freeze the iodine mobility. Surprisingly, the damage persists in the organic part for both RT-N2 and Cryo-N2 (Figure 4.10a-b, μ-FTIR column), with similar intensity (Figure 4.10d). The AFM topography (Figure 4.10a-b, AFM column) confirms that the inert atmosphere does not entirely mitigate the beam excavation. An additional effect observed in the Cryo-N2 condition is the formation of cracks in the irradiated region, probably caused by the decreased ionic mobility that tends to relax some stress. Lastly, the optical inspection (Figure 4.9) shows that the irradiated regions changed color as previously. However, none presented the intermediate dark greenish, as before. Both inert atmosphere conditions showed a soft light greenish, like in the lowest dose of 0.7 GGy in air. This observation is essential once it indicates that the color change is, at least, not exclusively related to the thin film thickness variation and probably depends on the layer compound formed on the surface.

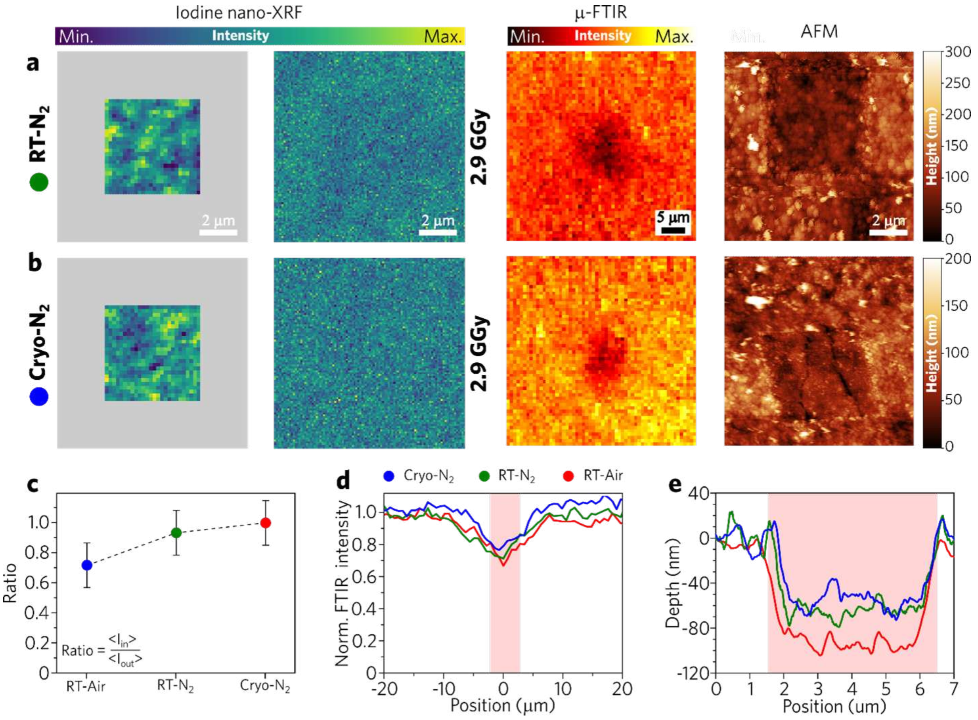

Figure 4.10: Effect dose and atmosphere on damage from an X-ray dose of 2.9 GGy. From left to right, nano-XRF damage scan, nano-XRF probe scan, μ-FTIR, AFM and optical images for samples measured at (a) room temperature and nitrogen obtained by a nitrogen flow, and (b) cryogenic temperature and nitrogen obtained using a cold nitrogen flow.) (c) Attenuation in the iodine content, (d) μ-FTIR intensity and (e) AFM depth profiles for the different conditions.

The high X-ray dose applied to the hybrid organic-inorganic MHP results in selective yanking out of ions at the film surface, leading to the consumption of iodine and organic cations while preserving the Pb and Br composition. This process causes excavation and alters the visible optical surface properties. As anticipated, limiting the X-ray dose significantly reduces damage, almost completely mitigating iodine and organic molecule consumption. Under a similar dose but with a nitrogen (N_2) atmosphere, all damage effects are diminished, indicating the relevance of an inert atmosphere in mitigating iodine yanking from the sample. It suggests that air components (O_2 and H_2O) play a role in iodine removal. The efficacy of a nitrogen atmosphere in reducing damage has been previously documented in these compounds. [16] However, even in an inert atmosphere, damage persists under the 2.9 GGy dose, emphasizing the importance of avoiding such a critical dose when investigating these compounds.

A time-extended observation of the dose and environmental effects on a control sample can be observed in Figure 4.11. A single position on the sample was continuously irradiated by the 500(H) × 200(V) μm^2 beam of Carnaúba beamline, absorbing a dose of 70 GGy per minute. At every minute, the iodine distribution was monitored by the 10 × 10 μm^2 map. This measurement was performed in three environmental conditions with duplicates. The damaged region is larger than the beam size, indicating that the beam damage has a larger extension than the irradiated region for higher doses. Moreover, the damage gets extended at every increase in the dose deposited, an additional observation to reinforce the conclusion that the total dose is, indeed, the determinant parameter concerning sample damage.

Furthermore, the change in the atmosphere is an important factor in spatially controlling the beam damage, reducing the area where the iodine content varies with the deposited doses. In air, the whole 10 × 10 μm^2 presents a decrease in the total amount of iodine, while the impacted area is reduced to less than 2 × 2 μm^2 in dry atmospheres. Figure 4.12 shows the relative variation of the iodine content in a 1 × 1 μm^2 square the center concerning the initial iodine fluorescence counting at a 1 × 1 μm^2 square in the top left of the initial state of the sample. The iodine content suffers a reduction of 60% in air atmosphere after 9 minutes (630 GGy) of irradiation, while RT-N_2 atmosphere can reduce this variation to <40%, and full mitigation is achieved in one of the experiments in cryogenic conditions. This is an important observation for this part of the work that aims to find the optimal conditions of experiments in the Carnaúba beamline since a typical XANES spectrum acquisition in Tarumã station takes around 4 minutes, and, at this time, cryo- and RT- N_2 atmospheres shown minimal damage on the sample concerning the variation in the iodine content, what makes this technique feasible and applicable to this materials in safe conditions.

An additional observation in includes the fact that the damage does not only extends to an area larger than the beam size, but has an anisotropy, or preferential direction within the film in which the ions seems to migrate more easily, even though that regions is not being directly irradiated by the beam. We associate this phenomena to regions better connected with respect to the ionic transport, in the same sense of what was observed by Delport et al. [116] for the carrier transport properties.

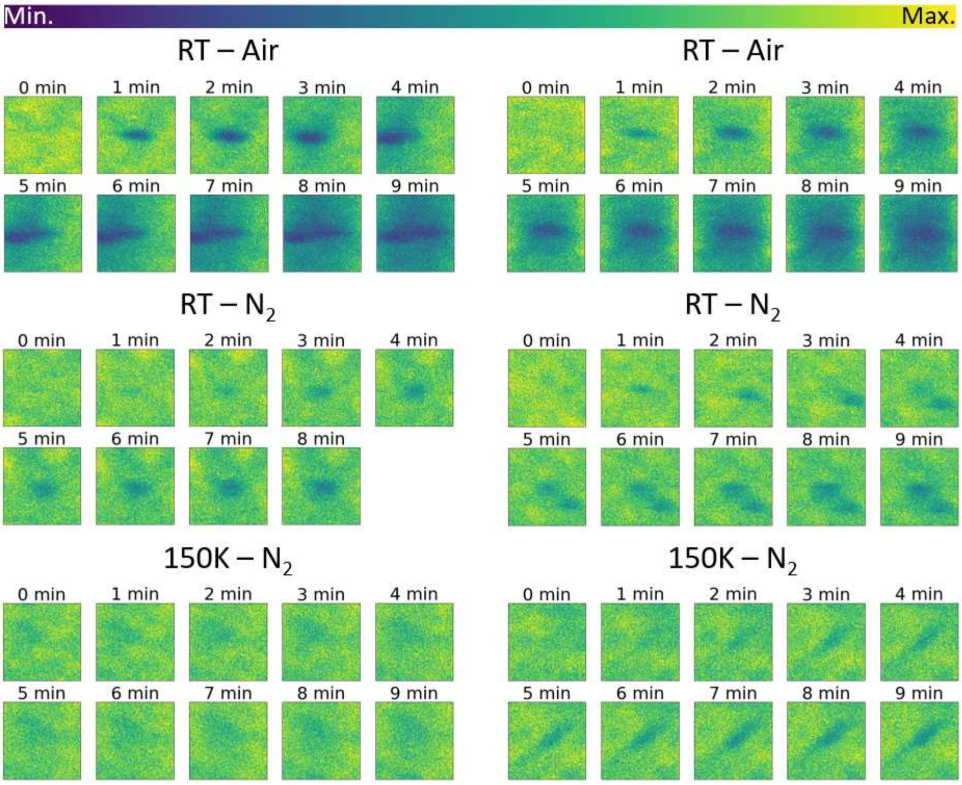

Figure 4.11: Effect of dose and atmosphere on damage. The deposited dose in the sample increase at the rate of 70 GGy per minute being deposited at the same point. Sequences show 10 × 10 μm^2 areas of the iodine fluorescence.

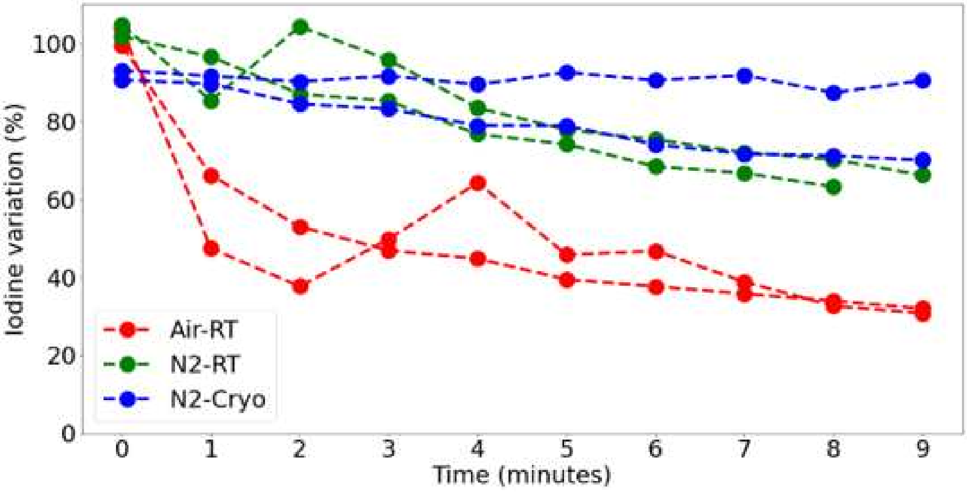

Figure 4.12: Variation in the iodine content. The iodine variation in a 10 × 10 μm^2 around the irradiated region is monitored with respect to the initial iodine content of a square in the tio left of the scanned region.

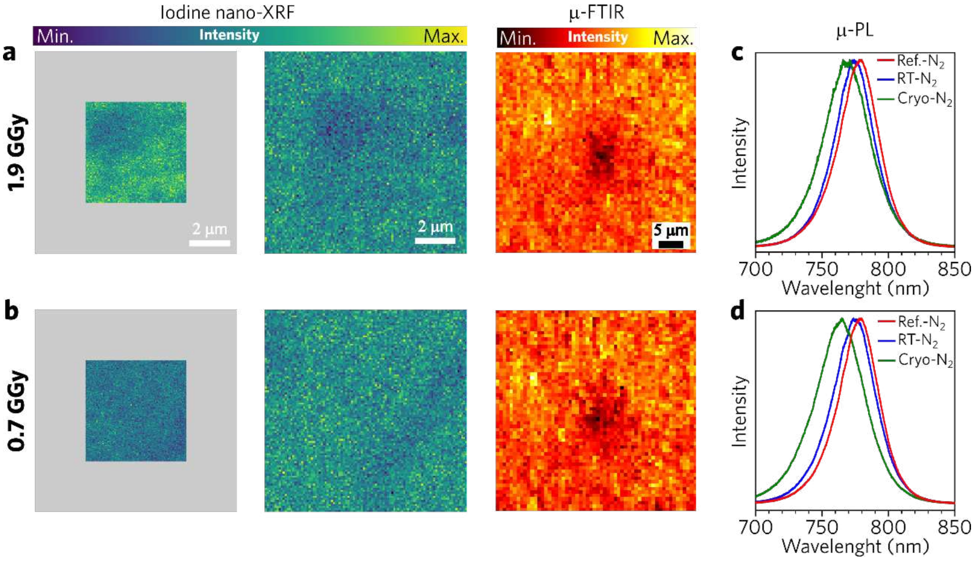

Figure 4.13: Perovskite damage with reduce dose and inert atmosphere. Sample irradiated with (a) 1.9 GGy and (b) 0.7 GGy in RT-N2. From left to right, nano-XRF damage scan, nano-XRF probe scan and μ-FTIR (1700 cm-1). (c and d) Respective μ-PL at RT-N2 and Cryo-N2.

4.4 Beam damage model proposal

Figure 4.13 displays the nano-XRF and µ-FTIR of the regions measured with the two smaller doses, 1.9 and 0.7 GGy, at RT-N_2. The reduction in absorbed dose, coupled with an inert atmosphere, effectively mitigates damage. The inorganic elemental distribution remains stable, although the organic component still experiences a reduction. AFM's topographic analysis (not shown) reveals no observable excavation. Interestingly, the photoluminescence properties are nearly unchanged under the RT-N_2 condition, with a slight blueshift in emission compared to the pristine sample (Figure 4.13c-d, μ-PL column). Additionally, the Cryo-N_2 condition is included to illustrate that the compound is more affected, particularly in terms of photonic properties, at cryogenic temperatures. A more significant shift and broadening in emission are observed, with the lowest dose surprisingly yielding the largest shift and broadening.

Our findings provide crucial insights into the damage caused by intensely focused X-ray beams on perovskite compounds. Figure 4.14 presents a schematic view of the damage induced by the X-ray beam in the MHP. The X-ray absorption cross-section of light elements, such as carbon and nitrogen from the organic part of the perovskite, is very weak, rendering the organic molecules essentially transparent to the X-ray beam. In contrast, the inorganic cage of heavy atoms absorbs X-ray photons more efficiently, decaying through different pathways, including the emission of electrons that interact more effectively with the organic molecules, ultimately creating ions or radicals. Both ions and radicals are reactive and can be neutralized or undergo reactions with other species. [117] [118] Various reactions can be proposed between ions and radicals with defects in the perovskite compound. These reactions generate new species that can be trapped in the structure or released as a gas, such as $PbBr_2$ crystallite or I_2 molecules. This process results in the creation of new punctual defects in the compound, eventually modifying their properties. However, if several defects are formed near each other, the 3D perovskite cage may be destroyed. Therefore, a small or intermediate dose could produce a defective material compared to a severely damaged one by a high dose.

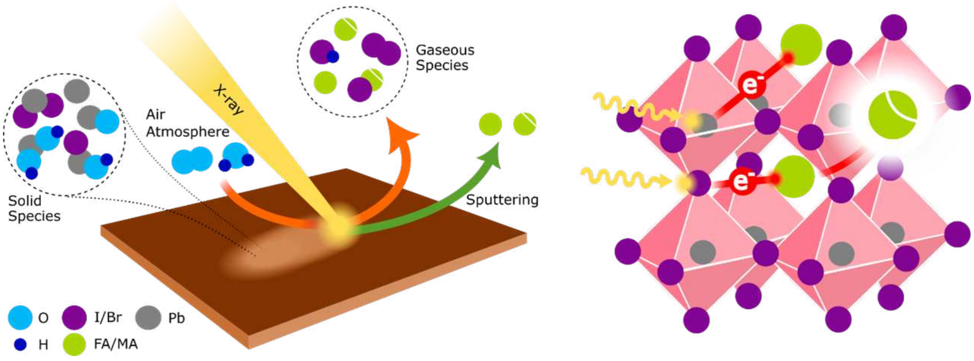

Figure 4.14: Schematic representation of the X-ray beam damage on the MHP.

The conservation of energy and momentum dictates that the electron must transfer energy to an atom when they interact in elastic scattering. If the transferred energy exceeds the displacement energy (Ed), the atom moves to an interstitial position, creating a defect. The Ed depends on the atom's bond strength, crystal lattice, and atomic weight. [118] As the perovskite is composed of medium to heavy elements, an intense displacement in the bulk is not expected. However, if an atom is at the surface, the Ed is lower, and the atom can leave the specimen in a sputtering-like process. [118] One expects a high sputtering contribution from the organic molecules, independently of the atmosphere and temperature. However, those from the inorganic elements (Pb, I, and Br) should be smaller unless they have high mobility and are more reactive, as is the case of the iodine ions exposed to the air atmosphere.

Hence, the MHP damage mechanism combines radiolysis and sputtering. The radiolysis produces reactive species that react with other elements leading to the formation of volatile species that leave the sample. In the air, the O_2 and H_2O molecules can react with perovskite in different ways forming solid species such as PbO, $Pb(OH)_2$, $PbCO_3$, PbIOH, Pb, PbI_2, and $PbBr_2$. [119] [120] [95] Orri et al. [95] reported forming the $PbBr_2$ crystalline phase as a product after electron or X-ray irradiation. Also, volatile species such as I_2, HI, and deprotonated or degraded FA/MA molecules (CH_3I, NH_3, HCN, $C_3H_3N_3$) can form and leave the sample. [121] [122] [123] The iodine departure is corroborated by the absence of iodine accumulation at the boundaries of the $5 \times 5\ \mu m^2$ irradiated area. These reactions probably occur more on the surface where the sputtering is more intense, and volatile molecules face a short path to escape. The N_2 atmosphere inhibits the O_2 and H_2O degradation paths. Consequently, the degradation is less severe, and inhibiting the formation of the iodine volatile species limits the iodine yanking out. However, the organic molecules still suffer from radiolysis and sputtering. Further investigation of the loss of the halogen can possibly provide the exact route for the volatilization process, such as the degradation over continuous x-ray irradiation under a toluene bath, which would quantifies the amount of iodine being extracted from the sample, however such an investigation is out of the scope of this work.

4.5 Practical application of the methodology developed

To highlight the relevance of controlling the X-ray dose and environmental conditions when applying X-ray nanoscopy for perovskite investigation, it is reported an X-ray ptychography study in an MHP compound. X-ray ptychography [108] is a phase contrast technique that reveals morphological aspects not seen in traditional scanning X-ray microscopy in transmission (STXM) or fluorescence (SXFM) modes. As a phase contrast technique, it is more sensitive to low-Z elements than absorption contrast techniques. A $Cs_{0.05}FA_{0.95}PbI_3$ perovskite film was prepared and intentionally irradiated , depositing a severe dose of 350 GGy on a single spot of 500 × 200 nm^2, corresponding to about 3.1 $\times 10^{23}$ 10-keV-photons/m2. After irradiation, a ptychography was performed map on a 10 × 10 μm^2 surface with steps of 100 nm, depositing a smaller dose of 0.0015 GGy, reaching a final reconstruction with a final global resolution estimated by FRC method [89] of 17.4 nm. The observation of Figure 4.15.c indicates that hole formed in the sample is not even visible in the STXM map, as like none of the grain details. In fact, no details can be observed in the transmissions because even the variation caused by the removal of matter by the x-ray beam is not detectable, while it is clearly distinguishable in the ptycography. It occurs because a 400 nm thick perovksite film has an absorption lesser than 2% for 10 keV photons. So, even if 50% of the perovskite film was expelled by the beam, the maximum variation in STXM measurements from the irradiated region to a undamaged region would be less than 1% of the beam intensity.

4.6 Conclusions

A correlative multi-technique approach was effectively applied to investigate the damage caused by highly intense focused X-ray beams on hybrid organic-inorganic metal halide perovskites. Using focused X-ray beams for perovskite characterization will be challenging as the absorbed dose determines the damage, and each technique requires different doses to produce enough signal-to-noise ratio to extract information. Then, evaluating how the beam damage affects the desired properties is highly recommended before any material investigation. The results show that combining an inert atmosphere with a controlled dose is compulsory to mitigate beam damage and provide conditions to understand the photo-structural-chemical dynamics of MHPs. Contrary to the expected common sense, cryogenic conditions are not the best for performing X-ray measurements under high doses because they lead to reduced mobility and cause morphological changes. Moreover, thoroughly re-

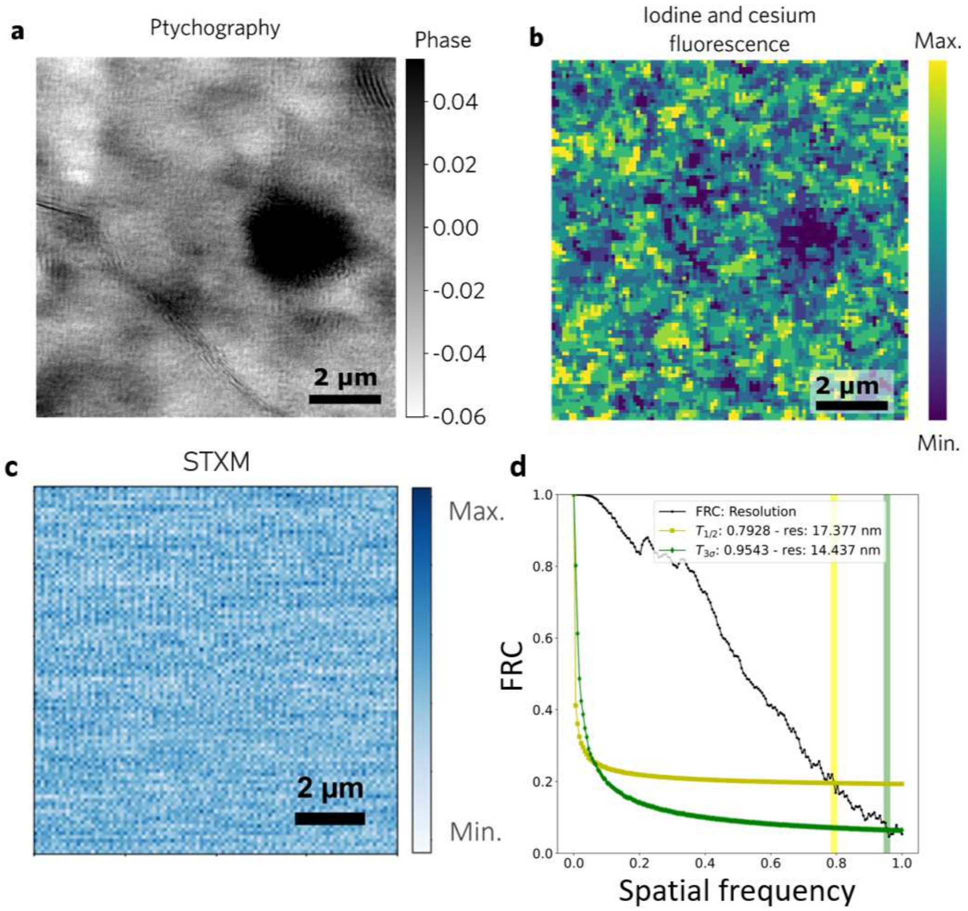

Figure 4.15: Simultaneous X-ray ptychography and fluorescence images of a perovskite. (a) Ptychography, (b) iodine and cesium nano-XRF images of $Cs_{0.05}FA_{0.95}PbI_3$ perovskite compoundx (c) STXM map from the same data as ptychography and (d) FRC of (b), showing a final resolution of 17.4 nm according to the 1/2-bit criteria (see Appendix I).

porting the X-ray deposited power on samples, i.e., the absorbed dose in Gy, will help the community find the best experimental conditions to work safely. As a clear demonstration of how powerful the use of sophisticated new techniques in synchrotron radiation facilities can be, the optimized conditions was applied below the harmful dose to demonstrate the feasibility of investigating MHPs with the X-ray ptychography technique, uncovering morphological details never seen before.

The optimal conditions to continue the studies are, explicitly said, the ones presented in Figure 4.13.a with 1.19 GGy under RT-N_2 atmosphere. All the data from experiments performed at Carnaúba present in this work from now on (Chapter 5) will be performed in this condition, or with less dose deposited per acquisition.

CHAPTER 5

MULTI-SPECTRAL SYNCHROTRON EXPERIMENTS IN METAL HALIDE PEROVSKITES

Several aspects of morphology, chemical composition, and optoelectronic properties are to be uncovered from the micro to the nanoscale in metal halide perovskites (MPH). [14] [2] [1] [124] X-ray nanoscopy techniques available at the CARNAUBA beamline (SIRIUS/LNLS) are up-and-coming to investigate MHP, revealing the correlation among morphology (x-ray ptychography), stoichiometric chemical distribution (X-ray fluorescence - XRF), and optoelectronic response (X-ray excited optical luminescence - XEOL) of these materials. Here, it is reported X-ray nanoscopy experiments, including coherent diffractive imaging (CDI) in flyscan mode on $Cs_xFA_{1-x}PbBr_{0.38}I_{0.62}$ thin films over mylar substrate. Ptychography in phase contrast (14 nm pixel size @10 keV) reveals morphological aspects not visible in traditional scanning transmission microscopy. XRF maps correlate wrinkled morphology to variations in Br:Pb stoichiometry, which agrees with shifts in emission seen by the XEOL. The possibility of measuring in fly-scan mode and N_2 atmosphere was essential to mitigate damages, typically the main limiting factor to applying the CDI in such samples. Our multispectral images of MHP are a pivotal step in developing and applying the technique in beam-sensitive samples for high-resolution imaging, especially in the case of heterogeneous and hierarchical functional materials in which the multiscale properties determine final device performances.

5.1 Sample preparation

We deposited the perovskite $Cs_xFA_{1-x}Pb(Br_{0.38}I_{0.62})_3$ (x = 0.10,0.20,0.30,0.40), from now on called X:38, using the traditional antisolvent method onto 6 μm mylar substrates, as described in Section 4.1. All the samples were prepared at the LNES-IQ/UNICAMP by collaborators. This simple and innovative substrate is well-suited for this study because it allows X-ray and other correlative characterization techniques, serving as a cheap and viable option to the area-limited and considerably expensive SiN windows commonly applied for X-ray transmission techniques such as STXM and ptychography. This study was conducted at the CARNAÚBA X-ray Nanoprobe beamline of the LNLS/CNPEM. [3]

5.2 Beamline experiments

The SIRIUS storage ring was running at 3 GeV and 100 mA, [125] with the beamline delivering a nanobeam of 200 nm(V)x500 nm(H) and a photon flux of $5x10^9$ ph/s at 10 keV. The methodology to correlate the information on morphology, chemical and optoelectronic response heterogeneities consisted of simultaneously and/or correlatively measuring the sample with the techniques available at Carnaúba beamline: x-ray ptychography [108], x-ray fluorescence (XRF) [126] an x-ray excited optical luminescence (XEOL) [79]. The main text will present the results for all four compositions and main compositional trends will be graphically presented and discussed.

5.2.1 Fluorescence - XRF

Figure 5.1a-d shows a 50×50 μ m^2 nano-XRF maps of the four heaviest elements on the sample acquired at room temperature and in an air atmosphere (RT-Air) in all four compositions. To irradiate and map the sample, we used the fly-scan snake mode with the scan starting on the left-bottom corner of the image and the beam spot going up and down while sliding to the right related to the sample. For optimizing the contrast two scans were performed with different excitation energies: 10 keV, for mapping the I-Lγ_1 (3938 eV) and Cs-Lβ(42YZ eV), and 14 keV, for mapping Pb-Lα_1(10551 eV) and Br-Kα_1(11924 eV). The X-ray dose after irradiation corresponds to about 7.63×10^6 Gy deposited in the scanned region, where 1 Gy = 1 J/kg is a measure of the total energy deposited per quantity of material irradiated. [126] These maps are damage free in the sense that, in the previous Chapter, we have shown that this absorbed dose is sufficiently low to not affect the chemical or morphological distribution, as well the optoelectronic response of the sample in the irradiated region and near surroundings. [16] [96] [2] All dose values presented here are calculated via Python code available at Appendix G.

The main heterogeneity present in the sample in the tens to hundreds of micrometers range are the well-described and characteristic of these Cs-rich compositions wrinkled morphology [127] [54] as the increase in the topography height. The corrugations in the sample are the result of the strain relief during step annealing of the film [23] and reach up to a few micrometers height, with widths coming from 3 μm, in 10:38 and 40:48, up to approximately 10 μm, in 20:38. Further details in morphology will be discussed later in the text. The width and height of the wrinkles change according to the composition. The topography has a huge impact on the total amount of the elements, once one can see that all 4 heavy elements have a similar distribution following the main total mass distribution, as shown in Figure 5.1. Despite this being a trivial observation, it is important to highlight that the figure shows that the micrometer to millimeter range main properties and heterogeneities are preserved in the new substrate. Furthermore, these pronounced heterogeneities are not directly linked to stoichiometric variations in the sample. These large-area scans do not provide enough photon counting in order to study more subtle variations in the proportions of the elements in the sense that the ratio between the bromine and lead fluorescence signals, Br:Pb, is the same overall within the noise of the measurement. In other words, they do not have sensitivity to track the variations in the stoichiometry of the material.

To observe stoichiometric variations smaller scans with higher acquisition time in smaller areas around the wrinkles were performed (Figure 5.2).

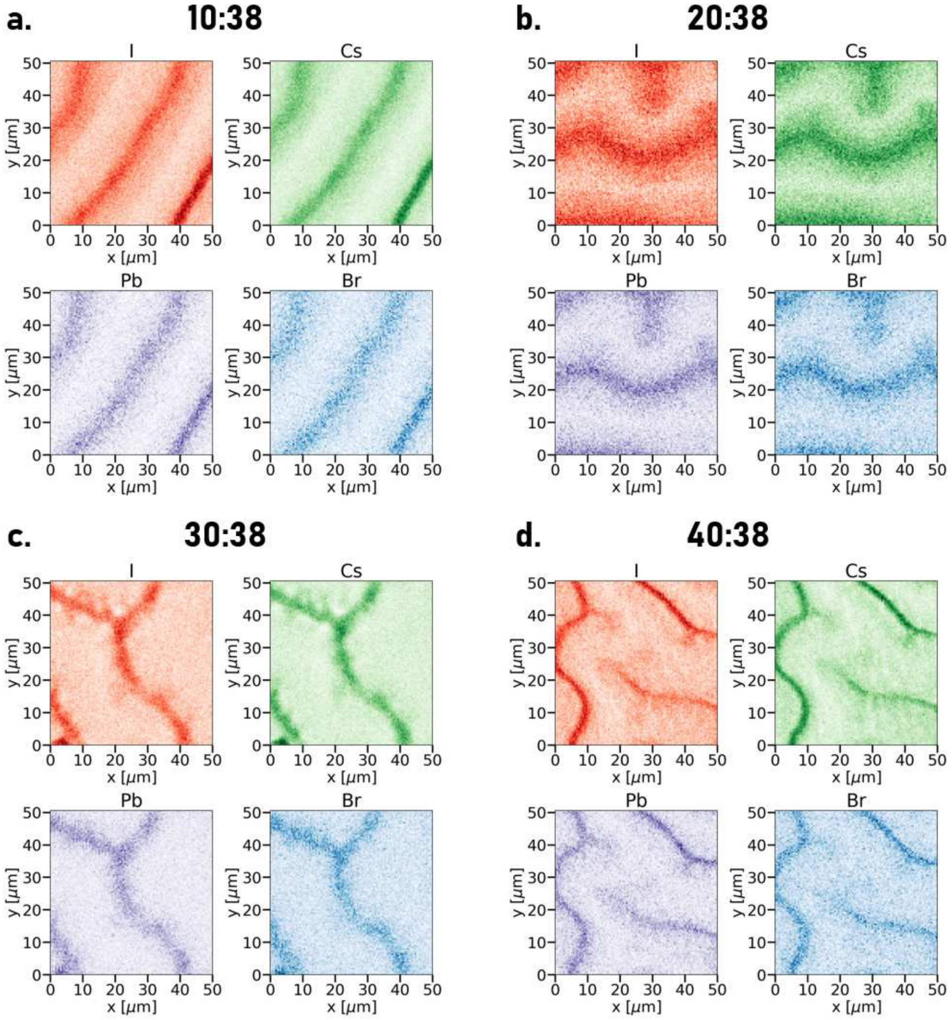

Figure 5.1: X-ray fluorescence maps for samples (a) 10:38, (b) 20:38, (c) 30:38, (d) 40:38. Colormaps goes from minimum to as maximum as it goes from white to the dominant color representing each element: red - I, green - Cs, purple - Pb, blue - Br.

The analysis between the fluorescence signals ratios, especially the Br/Pb ratio, indicates a variation in the stoichiometry highly correlated to the ~5 μm morphology features when analyzing a smaller region as shown in Figure 5.2. In these 5×5 μm^2 scans (30 ms integration per point) , one can observe that there is a gradient in the Br/Pb ratio that is anticorrelated to the morphology gradient representative of the wrinkles. More specifically from the valley regions of the morphology to the hill regions, one can observe a decrease in the Br content with respect to the Pb when compared to the valley regions. This variation in the Br stoichiometry with respect to the Pb, which is expected to be less sensitive to segregation due to its lesser mobility, [128] prevails over all the samples. A sudden variation happens however at the 20:38, in which the wrinkles become larger (~10 μm), and yet less pronounced resulting in a more homogeneous distribution of matter. Simultaneously the variation in the Br:Pb ratio is less prominent in this composition. For the Br:Pb ratio maps presented in Figure 5.2 a binning in the image by a factor of 4 was applied in order to reach enough statistics for the analysis. That is why the maps are presented with different pixel sizes.

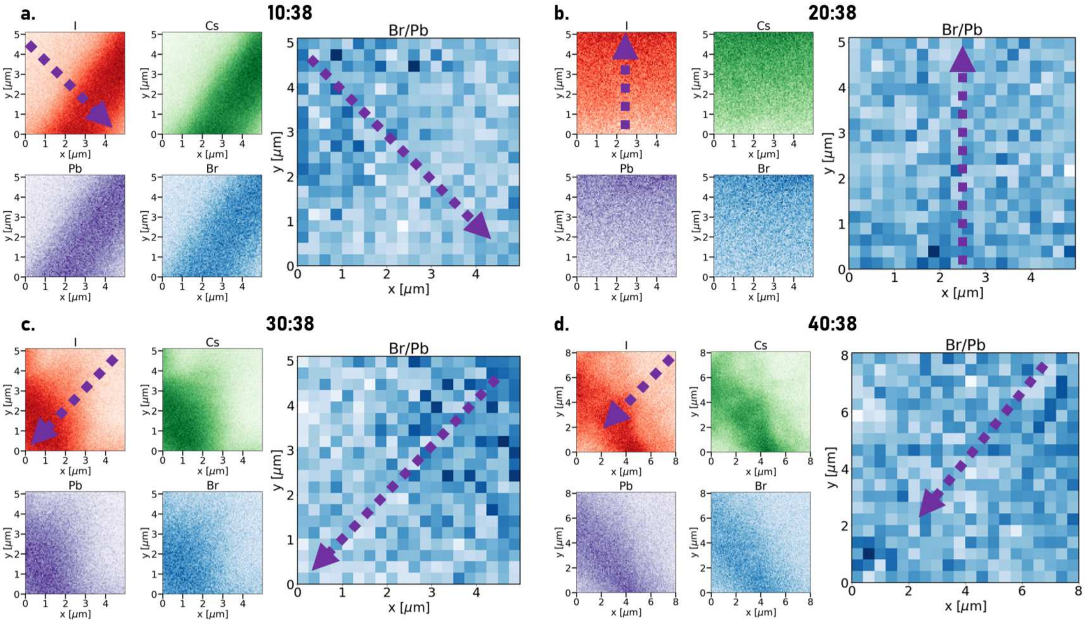

Figure 5.2: Stoichiometric analysis. X-ray fluorescence maps for samples (a) 10:38, (b) 20:38, (c) 30:38, (d) 40:38 in smaller plots. Large plots are the Br:Pb plots calculated from Br and Pb maps on left for each composition. Violet arrows indicate the direction of the morphology gradient. In the ratio maps the arrow show the decrease in the relative amount of Br with respect to Pb as it crosses the corrugation.

5.2.2 X-ray excited optical luminescence - XEOL

Associated to the variation in the stoichiometry, it is expected a variation in the optoelectronic response of the sample. [21] More specifically, the regions with more Br content most probably have a larger bandgap, and consequently a blueshift in its luminescence emission. To track that, XEOL experiments were conducted in the samples. As we scanned the sample, crossing the wrinkles, we observed that the luminescence signal varied in intensity and energy position strongly correlated to the morphology. Figure 5.3 shows the two lines representing the 10 keV beam path during the step-scan trajectory over the samples. At every 20 s (L1) or 60 s (L2) the beam that was continuously irradiating the sample was moved 3 μm to the next spot remaining while acquiring one spectrum every 1 s. One first observation is that the total intensity in the luminescence increases as the beam crosses the wrinkle, which is expected since there is an increase in the total amount of material, resulting in a more intense signal. In additon, the XEOL signal has a significant redshift from 1.75 eV to 1.66 eV as the X-ray beam crosses the wrinkles, which agrees with the Br:Pb ratio maps variation. This redshift behavior is consistent and present in all X:38 compositions, with only a global blueshift following the increase in Cs-content in the mean stoichiometry. The mean emission positions are present at 1.62 eV, 1.675 eV, 1.69 eV, and 1.735 eV for the 10:38, 20:38, 30:38 and 40:38, respectively (Figure 5.4).

Very interestingly, studying each point of irradiation separately, the total luminescence signal decreases with time of irradiation, followed by a decrease in the total amount of iodine seen by XRF. This is a consequence of a beam damage caused by the high dose deposited on the sample with the 200x500 nm² nanobeam irradiating the same position, which purges the material. Besides the removal of the iodine (and other parts such as the organic cation, as observed in Chapter 4), the remaining perovskite keeps the emission position almost unchanged. The same process is observed in Chapter 4. This behavior is common to all the samples in the series. One interesting trend, however, is the fact that the decay time of both iodine content and XEOL signals is reduced with the decrease in the total Cs of the composition. This observation reinforces the fact that increases in Cs content imply a better resilience of the sample, in this context for the XEOL with respect to X-ray beam irradiation.

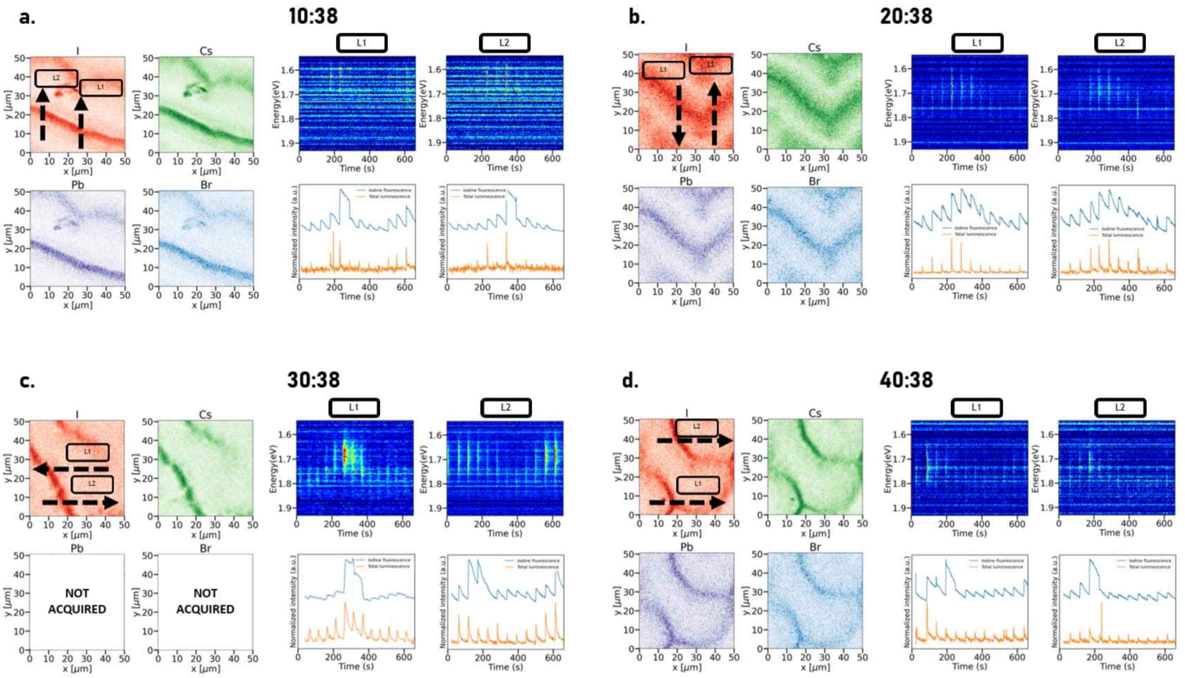

Figure 5.3: X-ray excited optical luminescence. Fluorescence maps for samples (a) 10:38, (b) 20:38, (c) 30:38, (d) 40:38 in smaller squares. Black arrow indicate the lines crossed over the sample as the XEOL is monitored at each second. 2D plots of XEOL spectras for each lines show the redshift as the probe crosses the wrinkle. The graphs show the total luminescence intensity (orange) and iodine content (blue) variations at the beam rests 60 s at each point of the line scan. The fluorescence maps in 14 keV for Pb and Br maps for the 30:38 samples were not acquired due to a malfunctioning of the beamline shutter.

For a more representative sampling of the optoelectronic response of the material, collections of XEOL spectra were acquired at every 1s with a deadtime of 0.1s between acquisitions as the beam fly-scanned a 50 × 50 μm² area during 172s with a speed of 50

μm/s. Figure 5.4 summarizes the spectra for each composition studied. This strategy is a smart way to avoid the issue with the damage suffered by the sample as observed in Figure 5.3, and even though it does not provide an image, it produces a response that is on average a good representative of the sample sensitive to spatial variations in some lengths. One can see that, for each composition, the peaks can be grouped in two main components: one at the lower energy position with a higher intensity, representative of the moments in which the x-ray beam is predominantly over the hill of the morphology, and other at a higher energy with lesser intensity, that is correlated to the valley regions. The clustering effect can also be visualized in Figure 5.4, where for each composition one can see that the points are dispersed in two groups, lesser in some cases such as in 40:38, and extremely pronounced for 30:38 for example. Also, the behavior of the bandgap increases with the Cs content in the sample.

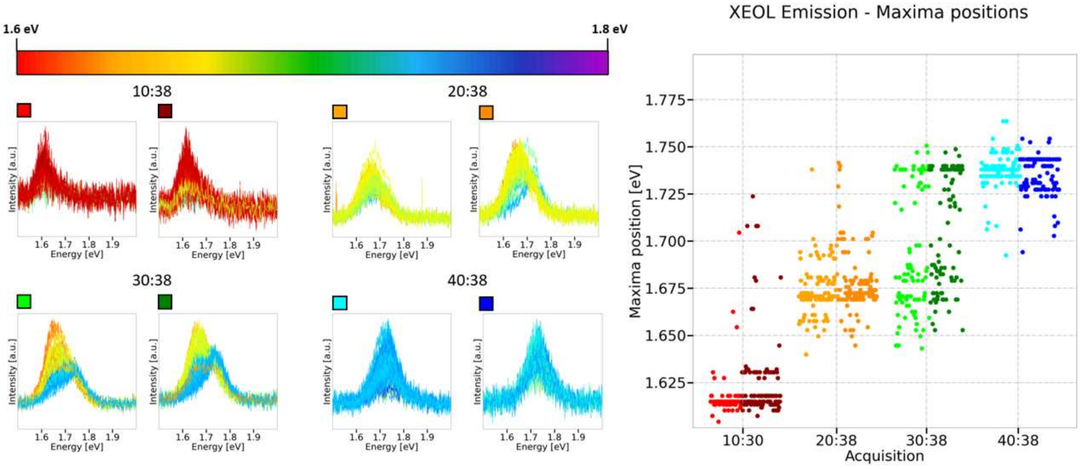

Figure 5.4: XEOL spectra acquired during fly-scan. Each spectrum is acquired during a 1s integration time, while the beam is fly-scanning the sample. The color of the line for the plot is chosen according to the position of its maxima. Color code is shown in the bar over the spectra. The position of the maxima is scattered for each sample in the plot on the right. Points in red are with respect to sample 10:38, orange 20:38, green, 30:38 and blue 40:38.

Despite the relevant information that these two methods of acquisition bring, they still lack important information and/or reliabilities in some aspects. The line scans crossing the wrinkles continuously irradiate the sample, which damages the sample in the sense that even though the energy of the emissions shows no changes, the total intensity decreases, so possibly the initial spectra are not pristine, since it has some effect of the previous moments in which the beam crosses the sample to reach the next point in the scan. The flyscan deposits a very low dose in the sample minimizing possible damages, however, it does not provide spatial resolution. To solve these problems, a new approach to measure the sample was proposed to the setup.

Using the control infrastructure of the beamline, which enables the use of individual triggers between the elements of the optics, detection and beam control, a deterministic control architecture was implemented, based on the Trigger And Timer Unit (TATU), an in-house development for FPGA-based applications created on NI's CompactRIO (cRIO) TTL signals. TATU is configured via EPICS to receive and distribute triggers from/to controllers setting the detectors, shutters, and other components of the beamline. The architecture proposed is illustrated in Figure 5.5. A master trigger with size ΔT_{Total} is sent to all the components. The detectors are configured to acquire exactly after this signal for a given time ΔT_{Sum} slightly smaller than ΔT_{Total}, to avoid conflicts such dead times of the detectors, while the shutter is configured to open just after a delay δt and keep open for an interval $\Delta T_{Irradiation}$ and than close again before the end of the ΔT_{Sum} period by δt. The experimental values used for the time constants were:

$$\Delta T_{Total} = 1s$$

$$\Delta T_{Sum} = 0.9s$$

$$\Delta T_{Irradiation} = 0.7s$$

$$\delta = 1s$$

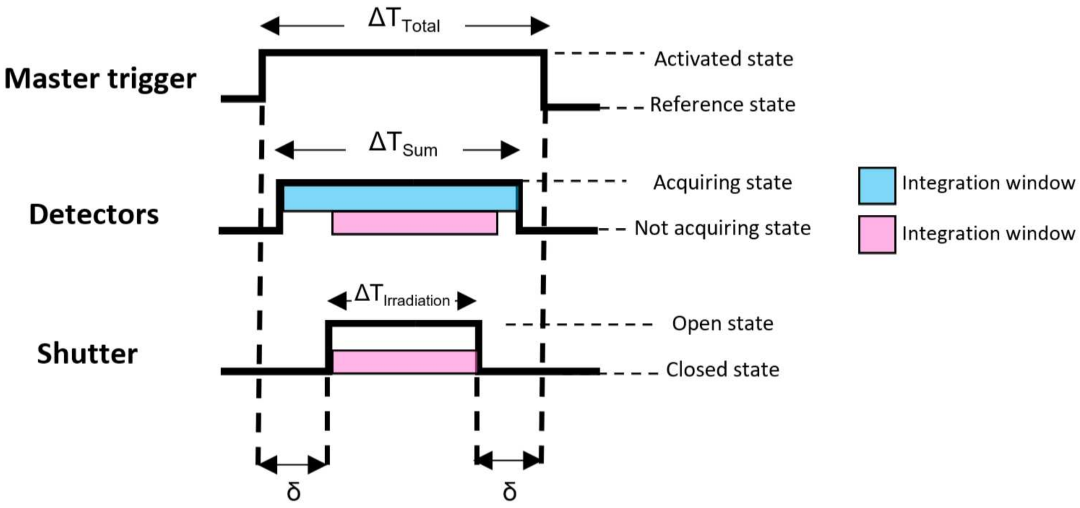

Figure 5.5: Trigger architecture for XEOL maps.

This time structure is repeated at each step as the beam moves through the sample, and summed up to the fact that each point of acquisition is separated by 3 μm in the maps that we performed, we guarantee that at every single position, the original undamaged signal from the sample is acquired, since the region is only irradiated after the acquisition is initiated and the N_2 atmosphere guarantees that for irradiation of 0.7 s not observable damage were caused by the adjacent points, as showed in the previous chapter (Figure 4.11).

The maps resulting from this step-scan acquisition method are shown in Figure 5.6. The fly-scan measurement of the I-L3 fluorescence performed in the same position with better resolution (500 nm) is presented on top of each sample with a contour line at the threshold value of 50% of the maximum of the counting. The same contour is plotted over the resulting luminescence maps from the new approach. The first initial observation is that, as one could expect the regions of the morphology with the largest amount of matter show a brighter luminescence signal, since a higher amount of matter generates a higher luminescence signal. The other predominant feature that confirms the observed previously by the line scan is the redshift of the emission from the valley to the hill regions, which is a direct consequence of the stoichiometric variations observed in the Br:Pb ratio maps from Figure 5.2. The variation within the map of each sample portrays the dispersion illustrated in Figure5.4, with a tendency of lower energy emissions as lesser Cs in the composition. The particularly broad dispersion in the emission that was firstly observed for sample 30:38 in Figure 5.4 is again observed in its map, with a larger contrast in the emission from the hill to the valley regions when compared to the other samples.

Further investigation of the spatial variations in luminescence response and the correlation with the wrinkle morphology using the Multivariate Curve Resolution with Alternating Least Squares (MCR-ALS) and Principal Component Analysis (PCA) approach is presented in Appendix J.

5.2.3 Nanodiffraction

Nanodiffraction experiments were conducted in order to correlate the lattice parameter size with the stoichiometric variations in the samples. The polycrystalline nature of the sample, with crystallites smaller than 100 nm in average, makes it impossible to measure the single-grain strain field in these samples since Tarumã's beam is larger than that. However, the average lattice parameter in the micrometer size range is possible to achieve. As the film is a powder, with no texture or preferential orientation, as the beam crosses the sample, eventually some crystallites will be in diffraction condition, and some of the fraction of the powder ring that eventually hits the detector will be acquired. The model for the nanodiffraction analysis is described in Appendix F.

Simultaneously to the XEOL maps (excitation at 7 keV), nanodiffraction of the samples was acquired at the peak of the (100) family of the cubic perovskite structure with detector positioned at fixed position covering the 2θ range from 13.6° to 18.2° (q = 0.85 Å^{-1} - 1.12 Å^{-1}) at the distance of 1.1 m from the sample, with pixel size angular resolution of 0.003°. The section of the powder ring selected by the detector corresponds to ~16° (4.5% of the total 360° of the reflection). As the beam scanned the sample, a few grains were at good orientation for diffracting into the detector, creating a collection of diffraction peaks, which are shown in Appendix H. Integrating the total intensity of each diffracting speckle one can obtain the diffracted intensity maps in Figure 5.7. The intensity maps in this case are only guidelines of the diffracting positions for the eyes since one cannot guarantee that

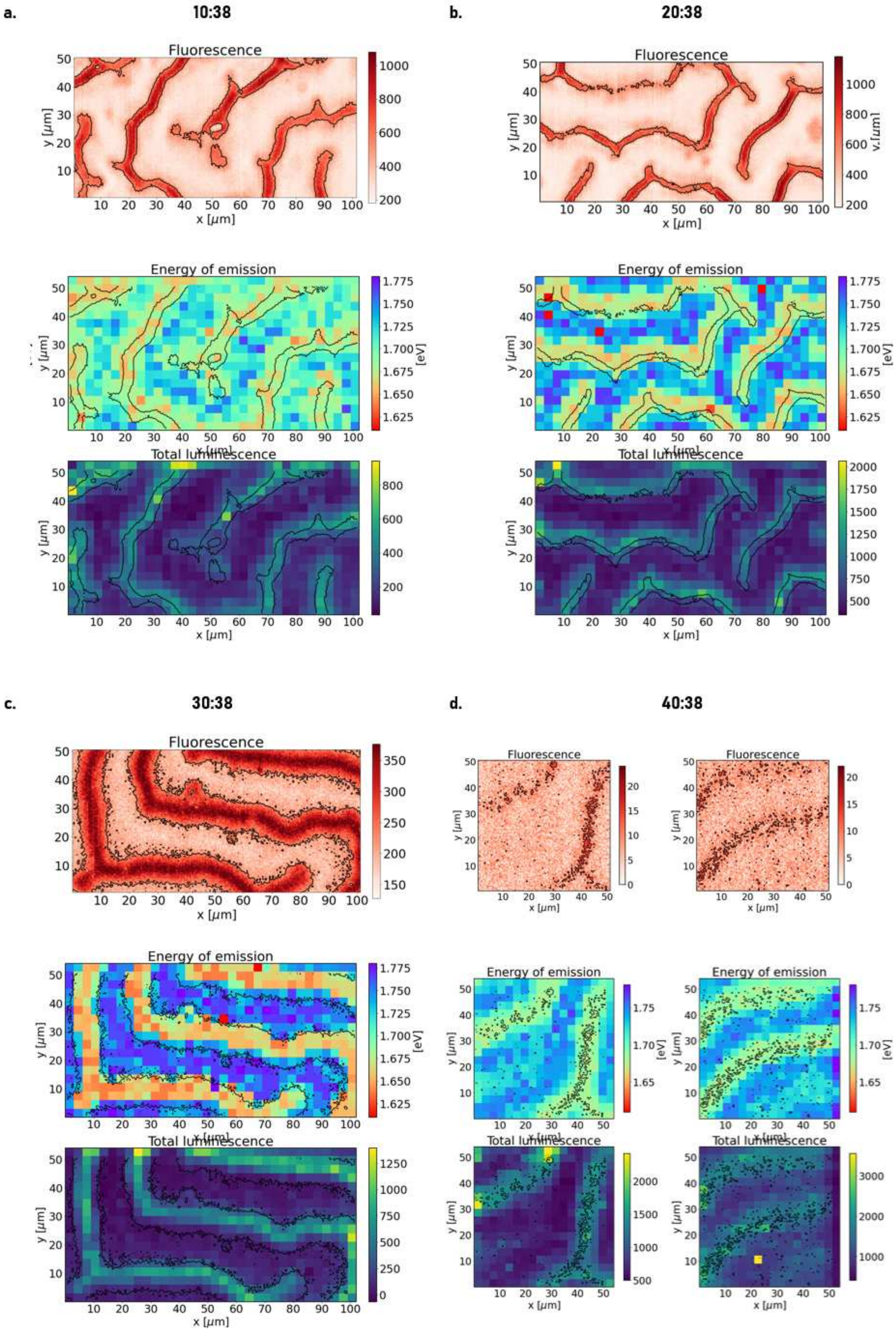

Figure 5.6: XEOL maps. From top to bottle the I fluorescence, the position of the maxima of the emission (Energy of emission) and the total luminescence intensity are presented from samples (a) 10:38, (b) 20:38, (c) 30:38, (d) 40:38. Black line are the 50% of the maximum fluorescence in the area contour lines.

each of these peaks are at the maximum of its rocking curve, and therefore no information of crystallinity for example can be discussed. Figure 5.7 also presents the fluorescence maps with the 50% threshold contour lines in black, which are reproduced in the Diffracted intensity maps and the lattice parameters maps segmenting the total area studied in two regions hill (gray), where the fluorescence is higher than 50% of the maximum intensity, and valley (white), where the fluorescence is lower than 50% of the maximum intensity. Consistently the majority of diffracting points are over or close to the hill regions, which can be explained by the higher amount of matter in these regions, which increases the probability of a diffraction to occur.

Determining the center of mass of each speckle is possible to calculate the local lattice parameter of the sample, which is shown in Figure 5.7. The average lattice parameter for samples 10:38, 20:38, 30:38, and 40:38 are calculated as 6.27 Å, 6.26 Å, 6.24 Å, and 6.26 Å, with standard deviations of 0.04 Å, 0.03 Å, 0.03 Å, and 0.03 Å, respectively. This sequence shows a small tendency for decrease in the lattice parameter with the increase of the Cs content that is not respected by 40:38. The decrease in the lattice parameter is expected due to the smaller radius size of the Cs^+ cation compared to the FA^+, and it was already observed in previous studies [127] [16] and by non-synchrotron diffraction data discussion to presented Section A.1. The reason for the 40:38 not respecting the tendency is the fact that only a small number of points are diffracting in each map, which makes the statistics to determine a true mean value unsurprisingly low. The standard deviations of each map do not even allow to separate the smallest to the largest average value obtained. Despite that, the nanodiffraction was capable of tracking spatial variations in the lattice parameter with 0.001 Å resolution in real space. The largest variation in lattice parameter was found in 10:38 of 0.187 Å, while 40:38 has the smallest difference between the two most distant lattice parameters measured, 0.113 Å.

In fact, for this sample, nanodiffraction may not be the best strategy to study the correlation between morphology and d-space variations. Microdiffraction with a slightly larger beam, for example, would provide better statistics, and the detector positioned with access to a larger portion of the reciprocal space would improve the amount of data available, even though it would cost spatial resolution in the scanning and reciprocal space resolution in the detector. No conclusive information could be taken from this dataset.

5.2.4 Ptychography - Ptycho

Despite this stoichiometric variation in the sample, strongly correlated to the micro-scale morphology, with direct implications in the optoelectronic response of the material, we observe that the wrinkle morphology does not imply in significant changes in the grain morphology. The area of 10x10 μm^2 was scanned with a step of 100 nm, >50% overlap in the probe size (500 × 200) H×V nm^2, including random variations in the 10100 probe positions

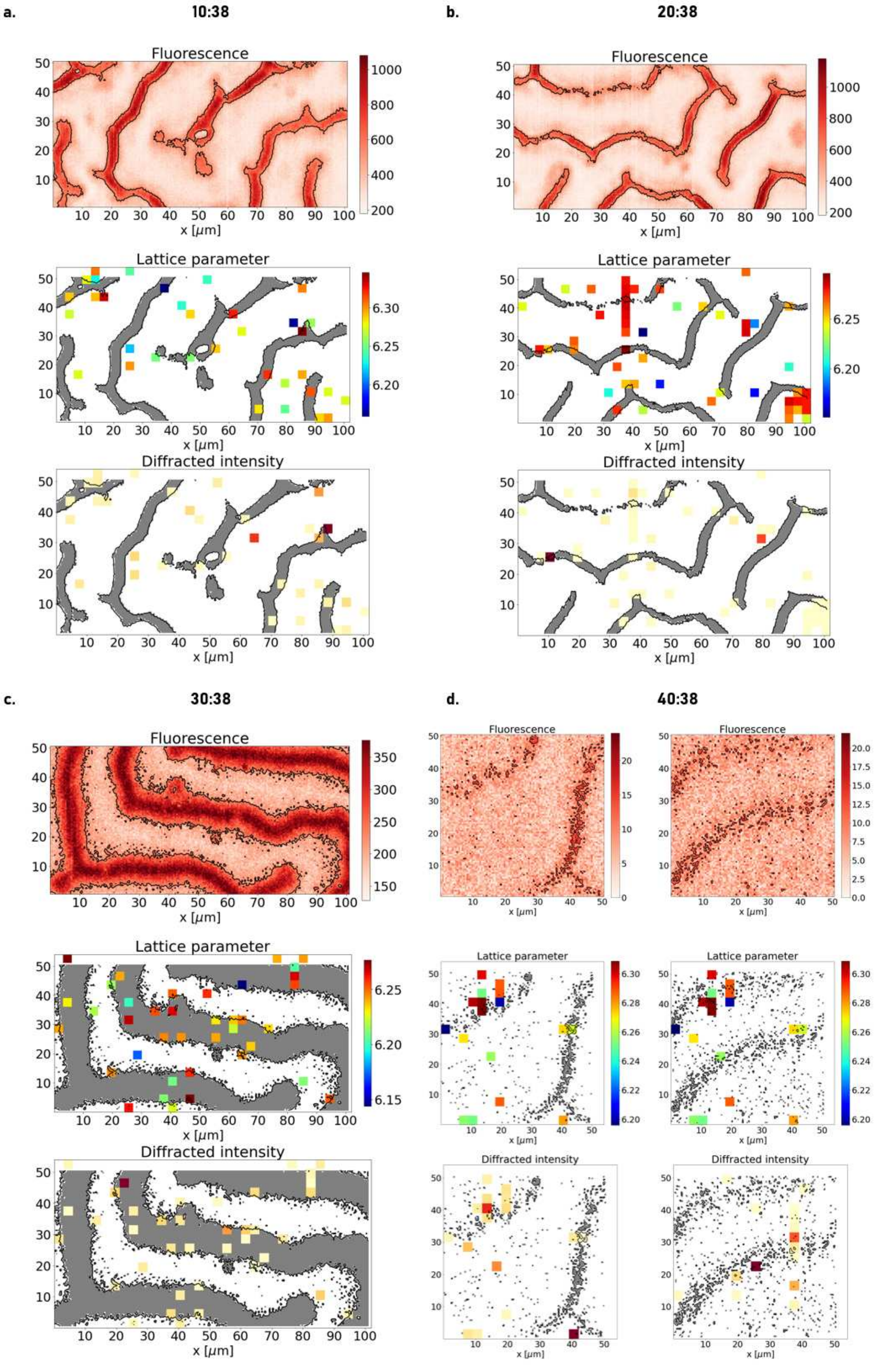

Figure 5.7: Nano-XRD maps. From top to bottle the I fluorescence, the lattice parameter and diffracted intensity are presented for samples (a) 10:38, (b) 20:38, (c) 30:38, (d) 40:38. Black line are the 50% of the maximum fluorescence in the area contour lines. Black lines segments the total area studied in two regions hill (gray), where the fluorescence is higher than 50% of the maximum intensity, and valley (white), where the fluorescence is lower than 50% of the maximum intensity.

with respect to a perfect square grid to avoid raster artifacts in the reconstruction. [82] The scan was performed at the energy of 10 keV in fly-scan mode with a constant velocity of 10 µm/s with a total acquisition time of 172s. The total dose of this scan was estimated to be 0.0015 GGy.

For the reconstruction, 256 × 256 pixels (55×55 µm²) of the data PiMega area detector at the distance of 1.1 m from the sample were used, resulting in a pixel size of reconstruction of 10 nm. The object was initialized with random amplitude and phase maps. The probe was initialized with the inverse Fourier transform of the average of the diffraction patterns in the first mode. Six more modes were added as random fluctuations of the first mode, and their maximum intensities were normalized to 15% of the first mode. The reconstruction was performed by combining 100 iterations of the Alternating projections (AP) [90] algorithm, followed by 5000 iterations of the Relaxed averaged alternating reflections (RAAR) [91] method, and finally, 1000 iterations of AP. The final R factor of the reconstruction reached the value of 6.1%, 4.9%, 6.3% and 5.1%, for Figures 5.8.a, .b, .c and .d respectively. [89] The same combination of reconstruction methods were used in all ptychographic reconstructed data in this chapter.

The ptychography measurements show the variations in the phase with the same sizes as in the morphology indicated by the higher amount of matter in the wrinkles morphology. In the phase map one can see the wrinkle morphology with a larger phase delay, in agreement with the larger amount of matter (Figure 5.8). Figures 5.8.b and .d also present phase shift in smaller dimensions, indicating a lesser electron density (less matter) in the contour of some nodular regions in the film's < 1 μm morphology. The large micrometer-size corrugations can be easily reconstructed. The reconstructions presented for samples 10:38, 20:38 and 30:38 correspond to areas covering the top of the corrugations, while Figure 5.8.d correlates with a region between two relatively close wrinkles. Figures 5.8.a, .b and .c have total phase shifts on the same order, which corresponds to very similar variations in the electronic density. This 0.9 delay in the 10 keV phase is a very representative number to the wrinkles in these materials, being present in most of the wrinkle reconstruction at this energy, and a strong indication that the variation in the total amount of matter in these compositions do not change drastically with the increase of Cs in these materials. In this case, the width of the wrinkles in 30:38 samples is considerably larger, 4 μm large, compared to the other compositions that are less than 3 μm in size. These observations match better the tendency observed in the samples studied in the nanodiffraction experiments.

A more detailed inspection of the reconstructions can improve the visualization of details. Focusing now on Figure 5.8.b, which is reproduced in Figure 5.9.a, the false color code saturated around the average phase value in one standard deviation of the phase distribution in the area (2σ of the phase histogram for the color bar range). This data selection improves the contrast of the more subtle details that were once hidden in the large phase shift of the wrinkled morphology. Oscillation in the phase shift shows fluctuations from 400

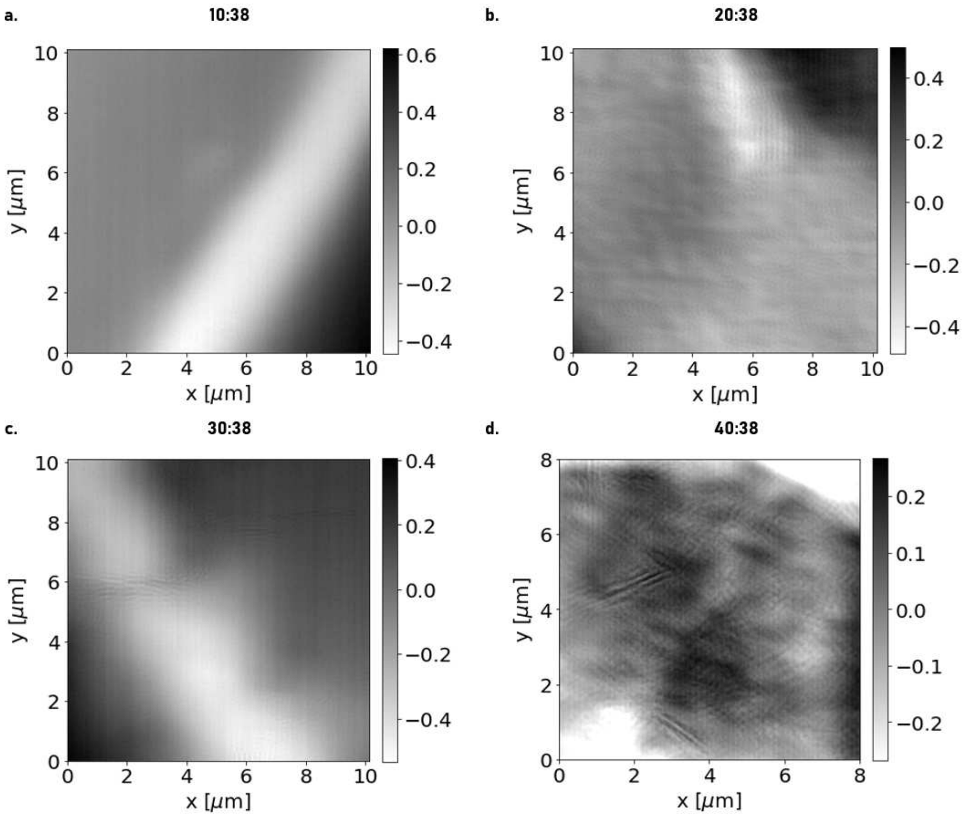

Figure 5.8: X-ray ptychography. Reconstructed phase for samples (a) 10:38, (b) 20:38, (c) 30:38, (d) 40:38.

nm up to 600 nm in size. These dimensions are considerably larger than expected for the grains in these compositions. But comparing these images with the SEM data to be presented in Section A.3 of the Appendix A, one can identify these images as clusters of grains organized in the wrinkles as fish scales- or flakes-like structures. These flakes would eventually coalesce as the annealing temperature gets higher, increasing the average grain size over the corrugation hill areas but not in the valley regions, as it is further discussed in Appendix A.3. To validate the structures, a second ptychography acquisition was performed, and the phase reconstruction is presented in Figure 5.9.b, where the same features in the electronic density distribution are observed.

Cropping the 10 × 10 μm^2 area into 4.6 × 5.6 μm^2 better optimize the color bar range for even finer details in Figures 5.9.c and d. The ~120 nm grains can be observed within the 600 nm structures. This grain distribution is uniform, and no change can be observed from hill to valley regions of the morphology. The same can be observed in Figure 5.8.d. However, the grain structures could not be observed in the 10:38 and 30:38 samples, even though their formation was confirmed by SEM images (Appendix A). In fact, despite the pivotal results in the micrometer size corrugation morphologies, and the visualization of the submicrometer size structures such as the flake-like grain clusters and single <200 nm grains in the 20:38 and 40:38 perovskites and pivotal reconstruction of the grain and damage region with 17.4 nm resolution shown in Figure 4.13, not all reconstructions are capable to reach a final result that allows for the visualization of the sub-micrometer structures, as in these scales the electron density is so small that even with the ptychography phase sensitivity convergence is still an issue.

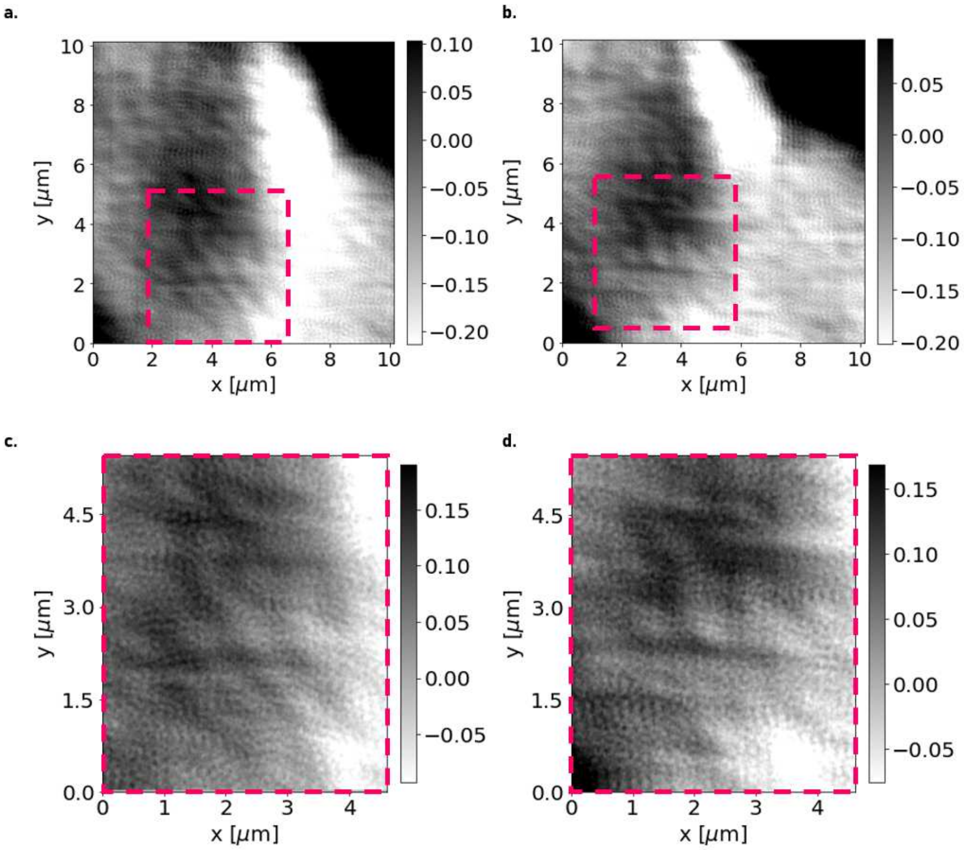

Figure 5.9: Grain morphology. Reconstructed phase for sample 20:38. (a) is Figure 5.8.b, saturated at 1 of the standard deviation of the phase distribution in the area. (b) is a second independent reconstruction of the same area from a different dataset. (c) and (d) are zooms in (a) and (b), respectively, in the areas indicated by the pink squares. The zooms highlight the grains with ~120 nm agglomerated in the region with an average size of 600 nm.

5.2.5 Incident photon energy influence in the reconstruction

As simple improvement in the resolution is not expected to guarantee a better contrast for this sample, and in fact only a gain from 17.4 nm to 11 nm, record of the beamline [3], was possible, other parameters should be taken into account to improve the reconstructions. To improve the ptychography phase contrast sensitivity in the reconstruction, the 40:38 sample was measured in two different energies, 6800 eV and 10000 eV.

The energy parameter was chosen since, from the fundamental properties of the X-ray interaction with the matter, the decrease in energy increases the cross-section with the materials (not considering the absorption edges) which is expected to increase the scattered signal, as shown in Figure 3.2. This strategy is commonly used in CDI experiments for soft biological matter, such as cells, which has low absorption contrast and low scattered signals. [129] [130] [131] Parameters such as the trajectory configuration or algorithms benchmarks could also be explored. However, energy is the most promising one, as no trajectory artifacts were found in the reconstruction shown before and it is a parameter that is expected to improve the phase contrast sensitivity. Moreover, no algorithm specifically developed for weakly scattering signal, such as Oversampling smoothness (OSS) [132] was available in the reconstruction package used in this work.

Figure 5.10 compares the phase and amplitude reconstructed at the energies of 6800 eV and 10000 eV. Comparing the phases in the Figures 5.10.a and .b where one can see the same features contained at a different phase interval, with small fluctuations in the phase of 6800 eV while at the energy of 10000 eV the phase is flattened, smooth, and surprisingly, the same can be observed in the reconstructed amplitude, which is usually much more difficult to converge. Crops in the central region shown in Figures 5.9 provide better visualization of the grains in both reconstructions. However, the grain presents a better contrast and shape definition in the 6800 eV data (Figure 5.11.c, with a good resemblance between phase and amplitude, indicating a better reconstruction. Despite the grain is still visible in 10000 eV, the contrast is worse, and the grain boundaries are not well defined. The amplitude did not show satisfactory convergence in the higher energy reconstruction.

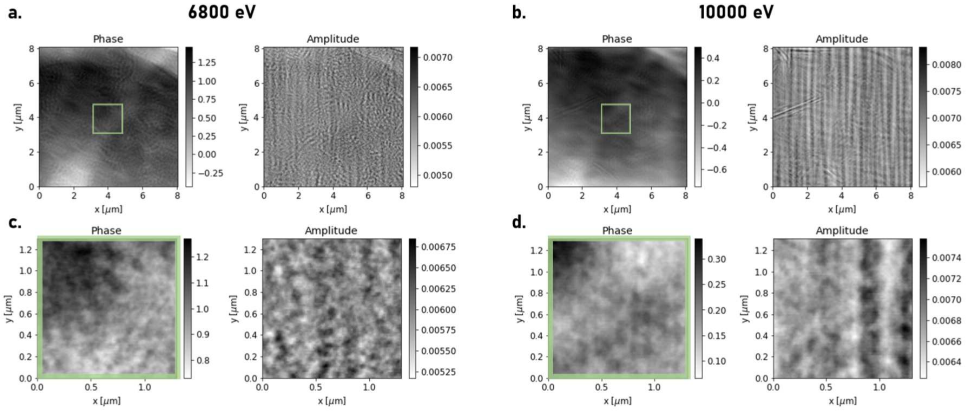

Figure 5.10: Radiation energy effect in the reconstruction. Reconstructed phase and amplitude for sample 40:38 in energies of (a) 6800 eV and (b) 10000 eV. (c) and (d) are zooms in (a) and (b), respectively, in the areas indicated by greeen squares. The zooms highlight the grains with ~120 nm. 6800 eV reconstruction shows a better definition of the grains.

In summary, despite the lower pixel size, the low energy acquisition has the advantage of better contrast in the grain boundaries. The higher energy acquisition has the advantage of definition in the micrometer morphology of the perovskite, in which case grain structure is still visible, but with lesser contrast.

5.2.6 Ptychography as a probe for early stages in the natural degradation process of perovskites

During the experiments at the beamline, the current at the ring was lost for 2 hours, with a simultaneous loss of nitrogen flow at the beamline leaving one of the 40:38 samples to air (52% rH) atmosphere. Just after the reinjection, the sample continued being measured in air atmosphere, until aging effects were noticed. The sample was changed and the environmental conditions were reestablished. The data of the aged sample, however, fortunately, showed interesting features related to the initial stages of segregation.

Figure 5.11.a show the ptychographic phase reconstructed at the beamline just after the return of the beam where the corrugation with a larger amount of matter is marked by the white strip on the diagonal, and some extra features with black contours (lesser amount of matter) can be observed. The colored fluorescence maps in Figure 5.11.b present the corrugations correlated to a higher amount of the main elements, but chemical marks of the new features can be found. After one hour of acquisition the measurements shown in Figures 5.11.c and .d reveal that the marks in the ptychography start to appear in the fluorescence maps as small strips following the same spatial pattern.

The black lines indicating an advance in the phase of the wavefront caused by the material are correlated to a decrease in the electronic density of the material in these regions, a consequence of a decrease in the total amount of matter. These regions with diminished amounts of matter presented only in the sample submitted in humid atmospheric conditions, followed by a heterogeneity created in the fluorescence after a prolonged period of exposure to harmful conditions, show an early stage of segregation/heterogenization of the film.

The pattern and sizes observed in these new structures have a resemblance with the hydrated and hexagonal phases structures observed in environmental scanning electron microscopy (ESEM) by Marchezi et al. [120] In their experiments in situ FEG-ESEM images were taken during the exposure of the 10:38 to a rH of 75% for 5 hours, to monitor the degradation reactions. They observed the first signs of degradation appearing after 1h of exposure to the humid atmosphere as hexagonal phases, and later emergence of hydrated phases. The group was capable of correlating the straight structures with hydrated phases and the small nodules that can be observed in Figure 5.11.a with the rise of small islands of hexagonal phases. However, they could not observe any compositional inhomogeneities, as the ones shown in the fluorescence maps in Figure 5.11.d. The decrease in the electronic density in these regions marked by the phase advance also corroborates the presence of hydrated phases since the water intercalation in the perovskite structure causes a volume expansion. [133] This evidence summed up to the fact that such structures were only observed in the sample submitted to the humid atmosphere leads to the hypothesis that it is a mark of the early stages of the degradation process by the H_2O intercalation in the structure.

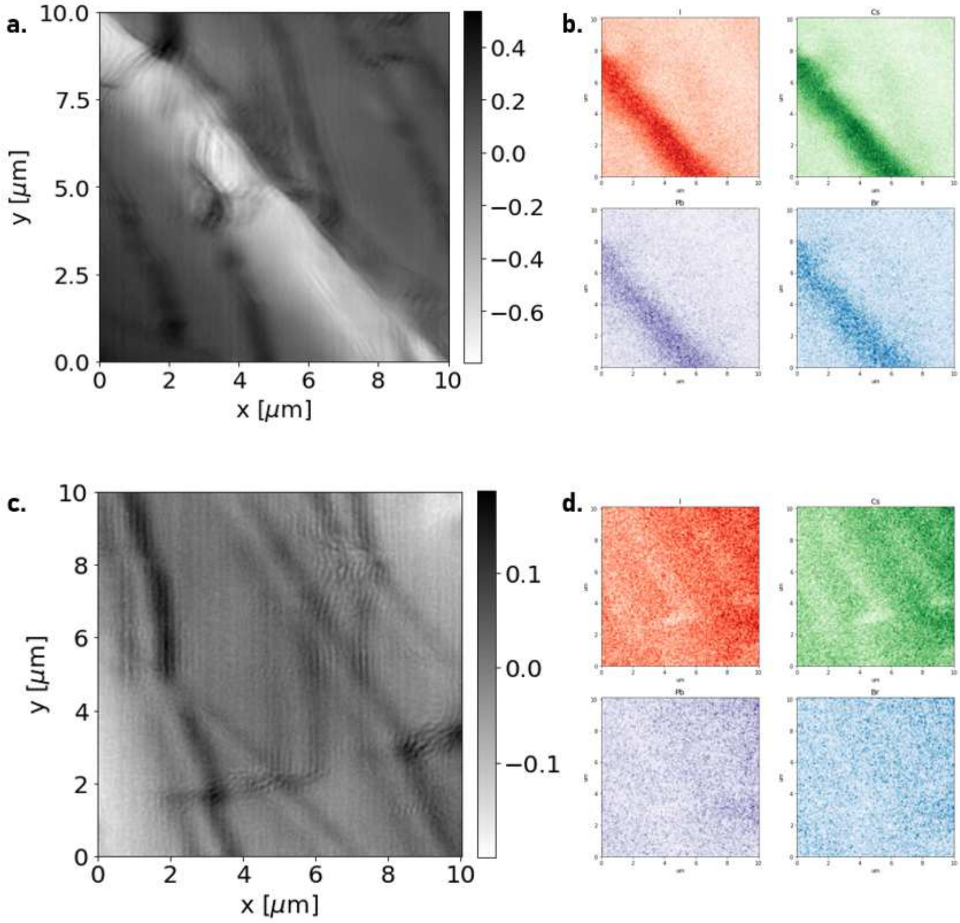

Figure 5.11: Early stages of perovskite degradation probed by x-ray ptychography and x-ray fluorescence. (a) and (c) are the reconstructed phases of two different positions of the sample separated by 1h of aging in humid atmosphere. (b) and (d) are the respect fluorescence maps of (a) and (b). The structures that appear in both reconstructions are attributed to hydrated phases of the perovskite with lower electronic density from the incorporation of water.

5.3 Correlative discussion

The observed stoichiometric variations in the Br/Pb ratio, coupled with intricate elemental distributions, underscore the complex heterogeneities inherent in Cs-rich perovskite compositions. This complexity aligns with recent literature, acknowledging the impact of local variations on the macroscopic behavior of perovskite materials [54]. The anti-correlation between Br content and the morphology gradient further hints at a structural influence on elemental distribution, challenging simplistic models. The interplay between stoichiometry and morphology echoes findings in similar perovskite systems, emphasizing the need for a comprehensive understanding of compositional heterogeneities [54].

XEOL experiments contribute valuable insights into the optoelectronic response's sensitivity to structural variations. The observed redshift in the XEOL signal, correlated with stoichiometric changes, aligns with recent studies highlighting the influence of halide composition on perovskite bandgaps [134]. The optimal experimental conditions for reaching the necessary stability of the sample are crucial for advancing perovskite applications, emphasizing the need for sustainable and reliable material behavior.

This multimodal analysis significantly contributes to the fundamental understanding of Cs-rich perovskite heterogeneities. It resonates with recent literature, providing a nuanced perspective on the intricate interplay between composition, structure, and optoelectronic properties [55] [54]. The correlation between structural, elemental, and optoelectronic aspects enriches our understanding and sets the stage for future studies, focusing on the dynamic evolution of these materials under controlled conditions [135] [136].

The observed stoichiometric variations in the Cs-rich perovskite samples, strongly correlated with micro-scale morphology, have direct implications for the material's optoelectronic response. Remarkably, despite the significant stoichiometric differences across the samples, the micro-scale grain morphology remains relatively unaffected. The intricate analysis conducted through advanced techniques sheds light on the structural and compositional aspects, providing valuable insights.

The observed stoichiometric variations in Cs-rich perovskite samples, despite their correlation with micro-scale morphology, may be attributed to the inherent compositional dynamics during the deposition process. Cs-containing perovskites are known for their sensitivity to processing conditions, and the observed variations could be linked to preferential segregation or redistribution of Cs ions during film formation. Literature suggests that subtle changes in precursor concentrations or annealing conditions can significantly impact the stoichiometry of perovskite films [137] [138] [139]

Ptychography measurements, performed at 10 keV with a scan area of 10x10 μm^2, elucidated the morphological intricacies at the micro-scale. The detailed reconstruction, employing Alternating Projections (AP) and Relaxed Averaged Alternating Reflections (RAAR) algorithms, highlighted variations in phase, indicative of electron density variations. The

30:38 sample, exhibiting larger wrinkles, showcased a distinctive 0.9 phase delay, consistent with higher material density. The reconstructed morphology revealed pronounced corrugations and additional examination disclosed submicrometer structures resembling fish scales or flakes.

The uniformity of micro-scale grain morphology across different stoichiometric compositions suggests that the growth dynamics during deposition play a crucial role. It aligns with studies indicating that certain perovskite compositions exhibit robust morphological features, resisting significant changes under specific deposition conditions [140], in particular for the samples deposited over mylar in which the annealing process is softer due to the lesser temperature that the substrates reaches compared to other substrates. This is further discussed in Appendix A.

Despite the discernible micrometer-scale corrugations, a detailed examination of Figure 5.8.d indicated a uniform distribution of 120 nm grains. Notably, the grain distribution appeared consistent across hill and valley regions. Nanodiffraction experiments further revealed a variation in lattice parameters with subtle decrease in average lattice parameters with increasing Cs content, aligned with predictions. This concurrence supports recent discussions on the influence of Cs incorporation on the crystal lattice structure, yet no definitive correlation with the morphology.

The lack of a clear correlation between lattice parameter variations and morphology may stem from the limitations of the nanodiffraction technique. The difficulty in measuring single-grain strain fields due to the polycrystalline nature of the samples might obscure subtle variations.

The lack of a clear correlation between lattice parameter variations and micro-scale morphology may stem from the intricate interplay between halide content variations and crystal structure in Cs-rich perovskite films. While the stoichiometric variations between the films primarily involve the Cs content, halide composition (specifically iodine content) also plays a crucial role in determining the properties of perovskite films.

One potential explanation for the observed complexity is the non-uniform distribution of halides within the hill and /or valley regions of the film. [141] Halide segregation, either at grain boundaries or within specific crystallographic planes, could introduce localized variations in the lattice parameters that trouble the data segmentation due to the low statistics during the acquisition. Nanodiffraction techniques may face challenges in capturing these nuanced halide-induced changes, especially in polycrystalline samples where the distribution of halides might not be uniform across all grains. Furthermore, variations in halide composition led to changes in the electronic structure and bandgap of the perovskite film as observed in the XEOL experiments. The electronic properties of Cs-rich perovskites are known to be sensitive to halide composition, affecting their optoelectronic performance. This interdependence of halide content and electronic structure adds another layer of complexity to the relationship between stoichiometry-driven lattice parameter changes and micro-scale morphology.

Defects or strain fields within the grains could also contribute to the observed variations, with halide-induced distortions interacting with the lattice structure. The intricate coupling of halide content, crystal structure, and micro-scale morphology underscores the need for comprehensive characterization techniques. Advanced methods such as micro-Laue [142] [143] and BCDI [144] could offer higher resolution and statistical relevance, enabling a more detailed investigation of halide distribution and its impact on lattice parameters at the nanoscale. To unravel the complete picture, integrating nanodiffraction data with advanced characterization techniques becomes imperative. This holistic approach will not only enhance our understanding of the role of halide content in the observed variations but also shed light on the intricate relationship between composition, crystal structure, and micro-scale morphology in Cs-rich perovskite materials.

In an effort to enhance resolution and contrast, the incident photon energy was varied between 6800 eV and 10000 eV. Lower energy acquisition at 6800 eV exhibited superior contrast in grain boundaries, while higher energy at 10000 eV provided clarity in micrometer morphology. This observation underscores the significance of incident photon energy in influencing ptychography reconstruction outcomes.

The observed influence of incident photon energy on ptychography reconstruction outcomes aligns with fundamental principles of X-ray interactions. Lower energy acquisitions enhance sensitivity to weakly scattering materials, improving contrast in grain boundaries. This strategy finds precedence in coherent diffractive imaging experiments for biological samples [145].

Unexpectedly, an interruption in beamline operations provided an opportunity to capture the early stages of degradation. Ptychography measurements on the aged 40:38 sample unveiled phase features indicative of material loss, corroborated by fluorescence maps. The appearance of small strips following a distinct spatial pattern suggested the initiation of segregation or heterogenization. This phenomenon bears resemblance to structures observed in environmental scanning electron microscopy (ESEM) during degradation studies. The observed hydrated and hexagonal phases in the aged sample align with findings by Marchezi et al. [120], who identified similar structures during exposure to humid conditions. The decrease in electronic density in regions exhibiting phase advance is indicative of water intercalation and volume expansion, reinforcing the hypothesis of early-stage degradation.

The observation of early-stage degradation features in aged samples could be attributed to the infiltration of water molecules into the perovskite structure, causing changes in electron density. This aligns with studies indicating the susceptibility of perovskite films to environmental conditions, leading to phase transformations and structural degradation [16] [146] The comprehensive analysis presented herein contributes to the understanding of Cs-rich perovskite materials' intricate behavior at the micro-scale. The correlation between stoichiometry, morphology, and optoelectronic response opens avenues for targeted material design. Future work could leverage computational modeling to validate experimental findings and explore the impact of varied processing conditions. The observed early-stage degradation phenomena underscore the importance of environmental stability in perovskite applications, warranting further investigations into degradation mechanisms and mitigation strategies.

5.4 Conclusions

X-ray ptychography, XRF, XEOL, and nanodiffraction experiments were conducted at the CARNAUBA X-ray nanoprobe beamline (SIRIUS/LNLS) to investigate metal halide perovskite (MHP) materials. The study focuses on the correlation among morphology, stoichiometric chemical distribution (X-ray fluorescence - XRF), and optoelectronic response (X-ray excited optical luminescence - XEOL) of $Cs_xFA_{1-x}Pb(Br_{0.38}I_{0.62})_3$ thin films deposited on mylar substrates providing a cost-effective alternative for X-ray transmission techniques.

XRF maps revealed a correlation between the wrinkled morphology and variations in Br:Pb stoichiometry. The Br:Pb ratio, especially in smaller regions, showed an anticorrelation with the morphology gradient, indicating stoichiometric variations associated with the wrinkles. XEOL experiments demonstrated variations in luminescence intensity and energy position correlated with the morphology. The luminescence signal exhibited a redshift as the X-ray beam crossed the wrinkles, consistent with the Br:Pb ratio maps.

Ptychography in phase contrast (10 nm pixel size @10 keV) reveals morphological aspects not visible in traditional scanning transmission. The possibility of measuring in fly-scan mode and N_2 atmosphere was essential to mitigate damages, typically the main limiting factor to applying the CDI in such samples. And the results in multispectral images of MHP are a paramount step in developing and applying the technique in beam-sensitive samples for high-resolution imaging. The reconstructions revealed variations in phase and amplitude, highlighting features such as wrinkles, grain structures, and submicrometer details. Despite these correlated changes in the chemical proportions and the wrinkle morphology, no changes in the grain size or morphology were observed. The ptychography however, indicated ~700 nm grains agglomerations, where the ~120 nm grain seems to be more coalesced. Further studies with ptychography as the energy optimization for reconstructions and the application for the study of early stages in natural degradation were performed.

Overall, the study employed a combination of advanced X-ray techniques to unravel the complex correlations among morphology, stoichiometry, and optoelectronic properties in metal halide perovskite materials. The findings contribute to the understanding of perovskite behavior under different conditions, offering insights into potential applications and challenges, particularly in the context of hierarchical processes.

CHAPTER 6

GENERAL CONCLUSIONS AND PROSPECTS

The study employed a multi-technique approach, combining synchrotron techniques with non-synchrotron methods. This strategy, which included X-ray diffraction, atomic force microscopy, scanning electron microscopy, micro-photoluminescence, and cathodoluminescence, provided a thorough understanding of the structural, morphological, and optical aspects of the perovskite films.

The use of various characterization techniques revealed spatial and compositional variations within the perovskite films. The correlation between morphology and XEOL, as observed in photoluminescence and cathodoluminescence mapping, suggests that the film's microstructure plays a crucial role in determining its optical properties.

The incorporation of cesium (Cs) in perovskite compositions influenced the material's properties, leading to shifts in X-ray diffraction peaks, changes in luminescence emission energies, and variations in film morphology. The study highlighted the importance of understanding and controlling Cs content for tailoring perovskite film properties.

The comparison of photoluminescence, cathodoluminescence, and X-ray-excited optical luminescence emphasized the significance of penetration depth in each technique. While visible light in photoluminescence primarily probed the surface, 10 kV electrons in cathodoluminescence explored subsurface structures, and X-rays in X-ray excited optical luminescence provided insights into bulk properties.

Controlling X-ray beam dose and environment, such as using an inert N_2 atmosphere, emerged as a strategy to mitigate damage to the perovskite films during characterization. This optimization allowed efficient probing of material properties with reduced harm. And made it possible to perform the first ptychography measurement in hybrid perovskites. Further application of the ptychography observed micrometer-scale corrugations, indicative of strain relief during annealing, are distinctly captured. The larger phase shifts associated with these corrugations suggest a higher density of material, aligning with the observed topographical features. Notably, the width and height of these wrinkles exhibit variations among different compositions, emphasizing the sensitivity of ptychography to subtle structural changes.

Examining specific compositions, such as the 20:38 and 40:38 samples, reveals the capability of ptychography to capture details in the sub-micrometer range. The oscillations in the phase shift, on the order of hundreds of nanometers, correspond to fine features within the material. These features, as suggested by the comparisons with SEM data, could be associated with clusters of grains organized in a flake-like structure.

The parallel use of various techniques, both synchrotron and non-synchrotron, offered a holistic perspective on the properties of metal halide perovskite films. This approach facilitated cross-validation of results and contributed to a more comprehensive understanding of the material.

The choice of substrate, such as mylar or glass, has a substantial impact on the properties of metal halide perovskite (MHP) films. Variations in grain sizes, morphology, and luminescent characteristics were observed between different substrates, emphasizing the need to consider substrate effects in perovskite research.

In summary, the study underscores the complexity of metal halide perovskite films, demonstrating the intricate interplay between substrate choice, composition, morphology, and luminescent properties. The multi-technique and parallel characterization approach presented in the research contribute valuable insights for advancing the understanding and application of perovskite materials. As consequence, we foresee that these results pave the way to new correlative in-situ and in-operando experiments with hybrid perovskites. Also, the ptychography is prospect as a new probe for the early stages of degradation that were once inaccessible to the other techniques.

BIBLIOGRAPHY

[1] Zhou, Y., Zhou, H., Deng, J., Cha, W. & Cai, Z. Decisive structural and functional characterization of halide perovskites with synchrotron. *Matter* **2**, 360–377 (2020).

[2] Kodur, M. *et al.* X-ray microscopy of halide perovskites: techniques, applications, and prospects. *Advanced Energy Materials* **10**, 1903170 (2020).

[3] Tolentino, H. C. *et al.* The carnaúba x-ray nanospectroscopy beamline at the sirius-lnls synchrotron light source: developments, commissioning, and first science at the tarumã station. *Journal of Electron Spectroscopy and Related Phenomena* 147340 (2023).

[4] Sá, F., Liu, L., Resende, X. & Rodrigues, A. A new booster synchrotron for the sirius project. *Proc. IPAC'14* 1959–1961 (2014).

[5] Mathews, I. *et al.* Economically sustainable growth of perovskite photovoltaics manufacturing. *Joule* **4**, 822–839 (2020).

[6] Chen, W.-H. *et al.* Simple fabrication of perovskite solar cells with enhanced efficiency, stability, and flexibility under ambient air. *Journal of Power Sources* **442**, 227216 (2019).

[7] Guo, N. *et al.* A simple fabrication of ch3nh3pbi3 perovskite for solar cells using low-purity pbi2. *Journal of Semiconductors* **38**, 014004 (2017).

[8] Niu, X., Li, N., Chen, Q. & Zhou, H. Insights into large-scale fabrication methods in perovskite photovoltaics. *Advanced Energy and Sustainability Research* **2**, 2000046 (2021).

[9] Kim, J. Y., Lee, J.-W., Jung, H. S., Shin, H. & Park, N.-G. High-efficiency perovskite solar cells. *Chemical reviews* **120**, 7867–7918 (2020).

[10] Liu, S., Biju, V. P., Qi, Y., Chen, W. & Liu, Z. Recent progress in the development of high-efficiency inverted perovskite solar cells. *NPG Asia Materials* **15**, 27 (2023).

[11] Moseley, O. D., Doherty, T. A., Parmee, R., Anaya, M. & Stranks, S. D. Halide perovskites scintillators: unique promise and current limitations. *Journal of Materials Chemistry C* **9**, 11588–11604 (2021).

[12] Birowosuto, M. *et al.* X-ray scintillation in lead halide perovskite crystals. *Scientific reports* **6**, 37254 (2016).

[13] Zaffalon, M. L. *et al.* Extreme γ-ray radiation hardness and high scintillation yield in perovskite nanocrystals. *Nature Photonics* **16**, 860–868 (2022).

[14] Szostak, R. *et al.* In situ and operando characterizations of metal halide perovskite and solar cells: Insights from lab-sized devices to upscaling processes. *Chemical reviews* **123**, 3160–3236 (2023).

[15] Szostak, R., Tolentino, H. C. N. & Nogueira, A. F. Synchrotron-based characterization of metal halide perovskites: advances and prospects from brazilian synchrotron light laboratory sources. *Oxford Open Energy* **1**, oiac006 (2022).

[16] da Silva, F. M. *et al.* Disentangling x-ray and sunlight irradiation effects under a controllable atmosphere in metal halide perovskites. *Solar RRL* **7**, 2200898 (2023).

[17] Guaita, M. G. *et al.* Influence of methylammonium chloride on wide-bandgap halide perovskites films for solar cells. *Advanced Functional Materials* 2307104 (2023).

[18] Szostak, R. *et al.* Revealing the perovskite film formation using the gas quenching method by in situ giwaxs: morphology, properties, and device performance. *Advanced Functional Materials* **31**, 2007473 (2021).

[19] Chapman, H. N. Fourth-generation light sources (2023).

[20] De Wolf, S. *et al.* Organometallic halide perovskites: sharp optical absorption edge and its relation to photovoltaic performance. *The journal of physical chemistry letters* **5**, 1035–1039 (2014).

[21] Sutherland, B. R. & Sargent, E. H. Perovskite photonic sources. *Nature Photonics* **10**, 295–302 (2016).

[22] Hoke, E. T. *et al.* Reversible photo-induced trap formation in mixed-halide hybrid perovskites for photovoltaics. *Chemical Science* **6**, 613–617 (2015).

[23] Bush, K. A. *et al.* Controlling thin-film stress and wrinkling during perovskite film formation. *ACS Energy Letters* **3**, 1225–1232 (2018).

[24] Slotcavage, D. J., Karunadasa, H. I. & McGehee, M. D. Light-induced phase segregation in halide-perovskite absorbers. *ACS Energy Letters* **1**, 1199–1205 (2016).

[25] Iagher, L. & Etgar, L. Effect of cs on the stability and photovoltaic performance of 2d/3d perovskite-based solar cells. *ACS Energy Letters* **3**, 366–372 (2018).

[26] Saliba, M. *et al.* Cesium-containing triple cation perovskite solar cells: improved stability, reproducibility and high efficiency. *Energy & environmental science* **9**, 1989–1997 (2016).

[27] Fan, X. Advanced progress in metal halide perovskite solar cells: A review. *Materials Today Sustainability* 100603 (2023).

[28] Li, Y. *et al.* A review on morphology engineering for highly efficient and stable hybrid perovskite solar cells. *Journal of Materials Chemistry A* **6**, 12842–12875 (2018).

[29] Kim, G.-H. & Kim, D. S. Development of perovskite solar cells with> 25% conversion efficiency. *Joule* **5**, 1033–1035 (2021).

[30] Aydin, E. *et al.* Pathways toward commercial perovskite/silicon tandem photovoltaics. *Science* **383**, eadh3849 (2024).

[31] Cherepakhin, A. *et al.* Advanced laser nanofabrication technologies for perovskite photonics. *Advanced Optical Materials* 2302782 (2024).

[32] Zhang, Q., Shang, Q., Su, R., Do, T. T. H. & Xiong, Q. Halide perovskite semiconductor lasers: materials, cavity design, and low threshold. *Nano Letters* **21**, 1903–1914 (2021).

[33] Karabchevsky, A. Perovskite beyond solar: toward novel developments of lasers and detectors for photonic circuits. *Light: Science & Applications* **12**, 160 (2023).

[34] Zhu, H. *et al.* Long-term operating stability in perovskite photovoltaics. *Nature Reviews Materials* **8**, 569–586 (2023).

[35] Chowdhury, T. A. *et al.* Stability of perovskite solar cells: issues and prospects. *RSC advances* **13**, 1787–1810 (2023).

[36] Zhang, Z., Wang, H., Jacobsson, T. J. & Luo, J. Big data driven perovskite solar cell stability analysis. *Nature Communications* **13**, 7639 (2022).

[37] Wang, Y. *et al.* Encapsulation and stability testing of perovskite solar cells for real life applications. *ACS Materials Au* **2**, 215–236 (2022).

[38] Li, J. *et al.* Encapsulation of perovskite solar cells for enhanced stability: Structures, materials and characterization. *Journal of Power Sources* **485**, 229313 (2021).

[39] Knight, A. J. *et al.* Halide segregation in mixed-halide perovskites: influence of a-site cations. *ACS Energy Letters* **6**, 799–808 (2021).

[40] Hieulle, J. *et al.* Unraveling the impact of halide mixing on perovskite stability. *Journal of the American Chemical Society* **141**, 3515–3523 (2019).

[41] Crespo, C. T. The effect of the halide anion on the optical properties of lead halide perovskites. *Solar Energy Materials and Solar Cells* **195**, 269–273 (2019).

[42] Meloni, S., Palermo, G., Ashari-Astani, N., Grätzel, M. & Rothlisberger, U. Valence and conduction band tuning in halide perovskites for solar cell applications. *Journal of Materials Chemistry A* **4**, 15997–16002 (2016).

[43] Motti, S. G. *et al.* Phase segregation in mixed-halide perovskites affects charge-carrier dynamics while preserving mobility. *Nature Communications* **12**, 6955 (2021).

[44] Chen, S. *et al.* The lattice reconstruction of cs-introduced fapbi 1.80 br 1.20 enables improved stability for perovskite solar cells. *RSC advances* **11**, 3997–4005 (2021).

[45] Sutanto, A. A. *et al.* Pushing the limit of cs incorporation into fapbbr3 perovskite to enhance solar cells performances. *APL Materials* **7** (2019).

[46] Tang, S., Huang, S., Wilson, G. J. & Ho-Baillie, A. Progress and opportunities for cs incorporated perovskite photovoltaics. *Trends in Chemistry* **2**, 638–653 (2020).

[47] Goldschmidt, V. M. Die gesetze der krystallochemie. *Naturwissenschaften* **14**, 477–485 (1926).

[48] Ji, D. *et al.* Regulatory tolerance and octahedral factors by using vacancy in apbi3 perovskites. *Vacuum* **164**, 186–193 (2019).

[49] Zhang, C.-X. *et al.* Reviewing and understanding the stability mechanism of halide perovskite solar cells. *InfoMat* **2**, 1034–1056 (2020).

[50] Choi, D.-H. *et al.* The effect of cs/fa ratio on the long-term stability of mixed cation perovskite solar cells. *Solar RRL* **5**, 2100660 (2021).

[51] Han, G. *et al.* Additive selection strategy for high performance perovskite photovoltaics. *The Journal of Physical Chemistry C* **122**, 13884–13893 (2018).

[52] Hsiao, Y.-W. *et al.* Effects of cesium content on the triple-cation lead halide perovskite photodetectors with enhanced detectivity and response time. *Journal of Alloys and Compounds* **889**, 161621 (2021).

[53] Ašmontas, S. *et al.* Impact of cesium concentration on optoelectronic properties of metal halide perovskites. *Materials* **15**, 1936 (2022).

[54] Braunger, S. *et al.* Cs x fa1–x pb (i1–y br y) 3 perovskite compositions: the appearance of wrinkled morphology and its impact on solar cell performance. *The Journal of Physical Chemistry C* **122**, 17123–17135 (2018).

[55] Kim, S.-G. *et al.* How antisolvent miscibility affects perovskite film wrinkling and photovoltaic properties. *Nature communications* **12**, 1554 (2021).

[56] Willmott, P. *An introduction to synchrotron radiation: techniques and applications* (John Wiley & Sons, 2019).

[57] Westfahl, H. *et al.* X-ray microscopy at sirius, the new brazilian synchrotron light source. *Microscopy and Microanalysis* **24**, 172–175 (2018).

[58] Tolentino, H. C. *et al.* Carnaúba: the coherent x-ray nanoprobe beamline for the brazilian synchrotron sirius/lnls. In *Journal of Physics: Conference Series*, vol. 849, 012057 (IOP Publishing, 2017).

[59] da Silva, F. *et al.* An innovative optical element for x-ray beam aperture, monitoring, and diagnostic at the carnaúba beamline at sirius/lnls. In *Journal of Physics: Conference Series*, vol. 2380, 012062 (IOP Publishing, 2022).

[60] Moreno, G. *et al.* Exactly-constrained kb mirrors for sirius/lnls beamlines: Design and commissioning of the tarumã station nanofocusing optics at carnaúba beamline. *Proc. MEDSI* **2021** (2020).

[61] Silva, M. S. *et al.* Four-bounce crystal monochromators for the sirius/lnls beamlines (2020).

[62] Tolentino, H. C. *et al.* Innovative instruments based on cryogenically cooled silicon crystals for the carnaúba beamline at sirius-lnls. In *AIP Conference Proceedings*, vol. 2054 (AIP Publishing, 2019).

[63] Bueno, C. *et al.* Vibration assessment at the carnaúba beamline at sirius/lnls. *JACoW, MEDSI2020: MOPB08* (2021).

[64] Geraldes, R. *et al.* Design and commissioning of the tarumã station at the carnaúba beamline at sirius/lnls. In *11th Int. Conf. on Mechanical Engineering Design of Synchrotron Radiation Equipment and Instrumentation (MEDSI2020), Chicago, IL, USA, virtual conference* (2021).

[65] Geraldes, R. R. *et al.* The high-dynamic cryogenic sample stage for sapoti/carnaúba at sirius/lnls. In *AIP Conference Proceedings*, vol. 2990 (AIP Publishing, 2023).

[66] Cooper, M., Mijnarends, P., Shiotani, N., Sakai, N. & Bansil, A. *X-ray Compton scattering*, vol. 5 (OUP Oxford, 2004).

[67] Solé, V. A., Papillon, E., Cotte, M., Walter, P. & Susini, J. A multiplatform code for the analysis of energy-dispersive x-ray fluorescence spectra. *Spectrochimica Acta Part B: Atomic Spectroscopy* **62**, 63–68 (2007).

[68] Lider, V. V. X-ray fluorescence imaging. *Physics-Uspekhi* **61**, 980 (2018).

[69] Hammond, C. *The basics of crystallography and diffraction*, vol. 21 (International Union of Crystallography texts on crystallography, 2015).

[70] Ameh, E. A review of basic crystallography and x-ray diffraction applications. *The international journal of advanced manufacturing technology* **105**, 3289–3302 (2019).

[71] Schülli, T. U. & Leake, S. J. X-ray nanobeam diffraction imaging of materials. *Current Opinion in Solid State and Materials Science* **22**, 188–201 (2018).

[72] Lim, B. *et al.* A convolutional neural network for defect classification in bragg coherent x-ray diffraction. *npj Computational Materials* **7**, 115 (2021).

[73] Vicente, R. A., Neckel, I. T., Sankaranarayanan, S. K., Solla-Gullon, J. & Fernández, P. S. Bragg coherent diffraction imaging for in situ studies in electrocatalysis. *ACS nano* **15**, 6129–6146 (2021).

[74] Gao, Y. *et al.* Modeling and experimental validation of dynamical effects in bragg coherent x-ray diffractive imaging of finite crystals. *Physical Review B* **106**, 184111 (2022).

[75] Leake, S. J. *et al.* The nanodiffraction beamline id01/esrf: a microscope for imaging strain and structure. *Journal of synchrotron radiation* **26**, 571–584 (2019).

[76] Le Bolloc'h, D., Bellec, E., Kirova, N. & Jacques, V. L. Tracking defects of electronic crystals by coherent x-ray diffraction. *Symmetry* **15**, 1449 (2023).

[77] Hruszkewycz, S. O. *et al.* High-resolution three-dimensional structural microscopy by single-angle bragg ptychography. *Nature materials* **16**, 244–251 (2017).

[78] Li, J., Liu, L. & Sham, T.-K. 2d xanes–xeol spectroscopy studies of morphology-dependent phase transformation and corresponding luminescence from hierarchical tio2 nanostructures. *Chemistry of Materials* **27**, 3021–3029 (2015).

[79] Wang, Z., Guo, X. & Sham, T.-K. 2d xanes-xeol mapping: observation of enhanced band gap emission from zno nanowire arrays. *Nanoscale* **6**, 6531–6536 (2014).

[80] Nussenzveig, H. M. *Curso de física básica: Ótica, relatividade, física quântica (vol. 4)* (Editora Blucher, 2014).

[81] Jackson, J. D. Classical electrodynamics (1999).

[82] Thibault, P. *Algorithmic methods in diffraction microscopy* (2007).

[83] Sayre, D. Some implications of a theorem due to shannon. *Acta Crystallographica* **5**, 843–843 (1952).

[84] Shannon, C. E. Communication in the presence of noise. *Proceedings of the IEEE* **72**, 1192–1201 (1984).

[85] Jerri, A. J. The shannon sampling theorem—its various extensions and applications: A tutorial review. *Proceedings of the IEEE* **65**, 1565–1596 (1977).

[86] Miao, J., Ishikawa, T., Robinson, I. K. & Murnane, M. M. Beyond crystallography: Diffractive imaging using coherent x-ray light sources. *Science* **348**, 530–535 (2015).

[87] Marchesini, S. *et al.* Coherent x-ray diffractive imaging: applications and limitations. *Optics Express* **11**, 2344–2353 (2003).

[88] Prosekov, P., Nosik, V. & Blagov, A. Methods of coherent x-ray diffraction imaging. *Crystallography Reports* **66**, 867–882 (2021).

[89] Van Heel, M. & Schatz, M. Fourier shell correlation threshold criteria. *Journal of structural biology* **151**, 250–262 (2005).

[90] Marchesini, S., Tu, Y.-C. & Wu, H.-t. Alternating projection, ptychographic imaging and phase synchronization. *Applied and Computational Harmonic Analysis* **41**, 815–851 (2016).

[91] Luke, D. R. Relaxed averaged alternating reflections for diffraction imaging. *Inverse problems* **21**, 37 (2004).

[92] Picoreti, R. & Westfahl Jr, H. Sirius facility update. *Synchrotron Radiation News* **34**, 12–13 (2021).

[93] Kot, M. *et al.* In situ near-ambient pressure x-ray photoelectron spectroscopy reveals the influence of photon flux and water on the stability of halide perovskite. *ChemSusChem* **13**, 5722–5730 (2020).

[94] Svanström, S. *et al.* X-ray stability and degradation mechanism of lead halide perovskites and lead halides. *Physical Chemistry Chemical Physics* **23**, 12479–12489 (2021).

[95] Ferrer Orri, J. *et al.* Unveiling the interaction mechanisms of electron and x-ray radiation with halide perovskite semiconductors using scanning nanoprobe diffraction. *Advanced Materials* **34**, 2200383 (2022).

[96] Stuckelberger, M. E. *et al.* Effects of x-rays on perovskite solar cells. *The Journal of Physical Chemistry C* **124**, 17949–17956 (2020).

[97] Scalon, L. *et al.* Improving the stability and efficiency of perovskite solar cells by a bidentate anilinium salt. *JACS Au* **2**, 1306–1312 (2022).

[98] Chen, H. *et al.* Regulating surface potential maximizes voltage in all-perovskite tandems. *Nature* **613**, 676–681 (2023).

[99] Park, J. *et al.* Controlled growth of perovskite layers with volatile alkylammonium chlorides. *Nature* **616**, 724–730 (2023).

[100] Kim, J. S. *et al.* Ultra-bright, efficient and stable perovskite light-emitting diodes. *Nature* **611**, 688–694 (2022).

[101] Sun, Y. *et al.* Bright and stable perovskite light-emitting diodes in the near-infrared range. *Nature* **615**, 830–835 (2023).

[102] Deumel, S. *et al.* High-sensitivity high-resolution x-ray imaging with soft-sintered metal halide perovskites. *Nature Electronics* **4**, 681–688 (2021).

[103] Perini, C. A., Doherty, T. A., Stranks, S. D., Correa-Baena, J.-P. & Hoye, R. L. Pressing challenges in halide perovskite photovoltaics—from the atomic to module level. *Joule* **5**, 1024–1030 (2021).

[104] Correa-Baena, J.-P. *et al.* Homogenized halides and alkali cation segregation in alloyed organic-inorganic perovskites. *Science* **363**, 627–631 (2019).

[105] Frohna, K. *et al.* Nanoscale chemical heterogeneity dominates the optoelectronic response of alloyed perovskite solar cells. *Nature Nanotechnology* **17**, 190–196 (2022).

[106] Macpherson, S. *et al.* Local nanoscale phase impurities are degradation sites in halide perovskites. *Nature* **607**, 294–300 (2022).

[107] Li, N. *et al.* Microscopic degradation in formamidinium-cesium lead iodide perovskite solar cells under operational stressors. *Joule* **4**, 1743–1758 (2020).

[108] Pfeiffer, F. X-ray ptychography. *Nature Photonics* **12**, 9–17 (2018).

[109] Schulz, P. *et al.* Electronic level alignment in inverted organometal perovskite solar cells. *Advanced Materials Interfaces* **2**, 1400532 (2015).

[110] Ma, C. *et al.* Unveiling facet-dependent degradation and facet engineering for stable perovskite solar cells. *Science* **379**, 173–178 (2023).

[111] Chen, S. *et al.* Transmission electron microscopy of organic-inorganic hybrid perovskites: myths and truths. *Science Bulletin* **65**, 1643–1649 (2020).

[112] Rothmann, M. U. *et al.* Structural and chemical changes to ch3nh3pbi3 induced by electron and gallium ion beams. *Advanced Materials* **30**, 1800629 (2018).

[113] Lena, F. *et al.* Commissioning of the cryogenic sample environment for the tarumã station at the carnaúba beamline at sirius/lnls. In *Journal of Physics: Conference Series*, vol. 2380, 012108 (IOP Publishing, 2022).

[114] Mettler, F. Basic radiation physics, chemistry, and biology. *Medical effects of ionizing radiation* **1** (1985).

[115] Szostak, R. *et al.* Nanoscale mapping of chemical composition in organic-inorganic hybrid perovskite films. *Science advances* **5**, eaaw6619 (2019).

[116] Delport, G., Macpherson, S. & Stranks, S. D. Imaging carrier transport properties in halide perovskites using time-resolved optical microscopy. *Advanced Energy Materials* **10**, 1903814 (2020).

[117] Stenn, K. & Bahr, G. Specimen damage caused by the beam of the transmission electron microscope, a correlative reconsideration. *Journal of ultrastructure research* **31**, 526–550 (1970).

[118] Egerton, R., Li, P. & Malac, M. Radiation damage in the tem and sem. *Micron* **35**, 399–409 (2004).

[119] Godding, J. S. *et al.* Oxidative passivation of metal halide perovskites. *Joule* **3**, 2716–2731 (2019).

[120] Marchezi, P. E. *et al.* Degradation mechanisms in mixed-cation and mixed-halide cs x fa 1- x pb (br y i 1- y) 3 perovskite films under ambient conditions. *Journal of Materials Chemistry A* **8**, 9302–9312 (2020).

[121] Zhuang, J., Wang, J. & Yan, F. Review on chemical stability of lead halide perovskite solar cells. *Nano-Micro Letters* **15**, 84 (2023).

[122] Juarez-Perez, E. J., Ono, L. K. & Qi, Y. Thermal degradation of formamidinium based lead halide perovskites into sym-triazine and hydrogen cyanide observed by coupled thermogravimetry-mass spectrometry analysis. *Journal of Materials Chemistry A* **7**, 16912–16919 (2019).

[123] Juarez-Perez, E. J., Hawash, Z., Raga, S. R., Ono, L. K. & Qi, Y. Thermal degradation of ch 3 nh 3 pbi 3 perovskite into nh 3 and ch 3 i gases observed by coupled thermogravimetry–mass spectrometry analysis. *Energy & environmental science* **9**, 3406–3410 (2016).

[124] Srivastava, S. *et al.* Advanced spectroscopic techniques for characterizing defects in perovskite solar cells. *Communications Materials* **4**, 52 (2023).

[125] Liu, L. *et al.* Status of sirius operation with users. In *Proc. 14th International Particle Accelerator Conference-IPAC*, vol. 23.

[126] Jones, M. W., Hare, D. J., James, S. A., de Jonge, M. D. & McColl, G. Radiation dose limits for bioanalytical x-ray fluorescence microscopy. *Analytical Chemistry* **89**, 12168–12175 (2017).

[127] Beal, R. E. *et al.* Structural origins of light-induced phase segregation in organic-inorganic halide perovskite photovoltaic materials. *Matter* **2**, 207–219 (2020).

[128] García-Batlle, M. *et al.* Effective ion mobility and long-term dark current of metal halide perovskites with different crystallinities and compositions. *Advanced Photonics Research* **3**, 2200136 (2022).

[129] Deng, J. *et al.* X-ray ptychographic and fluorescence microscopy of frozen-hydrated cells using continuous scanning. *Scientific Reports* **7**, 445 (2017).

[130] Deng, J. *et al.* Correlative 3d x-ray fluorescence and ptychographic tomography of frozen-hydrated green algae. *Science advances* **4**, eaau4548 (2018).

[131] Deng, J. *et al.* Advances and challenges in cryo ptychography at the advanced photon source. In *AIP conference proceedings*, vol. 1696 (AIP Publishing, 2016).

[132] Rodriguez, J. A., Xu, R., Chen, C.-C., Zou, Y. & Miao, J. Oversampling smoothness: an effective algorithm for phase retrieval of noisy diffraction intensities. *Journal of applied crystallography* **46**, 312–318 (2013).

[133] Jong, U.-G. *et al.* Influence of water intercalation and hydration on chemical decomposition and ion transport in methylammonium lead halide perovskites. *Journal of Materials Chemistry A* **6**, 1067–1074 (2018).

[134] Dolan, C. J. *et al.* Scanning x-ray excited optical luminescence of heterogeneity in halide perovskite alloys. *Journal of Physics D: Applied Physics* **56**, 034002 (2022).

[135] Chen, J., Lv, J., Liu, X., Lin, J. & Chen, X. A study on theoretical models for investigating time-resolved photoluminescence in halide perovskites. *Physical Chemistry Chemical Physics* **25**, 7574–7588 (2023).

[136] Teixeira, V. C. *et al.* X-ray excited optical luminescence at carnaúba, the sirius x-ray nanoprobe beamline. *Optical Materials: X* **20**, 100278 (2023).

[137] Li, B., Binks, D., Cao, G. & Tian, J. Engineering halide perovskite crystals through precursor chemistry. *Small* **15**, 1903613 (2019).

[138] Yuan, Z. *et al.* Unveiling the synergistic effect of precursor stoichiometry and interfacial reactions for perovskite light-emitting diodes. *Nature communications* **10**, 2818 (2019).

[139] Wargulski, D. R. *et al.* Relationship between the annealing temperature and the presence of pbi2 platelets at the surfaces of slot-die-coated triple-halide perovskite thin films. *ACS Applied Materials & Interfaces* **15**, 41516–41524 (2023).

[140] Li, Z. *et al.* Stabilizing perovskite structures by tuning tolerance factor: formation of formamidinium and cesium lead iodide solid-state alloys. *Chemistry of Materials* **28**, 284–292 (2016).

[141] Long, M. *et al.* Abnormal synergetic effect of organic and halide ions on the stability and optoelectronic properties of a mixed perovskite via in situ characterizations. *Advanced Materials* **30**, 1801562 (2018).

[142] Zhou, G. *et al.* Quantitative scanning laue diffraction microscopy: application to the study of 3d printed nickel-based superalloys. *Quantum Beam Science* **2**, 13 (2018).

[143] Chen, X., Dejoie, C., Jiang, T., Ku, C.-S. & Tamura, N. Quantitative microstructural imaging by scanning laue x-ray micro-and nanodiffraction. *MRS bulletin* **41**, 445–453 (2016).

[144] Thomas, O., Labat, S., Cornelius, T. & Richard, M.-I. X-ray diffraction imaging of deformations in thin films and nano-objects. *Nanomaterials* **12**, 1363 (2022).

[145] Shapiro, D. *et al.* Biological imaging by soft x-ray diffraction microscopy. *Proceedings of the National Academy of Sciences* **102**, 15343–15346 (2005).

[146] Zhou, C. *et al.* Recent strategies to improve moisture stability in metal halide perovskites materials and devices. *Journal of Energy Chemistry* **65**, 219–235 (2022).

[147] Maghsoudy-Louyeh, S., Kropf, M. & Tittmann, B. Review of progress in atomic force microscopy. *The Open Neuroimaging Journal* **12** (2018).

[148] Franken, L. E., Grünewald, K., Boekema, E. J. & Stuart, M. C. A technical introduction to transmission electron microscopy for soft-matter: Imaging, possibilities, choices, and technical developments. *Small* **16**, 1906198 (2020).

[149] Kirchartz, T., Márquez, J. A., Stolterfoht, M. & Unold, T. Photoluminescence-based characterization of halide perovskites for photovoltaics. *Advanced energy materials* **10**, 1904134 (2020).

[150] Guthrey, H. & Moseley, J. A review and perspective on cathodoluminescence analysis of halide perovskites. *Advanced Energy Materials* **10**, 1903840 (2020).

[151] Wang, D. *et al.* Polarized emission from cspbx 3 perovskite quantum dots. *Nanoscale* **8**, 11565–11570 (2016).

[152] Lobet, M. *et al.* Efficiency enhancement of perovskite solar cells based on opal-like photonic crystals. *Optics Express* **27**, 32308–32322 (2019).

[153] Condon, J. J. & Ransom, S. M. *Essential radio astronomy*, vol. 2 (Princeton University Press, 2016).

[154] Wille, K. *The physics of particle accelerators: an introduction* (Clarendon Press, 2000).

[155] Wilson, E. *An introduction to particle accelerators* (Oxford University Press, 2001).

[156] Hecht, E. Alfred zajac, optics (1974).

[157] Geraldes, R. *et al.* The design of exactly-constrained x-ray mirror systems for sirius. *Proc. MEDSI'18* 173–178 (2018).

[158] Zilli, V. *et al.* Installation and commissioning of the exactly-constrained x-ray mirror systems for sirius/lnls (2020).

[159] Geraldes, R. *et al.* Granite benches for sirius x-ray optical systems. *Proc. MEDSI18* (2018).

[160] Lena, F. *et al.* Copper braid heat conductors for sirius cryogenic x-ray optics (2020).

[161] dos Santos, L. M. *et al.* The control system of the four-bounce crystal monochromators for sirius/lnls beamlines. In *submitted to 18th International Conference on Accelerator and Large Experimental Physics Control Systems Shanghai* (2021).

[162] Geraldes, R., Witvoet, G. & Vermeulen, J. The mechatronic architecture and design of the high-dynamic double-crystal monochromator for sirius light source. *Precision Engineering* **77**, 110–126 (2022).

[163] Neckel, I. T. *et al.* Development of a sticker sealed microfluidic device for in situ analytical measurements using synchrotron radiation. *Scientific Reports* **11**, 23671 (2021).

[164] Campanelli, R. *et al.* Large area hybrid detectors based on medipix3rx: commissioning and characterization at sirius beamlines. *Journal of Instrumentation* **18**, C02008 (2023).

[165] Takahashi, Y. *et al.* High-resolution and high-sensitivity x-ray ptychographic coherent diffraction imaging using the citius detector. *Journal of Synchrotron Radiation* **30** (2023).

[166] Grimes, M. *et al.* Bragg coherent diffraction imaging with the citius charge-integrating detector. *Journal of Applied Crystallography* **56** (2023).

[167] Moraes, M. *et al.* A control architecture proposal for sirius beamlines. In *Proc. of ICALEPCS*, vol. 17 (2017).

[168] Torquato, I. F. Coral: machine learning e matrizes de rotação aplicados a resolução de sistemas multivariados (2022).

[169] Março, P. H., Valderrama, P., Alexandrino, G. L., Poppi, R. J. & Tauler, R. Multivariate curve resolution with alternating least squares: description, operation and aplications. *Química Nova* **37**, 1525–1532 (2014).

[170] Ringnér, M. What is principal component analysis? *Nature biotechnology* **26**, 303–304 (2008).

Appendices

APPENDIX A

NON-SYNCHROTRON CHARACTERIZATION OF METAL HALIDE PEROVSKITES

In this chapter non-synchrotron characterizations of the films were performed to complement and support the observations with the synchrotron techniques described in the previous chapters. Moreover, some of the characterizations were performed in samples deposited over a glass and the newly explored mylar substrate, as an alternative for a cheap and easy access x-ray transparent substrate, with no absorption or phase contrast, for sample deposition as required for transmission techniques as ptychography.

The set of techniques used for this parallel characterization includes: tabletop x-ray diffraction (XRD) [69], atomic force microscopy (AFM) [147], scanning electron microscopy (SEM) [148], micro-photoluminescence (μ-PL) [149] and cathodoluminescence (CL) [150]. The choice of techniques was made to create a parallel between the synchrotron techniques to complement and corroborate with the previous results. X-ray diffraction allowed us to compare the values of lattice parameters in the small crystallites in the nanodiffraction with the average lattice parameter in each sample. Furthermore, XRD also gave insightful information about the phases formed in the new mylar substrate that was used in the synchrotron experiments, especially comparing the results with a more conventional and well-established glass substrate. μ-PL and cathodoluminescence are the complementary techniques to the XEOL, which probe the luminescence response excited in two different manners. While XEOL produces luminescence from the electron-hole recombination from the pairs created from the cascade after the excitation of a core electron, PL extracts the luminescence from exciting electrons near the bandgap with a much less energetic excitation photon (420 nm, 2.95200 eV) compared to the 7 or 10 keV used in XEOL experiments. PL comes in the sense of comparing the XEOL experiments with a well-established technique. Cathodoluminescence explores the luminescence excited with an electron beam and is as new as the XEOL in studies applied to hybrid perovskites. The main interest in using the XEOL and CL comes in the sense of studying new physics in these materials, and also comparing responses in different volumes of interactions since the X-ray beam is a bulk-sensitive probe since it crosses all the sample and excites the deepest layers of the materials, while the electron beam has a few nanometers penetration depth, probing only the near the surface emission channels of the materials. AFM and SEM are the ptychography's corresponding techniques. While ptychography, brings information about the general morphology of the sample probing all the depths of the material and integrates all this information in the projection direction, topographic AFM probes the 3-dimensional shape of the surface with a resolution that can reach values 1000 times better than the optical diffraction limit, but it is limited to the variation of the surface. As is the case of SEM it is surface sensitive technique that can create a high-resolution image depending on the magnification through the collection of secondary electrons emitted by the atoms, as it is scanned by the electron beam, as it is, SEM is mostly sensitive to the topography and surface composition. For that matter, a direct comparison is more intricate, and typically they work as complementary techniques. For that matter, we are going to use the SEM and AFM information only as support evidence, for some of our hypotheses, not as a validation of the ptychography results.

A.1 X-ray diffraction

X-ray diffraction data were obtained for the mylar substrate samples in the Bruker - D8 Advance Eco diffractometer, at the Brazilian Nanotechnology National Laboratory (LNNano) at the energy of 8 keV from the range of 5º to 55º, with a 0.04º resolution, which corresponds to the q interval of 0.35579 $Å^{-1}$ to 3.7670 $Å^{-1}$. The glass substrate data were obtained for the mylar substrate samples in the Shimadzu 6000 using Cu-K_α radiation, with 40 kV, 30 mA diffractometer, at the "Gleb Wataghin" Institute of Physics (IGFW) - UNICAMP at the same energy and angular range that the mylar samples with an angular resolution of 0.02º.

All 10, 20, 30, and 40% Cs-contents samples the XRD indicate the formation of the perovskite phase in both substrates, as it can be observed in the diffractogram in Figure A.1.a and .d for mylar and glass substrates. The major difference from the diffractograms is the fact that in the mylar samples, there is a strong and large peak at q = 1.8142 $Å^{-1}$ from form the Al frame use as support for the mylar. The second major difference is the presence of the PbI_2 at 20:38 only in the glass substrate, marked by the peak at q = 0.9058 $Å^{-1}$. As the Cs content increases the dominant effect is the shift to higher q in the perovskite peaks which is in agreement with the decrease of the lattice parameter as the Cs^+ substitutes the FA^+, which has a larger volume, contracting the crystal lattice [26]. In Table A.1 the peak positions are summarized from the 100 peaks of the cubic perovskite that are highlighted in Figures A.1.b and .e (pink region in Figures A.1.a and .d) showing the peak shift for a later q. The red and blue lines indicate the position of the 110 peak of 10:38 and 40:38 in mylar substrate, q = 0.9965 $Å^{-1}$ and q = 1.0218 $Å^{-1}$, respectively. This shift however occurs differently between the substrates. In mylar samples, this shift is actually caused by an inversion of two convoluted peaks, inverting the asymmetry of the resulting peak. As 10:38 is mostly symmetrical, 20:38, 30:38, and 40:38 have a asymmetric shape. 20:38 has a higher component in the lower q direction with a small component to the right, which increases as the Cs content increases

Position for 100 peak in the XRD data			
Substrate	Cs content (%)	q ($\AA^{-1}$)	d($\AA$)
Glass	10	1.0009	6.2775
Glass	20	1.0110	6.2148
Glass	30	1.0080	6.2333
Glass	40	1.0223	6.1461
Mylar	10	0.9965	6.3054
Mylar	20	0.9967	6.2681
Mylar	30	1.0024	6.2681
Mylar	40	1.0218	6.1491

Table A.1: Position for 100 peak in the XRD data

until it reaches 40:38 in which the far-right component gets more intense than the smaller-q one. These components also show a small displacement to larger q as the Cs content increases. In the glass samples, however, the peaks only translate to larger-q (lower d) as the Cs content increases, with only subtle variations in the asymmetry. The mylar samples have a smaller d for all compositions in comparison to the glass samples, as all the perovskite peaks in the diffractogram show a similar behavior.

Noticeably, the glass substrate shows the characteristic peaks of the tetragonal phase in the regions highlighted in blue in Figures A.1.c and .f with the increase of the Cs content, indicating the coexistence of the cubic and tetragonal phases for higher amounts of Cs in the sample in agreement with which was observed by Beal. et al. [127] The same behavior however could not be observed in mylar substrate, in which no indicatives of the tetragonal phase could be found. However, the splitting in the peaks at q = 2.2424 $\AA^{-1}$, q = 2.8400 $\AA^{-1}$ and q = 3.0122 $\AA^{-1}$, that Beal et. al. attribute as a indicate of the presence of the tetragonal phase also appears in the mylar samples. This splitting also appears in the 100 peak, much more prominently than the lost of symmetry observed in both of substrates of this work. In this referenced work, glass substrate was also used.

A.2 Atomic force microscopy

The Atomic Force Microscopy (AFM) methodology employed in this study involved conducting measurements in contact mode under controlled low humidity conditions (RH < 20%) using the NanoSurf AFM system. In this approach, a specialized environmental chamber is utilized to maintain the desired low humidity levels. The AFM tip, attached to a cantilever, engages with the sample surface in contact mode. The controlled environment plays a pivotal role in modulating adhesive forces between the AFM tip and the sample. Specifically,

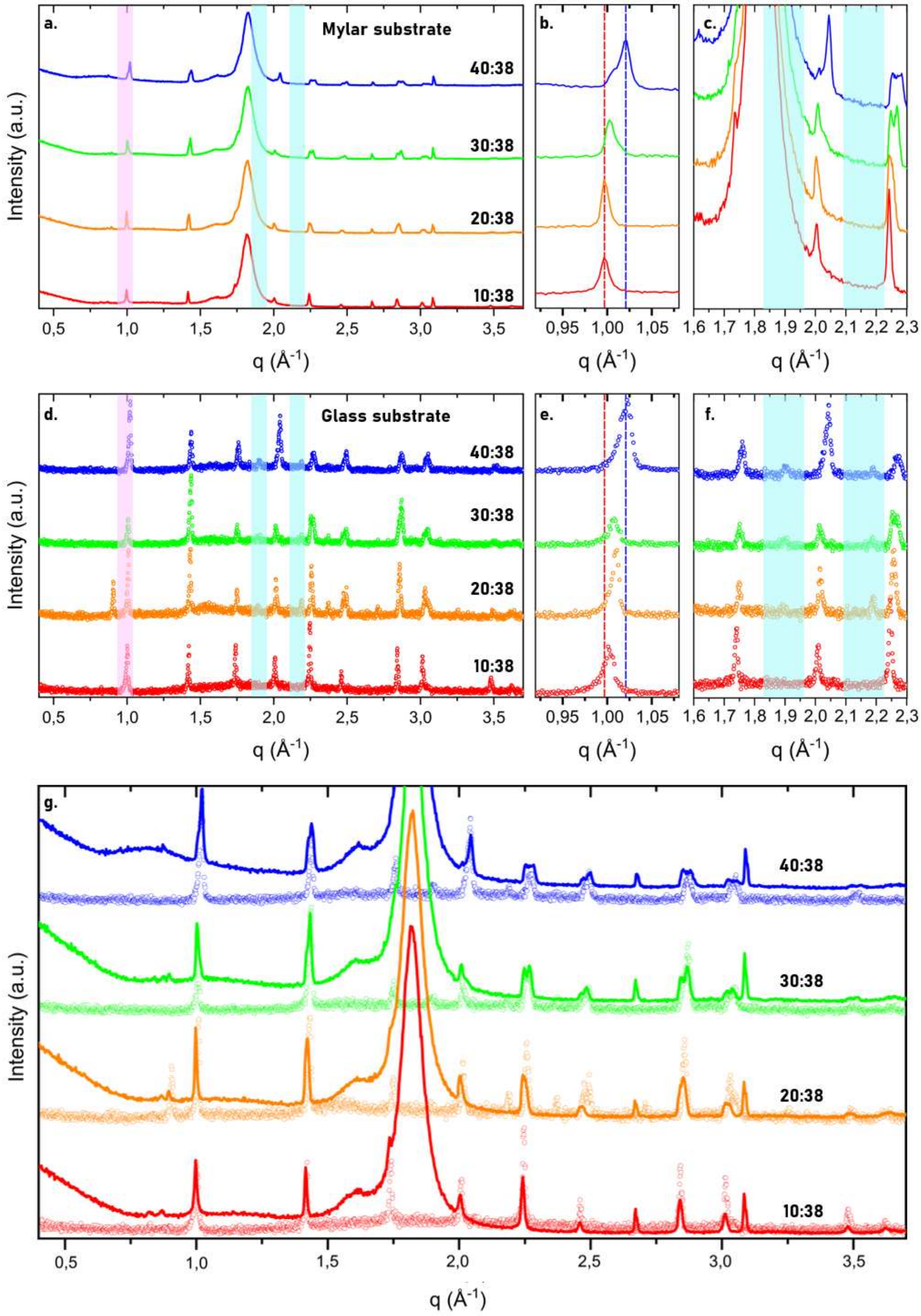

Figure A.1: XRD diffraction from for 10:38, 20:38, 30:38 and 40:38 samples.(a) and (d) are the full diffractograms in mylar and glass substrates. (b) and (e) are zoomed regions of the diffractogram around the (100) peak (pink region in the diffractogram). Blue and red lines correspond to 10:38 and 40:38 peak positions in mylar substrate, q = 0.9965 $Å^{-1}$ and q = 1.0218 $Å^{-1}$. (c) and (f) are zoomed in the region between 1.6 $Å^{-1}$ and 2.3 $Å^{-1}$, with light-blue areas indicating the position where the peaks indicating the presence of a tetragonal phase appears. (g) are the superposition of diffractograms (a) and (d) saturating the Al frame peak for better comparison of the substrates.

diminished moisture content mitigates van der Waals and capillary forces, minimizing tip-sample adhesion.

Examination of Atomic Force Microscopy (AFM) results shows the strikingly similar topographical features among four compositions with an average grain size of 150 nm become apparent. The AFM images of Samples 10:38, 20:38, 30:38, and 40:38 reveal a consistent pattern of nanoscale structures, suggesting a shared underlying synthesis and formation process, as observed in Figure A.2. All images were acquired in the transition region from the hill to valley regions with a 5×5 μm^2 area, with 10 nm resolution, except sample 10:38 which was measured in a smaller area of 2.5×2.5 μm^2 with the same resolution. No grain size distribution variation from different regions of the scans was observed. The uniformity in grain size across all samples underscores the precision and reproducibility of the deposition technique employed, despite the large variation in the Cs content. Average grain size is slightly smaller in 40:38 sample, 135 nm (Figure A.2.d and .h).

A few line artifacts can be observed in the AFM images, which are mostly attributed to the non-rigid mylar substrate and possible humidity in the sample environment during the measurement, since perovskite materials are known to be hygroscopic, meaning they readily absorb moisture from the surrounding atmosphere. In this scenario, the interaction between the AFM probe and the perovskite film on a non-rigid substrate can be complex. The softness or deformability of the substrate may affect the force exerted by the AFM probe during scanning, potentially leading to variations in the measured topography. Furthermore, the presence of adsorbed moisture on the perovskite surface can influence the adhesion forces between the probe and the sample, affecting the accuracy of the acquired images.

A.3 Electron microscopy

SEM images were obtained using a HELIOS 5 PFIB CXE DUALBEAM microscope at the accelerating voltage of 2.0 kV with a small current of 0.40 nA, at the magnifications of 25000 x and 50000 x. The electron micrograph of the samples are presented in Figure A.3. Before acquisitions, tests were made and no beam damage was observed until 3 consecutive images were acquired in the same positions. No charging artifacts were observed. All samples showed very similar features in the surface morphology, with grain sizes around 120 nm in diameter. Variation in the grain morphology could not be observed correlated with the microscale topology of the wrinkles in mylar substrate. All compositions have similar grain size distribution, with no correlation with Cs content. No anisotropic structures were present, other than the corrugations. The same compositions deposited on the glass substrate have different SEM morphologies compared to mylar ones, as shown in Figure A.4, with the average grain sizes growing as it is on the top of the hills in the morphologies reaching the average size of 650 nm, with a distribution in which some of the largest grains are larger than

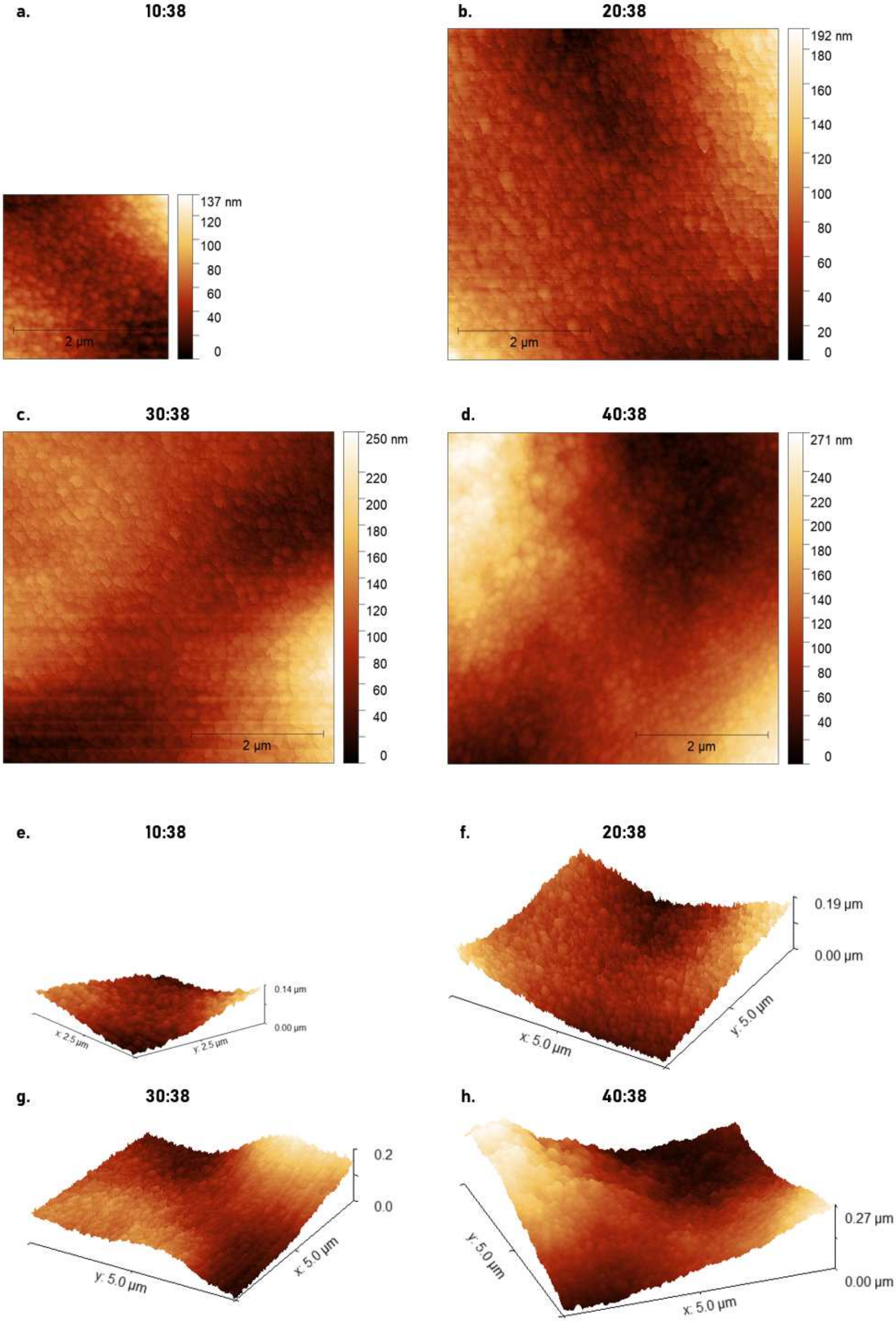

Figure A.2: AFM topographies. AFM maps presented for samples (a) 10:38, (b) 20:38, (c) 30:38, (d) 40:38, in mylar substrate. (e), (f), (g) and (g) are the respective 3D visualizations of the topographies. Maps for 20:38, 30:38 and 40:38 are of $5 \times 5 \mu m^2$ with 10 nm pixel size. Maps for 10:38 are of $2.5 \times 2.5 \mu m^2$ with 10 nm pixel size.

800 nm. In the valley regions of the morphology, the grain size is around 150 nm in all four compositions, slightly larger than the values observed for the mylar substrate.

These variations in the grain sizes between the substrates are attributed to the annealing part of the deposition process. As the 15 × 15 mm^2 aluminum frame over which the mylar film is fixed for sample deposition has a 10 mm in diameter hole in its center most of the heat transfer to the sample in the center region of the mylar substrate in reduced due to the small cross-section of the 6 μm thick mylar substrate (Figure A.5). Summed up the annealing process is performed not in vacuum (H_2O and O_2 are kept below 10 ppm), and the convection effects are not negligible in this case, the thermal homogeneity throughout the whole film is not achieved and the temperature ramp and final temperatures in the depositions are different between the substrates. This implies impaired annealing in the mylar films, ultimately, causing a poor crystallization in the sample, especially in the hill regions, where the annealing process not only favors the formation of the wrinkled morphology [23], but also can improve the crystallinity of the sample resulting in larger grain sizes, as one can observe in the glass films.

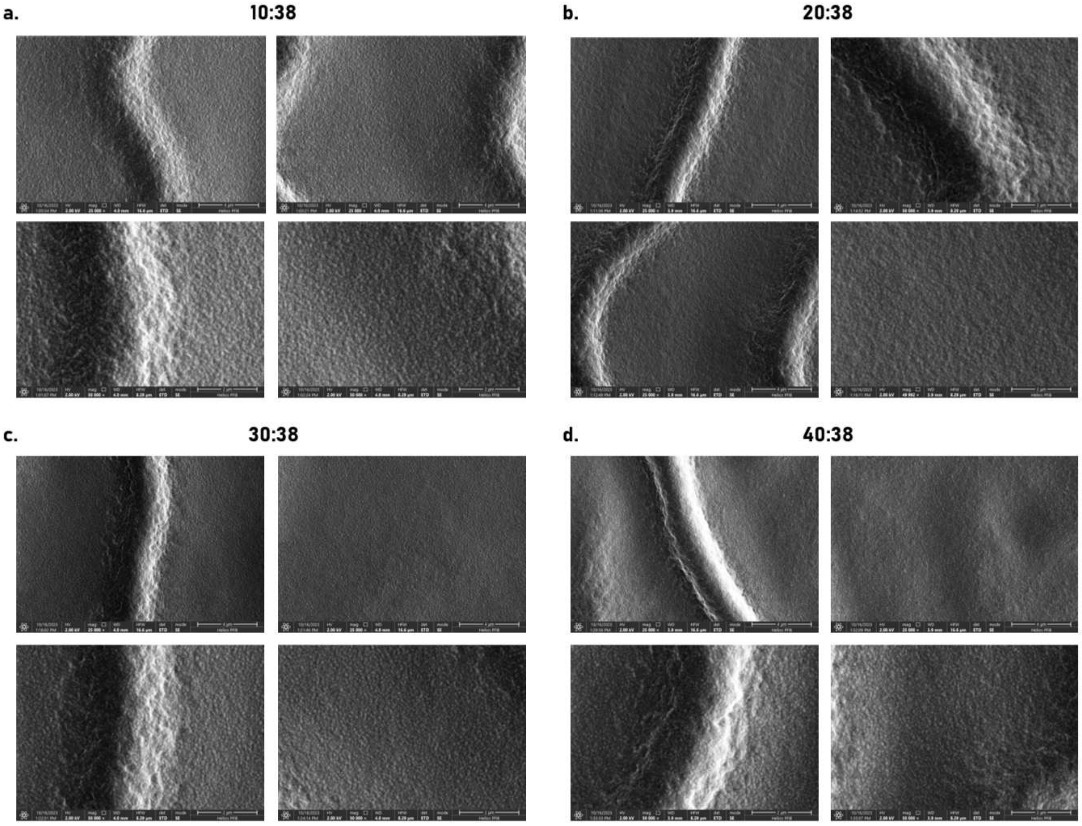

Figure A.3: SEM morphologies. SEM maps presented for samples (a) 10:38, (b) 20:38, (c) 30:38, (d) 40:38, in mylar substrate. In hill and valley regions of the morphology. Two images on top for each sample have a magnification of 25000 x, while two images on the bottom have a magnification of 50000 x.

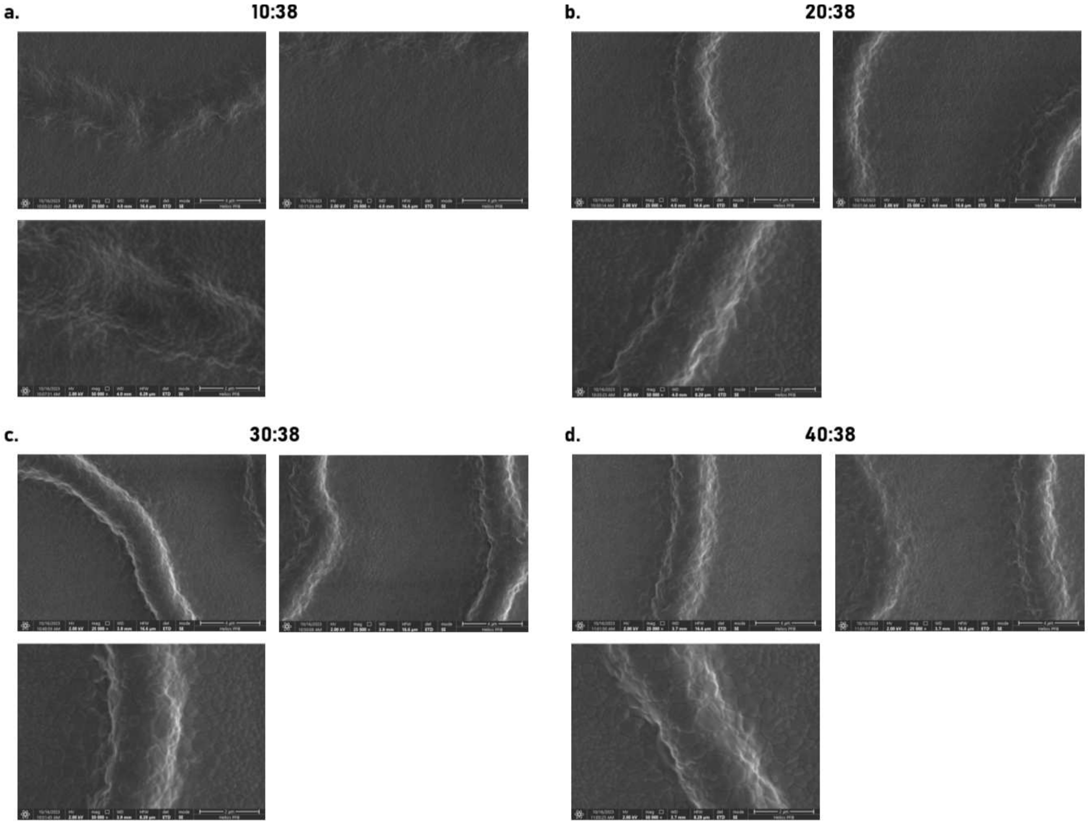

Figure A.4: SEM morphologies. SEM maps presented for samples (a) 10:38, (b) 20:38, (c) 30:38, (d) 40:38, in glass substrate. In hill and valley regions of the morphology. Two images on top for each sample have a magnification of 25000 x, while the image on the bottom has magnification of 50000 x.

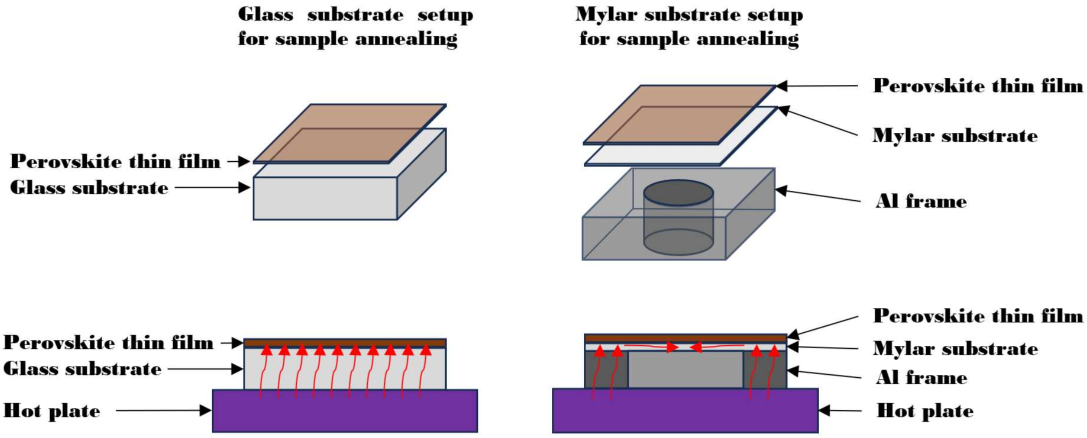

Figure A.5: Annealing processes in different substrates.

Position of the maximum of the luminescence emission			
Substrate	Cs content (%)	Mean emission position (eV)	Dispersion size (eV)
Glass	10	1.627	0.071
Glass	20	1.671	0.099
Glass	30	1.670	0.051
Glass	40	1.721	0.088
Mylar	10	1.631	0.072
Mylar	20	1.671	0.113
Mylar	30	1.702	0.150
Mylar	40	1.700	0.121

Table A.2: Position of the maximum of the luminescence emission

A.4 μ-Photoluminescence

To support and compare the XEOL observations PL measurements were performed via an excitation with a 420 nm laser in all X:38 compositions. The 1 μm optical probe scanned the sample with steps of 1 μm crossing in a linear path the morphology of the sample. The μ-PL data were acquired at the Brazilian Nanotechnology Laboratory (LNNano), which is part of the Brazilian Center for Research in Energy and Materials (CNPEM). The PL was obtained using a confocal Raman spectrometer Horiba XploRA plus. The studied regions of the sample were selected using optical microscopy coupled to the equipment, and then PL measurements were obtained in different regions with a beam size of around 1 μm. The excitation source was a 420 nm laser in circular polarization [151] with a minimum power of 0.1% and a minimum integration time of 1 ms with an average of 5 spectra per point. The emission range studied extends from 550 nm up to 850 nm.

The same behavior previously described in XEOL (Figure 5.4) was reproduced when the sample was scanned with a conventional μ-PL probe and agreed with measurements performed in both mylar and glass. It was also verified that in both substrates, the correlation between the wrinkled morphology region and the shifts in the PL emission still prevails. The maps of the regions correlated with these spectra are summarized in Figure **??**. One can see in Table **??** that the mean emission energy in both substrates are very similar, for 10:38 and 20:38, with 0.004 eV of difference or less, while in 30:38 and 40:38, the differences are of 0.032 eV and 0.021 eV respectively. And, except from 10:38, which has a very similar dispersion in both substrates, the mylar substrates seem to enlarge the difference the energy of emission between different points in the sample with a minimum dispersion of 0.113 eV for 20:38, 30:38, and 40:38 samples, in comparison with the respective samples in glass that has a maximum dispersion of 0.099 eV. This evidences that with respect to the optical response, the mylar substrate is less favorable for the homogeneity of the films.

The 40:38 sample in glass has 4 points out of the main cluster, with a smaller bandgap with emission around 1.30 eV. They were not included in the estimation of the dispersion size of the points. This is attributed to segregation in the sample since, that specific sample was measured three days later than the others.

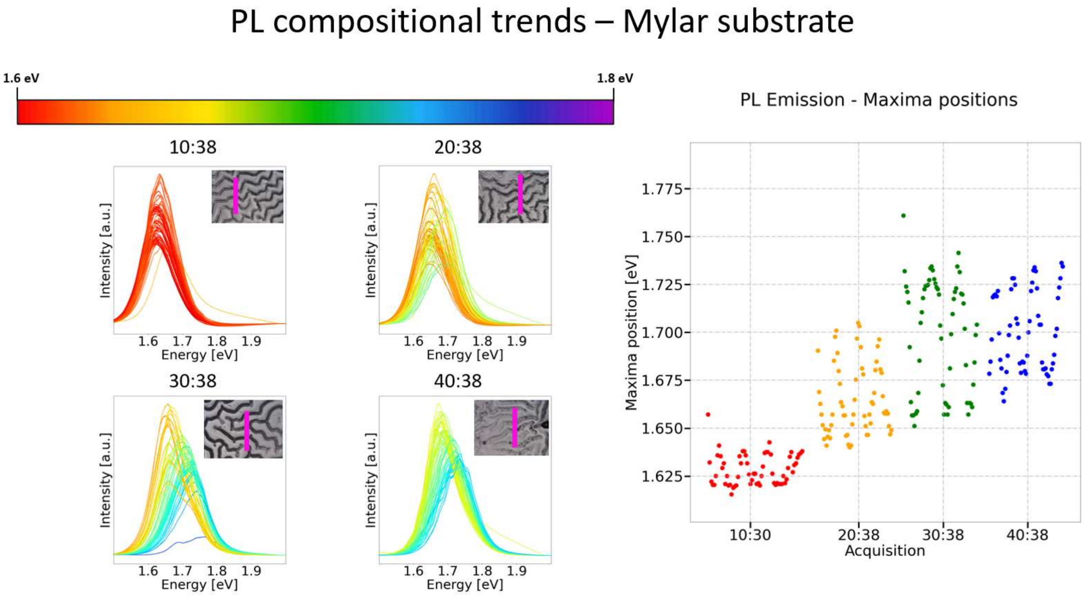

Figure A.6: PL spectra acquired for samples in mylar substrate. Each spectrum is acquired during a 1 ms integration time for each 1 μm step position on the sample. The color of the line for the plot is chosen according to the position of its maxima. Color code is shown in the bar over the spectra. The position of the maxima is scattered for each sample in the plot on the right. Points in red are with respect to sample 10:38, orange 20:38, green, 30:38, and blue 40:38. Inserts on the graphs show the wrinkled morphology with a pink-like indicating the path of the probe.

A.5 Cathodoluminescence

Cathodoluminescence (CL) mapping experiments were performed at HELIOS 5 PFIB CXE DUALBEAM microscope, and a focused electron beam was employed at an accelerating voltage of 10 kV and a current of 100 pA to probe the optical and structural characteristics of the sample. The utilization of a scanning electron microscope (SEM) equipped with a cathodoluminescence detection system facilitated high-resolution imaging. The electron beam systematically scanned the sample surface with a step size of 1 μm crossing the corrugated morphology of the sample, with an integration time of 0.5 s. This pixel size represents the spatial resolution at which individual data points were collected during the mapping process, however, it averages the majority over the 5 nm diameter area of the electron probe size. This procedure was based on the guidelines for CL measurements in perovskite summarized from literature [150] considering that: 1) incident e-beam current should be minimized, 2) accelerating voltage should be minimized, 3)acquisitions time, meaning pixel dwell time, should be minimized. As in the sense of methodology developed for the XEOL maps, the large step in the map was also implemented in order to reduce the damage effect from the

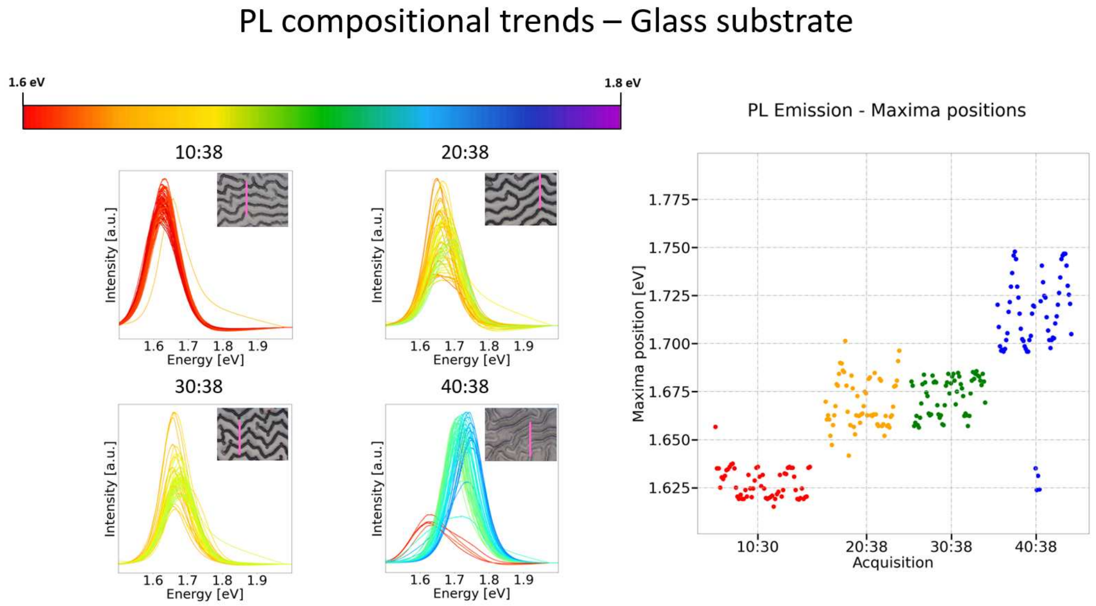

Figure A.7: PL spectra acquired for samples in a glass substrate. Each spectrum is acquired during a 1 ms integration time for each 1 μm step position on the sample. The color of the line for the plot is chosen according to the position of its maxima. Color code is shown in the bar over the spectra. The position of the maxima is scattered for each sample in the plot on the right. Points in red are with respect to sample 10:38, orange 20:38, green, 30:38, and blue 40:38. Inserts on the graphs show the wrinkled morphology with a pink-like indicating the path of the probe.

neighboring irradiated regions. A fast-tracking of the damaged region of a single point CL spectra indicated that steps smaller than 500 nm caused a considerable change in the next point of acquisition, mostly in intensity.

The micrometer resolution CL maps (Figure A.8 revealed distinct luminescent patterns correlated with the material's microstructure. Regions with varying halide compositions exhibited diverse emission spectra, shedding light on the spatial distribution of different amounts of matter within the perovskite film, corroborating the results observed in PL and XEOL experiments. The variations in the position of the emission in the cathodoluminescence signal (Figure A.9) in were found to be directly related to the local chemical composition, specifically the corrugation morphology of all four samples, associated to the ratio of halides, as presented in Chapter 5.

A closer look in the correlation between the morphology simultaneously acquired by SEM indicates that regions with smaller energy emissions extend to areas larger than the corrugation size as observed in the superposition of SEM and the emission energy maps in Figure A.8. The smaller bandgap are extended from 3 to 4 μm apart from the main variation (largest derivative in the brillance of SEM images) in the morphology

As in agreement with the observed in PL and XEOL experiments, and corroborating with XRF Br:Pb ratios, the hill regions of the wrinkled morphology have a CL redshifted compared to the valleys. The average value for the emissions are: 1.722 eV, 1.749 eV, 1.733 eV, 1.749 eV, with standard deviations of 0.039 eV, 0.064 eV, 0.039 eV, 0.045 eV, for samples 10:38, 20:38, 30:38 and 40:48 respectively. For these values the intensity of each point was not take into account. The mean value of the position of the emission follows the trend of a blue shift as the total content of Cs increases, except for the 20:38 sample, which has a larger simple mean emission value than the other samples. However, if the emission is pondered by the intensity of the average values are: 1.707 eV, 1.714 eV, 1.716 eV, and 1.733 eV, with standard deviations of 0.037 eV, 0.055 eV, 0.034 eV, 0.039 eV.

The difference from the different averages indicated that despite a considerably large variation in the emission of some compositions such as showed by 20:38, the average response of the sample is dominated by the Cs content, and the morphology of the samples plays an important role in the regularization of the Cs effect, since the wrinkled morphology, that affects preponderantly the intensity of the emission position and its intensity.

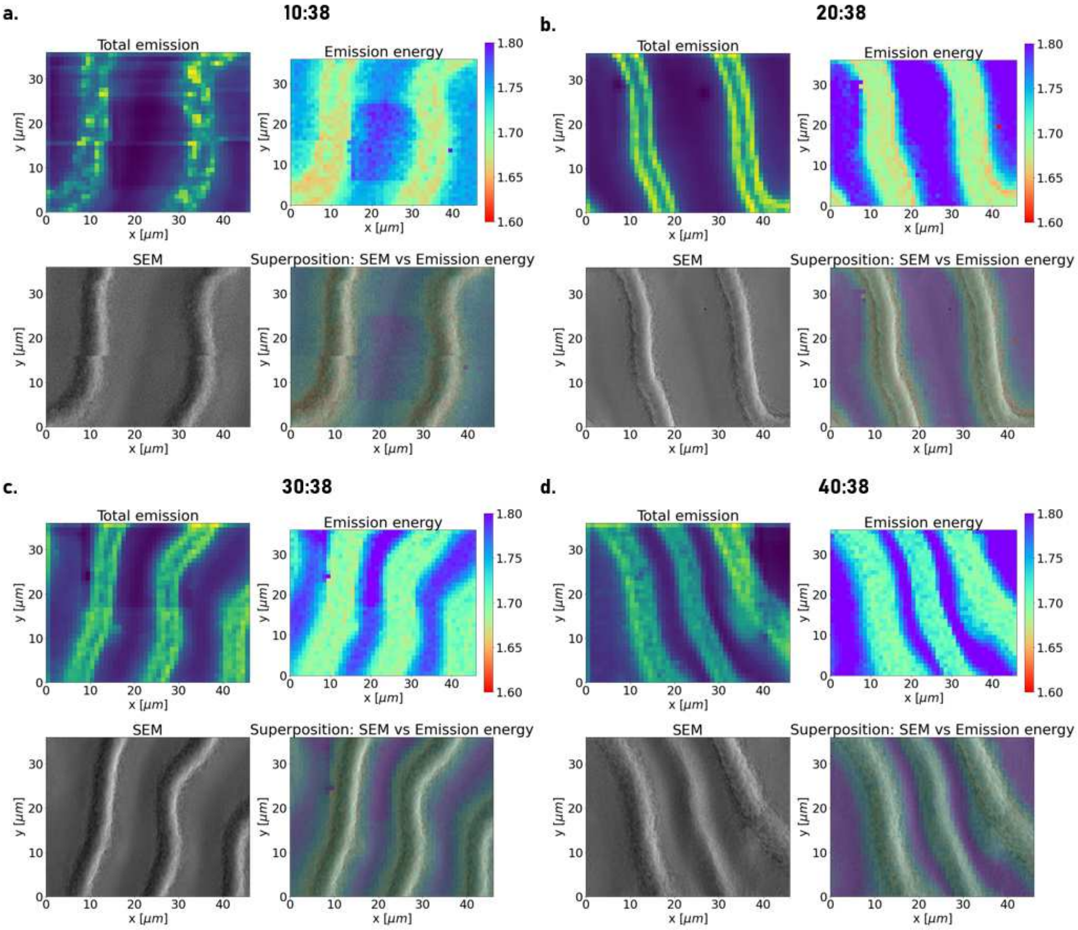

Figure A.8: CL mapping. CL maps presented for samples (a) 10:38, (b) 20:38, (c) 30:38, (d) 40:38, in mylar substrate. For each sample is presented the total luminescence emission and the position in energy of the maxima for each scanned point in the sample (Emission energy). A simultaneous SEM image is also presented. The superposition of the SEM and Emission energy aids in visualizing the correlative effect of the morphology and luminescence, and the spatial extension of its intricate behavior.

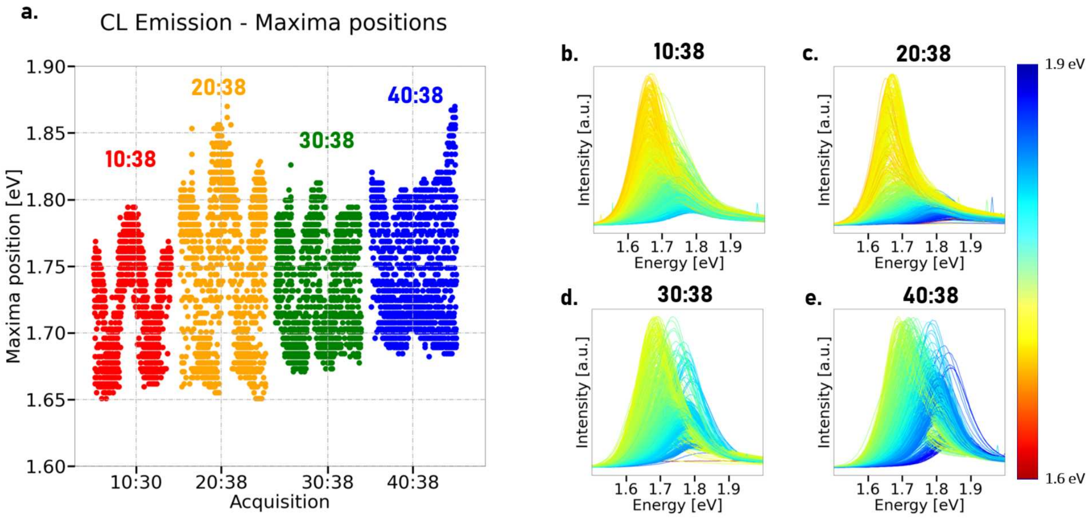

Figure A.9: CL spectra during mapping of Figure A.8 acquired for samples in mylar substrate. Each spectrum is acquired during a 0.5 s integration time for each 1 μm step position on the sample. The color of the line for the plot is chosen according to the position of its maxima. Color code is shown in the bar over the spectra. The position of the maxima is scattered for each sample in the plot on the right. Points in red are with respect to sample 10:38, orange 20:38, green, 30:38, and blue 40:38. Inserts on the graphs show the wrinkled morphology with a pink-like indicating the path of the probe.

A.6 PL, CL, and XEOL comparisons

Cathodoluminescence (CL) in semiconductors arises from the radiative recombination of excess electrons and holes induced by an electron beam (e-beam). The luminescent processes observed in CL measurements fundamentally mirror the process in PL and XEOL measurements. In all three cases, excess carriers undergo drift, diffusion, and recombination through nonradiative and radiative mechanisms, whether stimulated by the e-beam (CL) or by (visible or x-ray) photons means (PL or XEOL). Nevertheless, disparities in the excess-carrier generation between these methods yield distinct information. In CL, the excited material's volume is often considerably smaller than in PL, granting CL higher spatial resolution. However, achieving a satisfactory CL signal frequently demands substantially elevated generation rates and injection levels. [150]

The penetration depths of different types of radiation, such as visible light, 10 kV electrons, and X-rays, significantly impact experimental outcomes in techniques like XEOL (X-ray Excited Optical Luminescence), CL (Cathodoluminescence), and PL (Photoluminescence). Understanding these penetration depths is crucial for accurate interpretation and comparison of results obtained through these methods.

Visible light has a limited penetration depth of less than 100 nanometers in hybrid perovskites. [152] The shallow penetration makes it suitable for surface-level analyses, capturing responses primarily from the material's outer layer. In XEOL, CL, and PL experiments, visible light excitation may provide information predominantly from the surface, influencing the observed luminescent behavior. The 10 kV electrons exhibit greater penetration depth, ranging in the first 200 nanometers. [150] This increased penetration allows for probing deeper into the material, reaching subsurface layers. In CL experiments, the use of 10 kV electrons enables the exploration of subsurface structures, offering insights beyond the material's immediate surface. X-rays possess much larger penetration depths, extending into micrometer ranges, in this case, the full cross-section of the perovskite film. The capability of X-rays to penetrate deeper layers makes XEOL an effective technique for probing bulk properties of materials. In XEOL experiments, X-rays can excite luminescence throughout a more extensive volume, capturing information from deeper within the material. In fact the calculated values for the absorption for 10 keV photons for 500 nm thick perovskite film with this composition are less than 2%. (Appendix G).

A.7 General remarks

In this complementary study, the non-synchrotron characterizations of metal halide perovskite (MHP) films were explored, providing crucial insights to complement and support observations made using synchrotron techniques. The use of mylar as an alternative substrate for X-ray transparent applications, such as ptychography, was investigated due to its cost-effectiveness and accessibility.

The X-ray diffraction analysis uncovered essential details about the perovskite phases in both mylar and glass substrates, revealing intriguing differences in peak positions and phase coexistence. AFM provided high-resolution topographical information, showcasing consistent nanoscale structures across different compositions and suggesting a uniform synthesis process. SEM images, obtained with a focus on ptychography support, revealed variations in grain sizes between mylar and glass substrates, attributed to differences in the annealing process and thermal homogeneity.

The μ-PL measurements, serving as a comparison with X-ray excited optical luminescence (XEOL), highlighted the influence of substrate choice on the homogeneity of films. Notably, mylar substrates exhibited a less favorable outcome for the homogeneity of films compared to glass. Similarly, CL mapping experiments, performed with a focus on spatial distribution, provided insights into luminescent patterns correlated with microstructure, emphasizing the impact of Cs content and morphology on emission characteristics.

A noteworthy aspect was the comparison of PL, CL, and XEOL methods, each offering distinct information based on their penetration depths. While visible light in PL primarily captured surface-level responses, 10 kV electrons in CL delved deeper into subsurface structures. XEOL, utilizing X-rays with larger penetration depths, proved effective in probing bulk properties, providing a comprehensive understanding of the material's luminescent behavior across different volumes.

APPENDIX B

SCIENTIFIC AND TECHNICAL PRODUCTION DURING DOCTORATE YEARS

B.1 Published papers

[1]

1. **da Silva, F. M.**, Szostak, R., Teixeira, V. C., Germino, J. C., Soares, M. M., Nogueira, A. F., & Tolentino, H. C. (2023). *Disentangling X-Ray and Sunlight Irradiation Effects Under a Controllable Atmosphere in Metal Halide Perovskites.* Solar RRL, 7(1), 2200898.

2. **da Silva, F. M. C.**, Moreno, G. B. Z. L., Geraldes, R. R., Lordano, S. A., Pinto, A. C., Kofukuda, L. M., ... & Tolentino, H. C. N. (2022, December). *An innovative optical element for X-ray beam aperture, monitoring, and diagnostic at the CARNAÚBA beamline at SIRIUS/LNLS.* In Journal of Physics: Conference Series (Vol. 2380, No. 1, p. 012062). IOP Publishing.

3. Verônica C. Teixeira, Joelson C. Silva, **Francisco C. M. Silva**, Rodrigo Szostak, Maria Gabriella D. Guaita, Leonardo M. Kofukuda, Antonio C. Piccino Neto, Anna P. S. Sotero, Itamar T. Neckel, Carlos A. Pérez, Douglas Galante, & Hélio C. N. Tolentino *X-ray excited optical luminescence at Carnauba, the Sirius X-ray nanoprobe beamline.* Submitted at: The Optical Materials X

4. Guaita, M. G., Szostak, R., **da Silva, F. M.**, de Morais, A., Moral, R. F., Kodalle, T., ... & Nogueira, A. F. (2023). *Influence of Methylammonium Chloride on Wide-Bandgap Halide Perovskites Films for Solar Cells.* Advanced Functional Materials, 2307104.

5. Tolentino, H. C., Geraldes, R. R., **da Silva, F. M.**, Guaita, M. G. D., Camarda, C. M., Szostak, R., ... & Westfahl Jr, H. (2023). *The CARNAÚBA X-ray nanospectroscopy beamline at the Sirius-LNLS synchrotron light source: developments, commissioning, and*

---

[1] The first papers on the list accounts for the publications as first author. The following are listed in order of year of publication, from the newest to the earliest one.

first science at the TARUMÃ station. Journal of Electron Spectroscopy and Related Phenomena, 147340.

6. de Oliveira, R., Guallichico, L. A., Policarpo, E., Cadore, A. R., Freitas, R. O., **da Silva, F. M.**, ... & Barcelos, I. D. (2022). *High throughput investigation of an emergent and naturally abundant 2D material: Clinochlore.* Applied Surface Science, 599, 153959.
7. Neckel, I. T., **da Silva, F. M.**, Guedes, E. B., Dias, C. S., Soares, M. M., Costa, C. A., ... & Tolentino, H. C. (2022). *Unveiling Center-Type Topological Defects on Rosettes of Lead Zirconate Titanate Associated to Oxygen Vacancies.* Annalen der Physik, 534(2), 2100219.
8. Luiz, S. A., Bueno, C. S., **Silva, F. M.**, Celestre, R., Meyer, B. C., Oliveira, R., ... & Dias, C. S. (2022, October). *Diagnostics of KB mirrors misalignment using Zernike rectangular polynomials and neural networks.* In Advances in X-Ray/EUV Optics and Components XVII (Vol. 12240, pp. 11-19). SPIE.
9. Lena, F. R., Bueno, C. S. N. C., Cardoso, F. H., Donatti, M. M., Neto, J. B., Geraldes, R. R., ... & **Silva, F. M. C.**, Szostak, R. (2022, December). *Commissioning of the cryogenic sample environment for the TARUMÃ station at the CARNAÚBA beamline at Sirius/LNLS.* In Journal of Physics: Conference Series (Vol. 2380, No. 1, p. 012108). IOP Publishing.
10. Baraldi, G. L., Dias, C. S., **Silva, F. M.**, Tolentino, H. C., & Miqueles, E. X. (2020). *Fast reconstruction tools for ptychography at Sirius, the fourth-generation Brazilian synchrotron.* Journal of Applied Crystallography, 53(6), 1550-1558.

B.2 Submitted papers

1. **da Silva, F. M.**, Szostak, R., Guaita, M. G., Teixeira, V. C., Nogueira, A. F., & Tolentino, H. C. *X-ray dose effects and strategies to mitigate beam damage in metal halide perovskites under high brilliance X-ray photon source.* Submitted at: Energy Materials
2. *L*ara Maldanis, David Fernandez-Remolar, Laurence Lemelle, Manuel Guizar-Sicairos, Mirko Holler, **Francisco M. C. da Silva**, Valérie Magnin, Michel Mermoux, Alexandre Simionovici, *Unveiling challenging microbial fossil biosignatures from Rio Tinto with micro-to-nanoscale chemical and ultrastructural imaging*. Submitted at: Astrobiology.

B.3 Awards

1. Award: **Young Scientist Award** *(Melbourne, Australia - 2023)* - Congress: Twenty-Sixth Congress and General Assembly of the International Union of Crystallography (`https://iucr2023.org/`). Organizer: IUCr - International Union of Crystallography

   Title: **Multispectral studies of metal halide perovskites**. Oral presentation.

2. Award: **Melhor poster de Doutorado** *(Campinas, Brasil - 2021)* - Congress: CEC: Congresso dos estudantes do CNPEM. Organizer: CNPEM - The Brazilian Center for Research in Energy and Materials

   Title: **Correlations among optical, structural, and morphological properties of hybrid perovskites by x-ray nanoscopy with synchrotron light**. Poster and flashtalk presentation.

APPENDIX C

SYNCHROTRON TECHNOLOGY

The generation of light through the acceleration of particles is a fascinating interplay of fundamental physics and cutting-edge technology. At the heart of this process lies the use of particle accelerators, where charged particles, typically electrons, are accelerated to relativistic speeds. As these high-energy electrons traverse curved trajectories within strong magnetic fields, they emit electromagnetic radiation known as synchrotron radiation. This phenomenon finds extensive applications in various scientific disciplines, from fundamental research in particle physics to advanced imaging techniques in medicine.

C.1 X-ray generation

The generation of electromagnetic radiation through the acceleration of charged particles constitutes a fundamental aspect of classical electrodynamics. This intricate physical phenomenon is comprehensively described by Maxwell's equations, which form the foundational framework for understanding the behavior of electric and magnetic fields in the presence of dynamic charge distributions.

Maxwell's equations, expressed in their differential form, encapsulate the principles of electromagnetic field theory. Gauss's law for electricity ($\nabla \cdot \mathbf{E} = \frac{\rho}{\varepsilon_0}$) establishes the relationship between electric fields and charge distributions, while Gauss's law for magnetism ($\nabla \cdot \mathbf{B} = 0$) dictates that magnetic field lines do not have sources or sinks. Faraday's law of electromagnetic induction ($\nabla \times \mathbf{E} = -\frac{\partial \mathbf{B}}{\partial t}$) reveals how a changing magnetic field induces an electric field, while Ampère's law with Maxwell's addition ($\nabla \times \mathbf{B} = \mu_0 \mathbf{J} + \mu_0 \varepsilon_0 \frac{\partial \mathbf{E}}{\partial t}$) highlights the interplay between changing electric fields and the generation of magnetic fields.

In the context of accelerating charged particles, the Larmor formula emerges as a pivotal expression that quantifies the power radiated (P) by a charged particle undergoing acceleration: [81]

$$P = \frac{q^2 a^2}{6\pi \varepsilon_0 c^3}$$

This formula elucidates the direct proportionality between the square of the charge (q) and the square of the acceleration (a), emphasizing the significance of acceleration in the radiation process. Here, ε_0 represents the vacuum permittivity, and c is the speed of light.

The Lorentz force equation, $\mathbf{F} = q(\mathbf{E}+\mathbf{v}\times\mathbf{B})$, is a cornerstone in describing the motion of charged particles in electromagnetic fields. This equation delineates how a charged particle experiences a force ($\mathbf{F}$) due to both electric ($\mathbf{E}$) and magnetic ($\mathbf{B}$) fields, along with its velocity ($\mathbf{v}$). As the particle accelerates, it undergoes a radiation reaction force ($\mathbf{F}_{\text{rad}}$), opposing its acceleration [153]:

$$\mathbf{F}_{\text{rad}} = -\frac{2q^2}{3c^3}\frac{\mathbf{a}_{\parallel} + \mathbf{v}\times(\mathbf{a}_{\parallel}\times\mathbf{v})}{(1-\mathbf{v}\cdot\mathbf{v}/c^2)^2}$$

This radiation reaction force encapsulates the intricate dynamics of charged particles experiencing acceleration, leading to the emission of radiation.

The power spectrum ($P(\omega)$) for non-relativistic particles provides further insights into the radiation process. This expression is influenced by the angle (θ) between the acceleration vector and the direction of observation, as well as the particle's velocity (β) [153]:

$$P(\omega) = \frac{q^2 a^2}{4\pi\varepsilon_0 c^3}\frac{\sin^2(\theta)}{(1-\beta\cos\theta)^5}$$

Here, the frequency-dependent power of the emitted radiation is clearly delineated, emphasizing the directional and velocity-dependent nature of the emitted radiation.

For relativistic particles, modifications are introduced to the power spectrum to account for relativistic effects. The Lorentz factor (γ) and critical frequency (ω_c) become crucial in this context [153] [154]:

$$P(\omega) = \frac{q^2 a^2}{4\pi\varepsilon_0 c^3}\frac{1}{\omega}\left[\frac{K_{2/3}^2(\xi)}{K_{1/3}^2(\xi)} + \frac{1}{\gamma^2}\left(\frac{1}{2}-\frac{1}{\xi}\right)^2\right]$$

In this expression, $K_{2/3}$ and $K_{1/3}$ represent modified Bessel functions, and $\xi = \omega/\omega_c$. These modifications underscore the relativistic effects on the emitted radiation spectrum, which are essential for the description of the synchrotron emission.

C.2 Electron harnessing and accumulation in synchrotron light sources

Within the domain of particle accelerators, the synchrotron particle accelerator stands as a quintessential apparatus, orchestrating the intricate manipulation of charged particles to yield highly collimated and energetic particle beams. In this section, the components of a synchrotron accelerator are described, encompassing the electron source, the booster ring, and the storage ring, (Figure C.1) while expounding upon the pivotal role played by magnetic lenses, the requisite tolerance factors, and key machine parameters.

LINAC (Linear accelerator)

The electron source and linear accelerator (LINAC) represent the initial stages in the orchestration of a synchrotron particle accelerator, serving as the foundational components responsible for generating and propelling electron beams into subsequent acceleration and storage phases. The electron source, typically a cathode, initiates the process by emitting electrons under the influence of an applied electric field. This initial electron population undergoes extraction, forming an electron beam with defined energy and current. Key parameters influencing the electron source operation include the cathode material, emission current, and energy spread of emitted electrons. Achieving a stable, high-quality electron beam at this stage is pivotal for downstream success in the accelerator complex.

Following extraction, the electron beam enters the LINAC, a linear array of radiofrequency (RF) cavities designed to sequentially accelerate the electrons to relativistic speeds. The RF cavities apply pulsed electric fields that synchronize with the electron bunch, imparting energy through each acceleration stage. Operational parameters such as RF frequency, pulse duration, and accelerating gradient are meticulously controlled to optimize the LINAC's performance.

The LINAC parameters significantly impact the final characteristics of the electron beam injected into subsequent stages. High accelerating gradients and precise control of RF parameters contribute to minimizing energy spread and emittance, crucial factors for achieving high-quality beams. The LINAC ensures that the electron beam reaches the desired energy before entering subsequent circular accelerators, setting the stage for synchrotron radiation production.

BOOSTER RING

The booster ring stands as a crucial component in the intricate symphony of a synchrotron particle accelerator. Functioning as an intermediate stage between the electron source and the storage ring, its primary role involves exponentially increasing the kinetic energy of extracted electrons. This enhancement ensures that, upon injection into the subsequent storage ring, the electron beam attains the requisite relativistic speeds for optimal synchrotron radiation generation.

Key parameters in the operation of the booster ring include the radiofrequency voltage (V_{RF}) applied to the electrons and the phase offset (ϕ). Maintaining synchronicity between the RF frequency and the revolution frequency of the electrons is crucial for optimal acceleration. Additionally, considerations such as the beam's energy spread, emittance, and dispersion play vital roles in characterizing the booster ring's performance.

In essence, the booster ring emerges as a transformative stage within the synchrotron particle accelerator, crucial for preparing the electron beam for the subsequent stages of exploration in the storage ring. Its operational parameters and intricate design contribute significantly to the overall efficiency and effectiveness of the accelerator architecture.

STORAGE RING

The storage ring (Figure C.1) stands as the centerpiece in the path of a synchrotron particle accelerator, constituting the final stage where high-energy electron beams traverse circular orbits, generating synchrotron radiation for diverse experimental applications. Its primary function involves maintaining the accelerated electron beams in a stable, closed trajectory, fostering prolonged interactions with inserted samples across various beamlines.

Key parameters defining the operation of the storage ring include the magnetic field strength, RF frequency, and lattice functions, such as beta (β) and emittance (ε). The beta function governs the beam's envelope, influencing its size at various locations along the ring, while emittance characterizes the spread of particle trajectories, affecting the beam's overall quality.

In essence, the storage ring represents the pinnacle of the synchrotron particle accelerator, where intricate design and precise control converge to facilitate prolonged and stable electron beam circulation. Its operational parameters, encompassing magnetic optics and RF systems, play a pivotal role in defining the quality and versatility of synchrotron radiation generated, establishing the storage ring as a cornerstone in the realm of high-energy particle exploration.

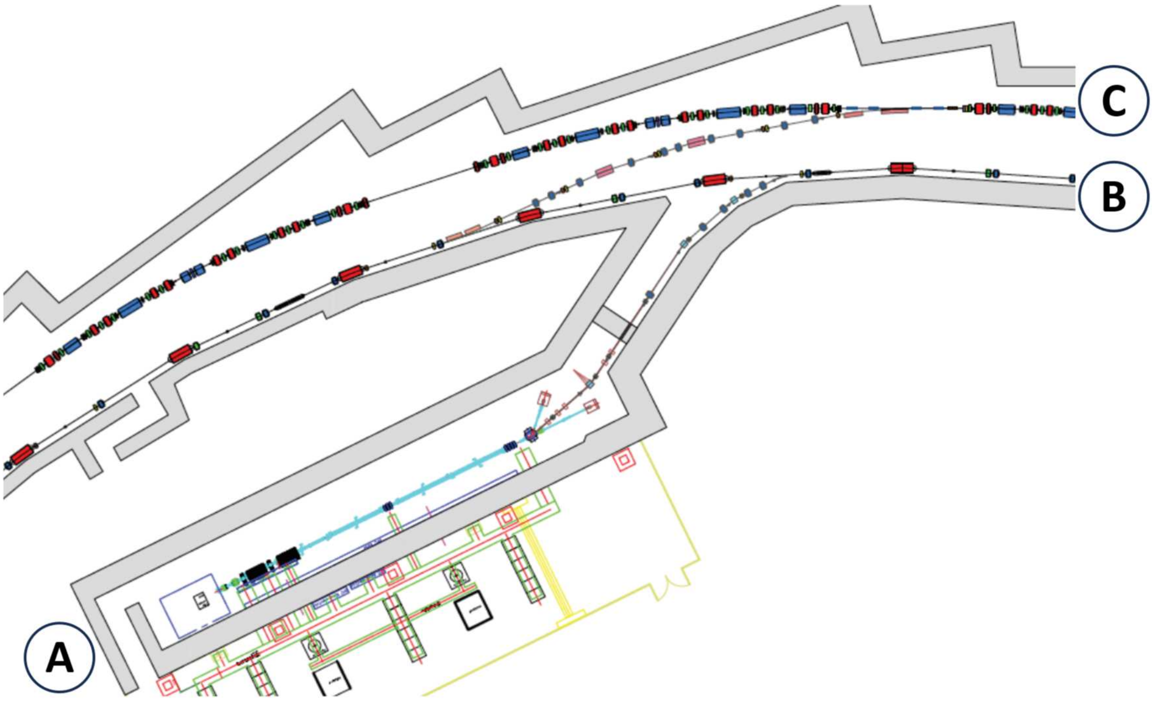

Figure C.1: Layout of Sirius injection system with a 150 MeV Linac (A) and a 3 GeV booster (B) in the same tunnel as the storage ring (C). Modified from: [4]

MAGNETIC LENS

Central to the functioning of the accelerator are magnetic lenses, which wield control over the trajectory of charged particles. These lenses, often comprising quadrupole and sextupole magnets, manipulate the beam's focusing and defocusing, ensuring its stability throughout the accelerator's components. The intricacies of these magnetic lenses necessitate stringent adherence to tolerance factors, defining the precision required in the fabrication and alignment of these components to guarantee optimal beam stability.

Quadrupole magnets serve as pivotal focusing devices, designed to concentrate electron trajectories in both horizontal and vertical planes. The strength of the magnetic field within the quadrupole, denoted by the gradient, is a critical parameter influencing the degree of focusing, with higher gradients leading to stronger focusing effects. Additionally, the focal length of the quadrupole, determined by the curvature of its magnetic field, plays a crucial role in shaping the trajectory of electrons. Sextupole magnets, as higher-order components, further refine the beam optics by addressing nonlinear effects induced by the quadrupoles. Parameters such as the sextupole strength and the resonance conditions are carefully tuned to correct chromatic aberrations and optimize beam stability. The intricate interplay of these magnetic lenses orchestrates the delicate dance of electrons, ensuring precise control over their trajectories within the accelerator.

Quadrupoles and sextupoles play a dual role in shaping the beam optics and mitigating inherent aberrations in the electron trajectories. The quadrupole's ability to focus in one plane and defocus in the perpendicular plane allows for the generation of a well-behaved beam, while sextupoles introduce corrective measures to enhance stability. The beta functions, representing the envelope of electron trajectories, are key parameters influenced by these magnetic lenses. By carefully adjusting the strengths and configurations of quadrupoles and sextupoles, researchers can tailor the beam's characteristics, optimizing conditions for advanced experiments across various beamlines. The precise manipulation of these magnetic optics is paramount for achieving high-quality synchrotron radiation and ensuring the success of diverse scientific investigations within the synchrotron particle accelerator. [155] [154]

C.3 Bending magnets and insertion devices

Synchrotron beamlines derive their exceptional brightness and intensity from accelerated charged particles, predominantly electrons, circulating within a storage ring. These particles are subject to powerful magnetic fields generated by specialized magnets, such as undulators and wigglers, strategically positioned along the storage ring. The interaction between the charged particles and these magnetic fields results in the emission of synchrotron radiation, a high-energy electromagnetic radiation with unique properties ideal for a myriad of scientific applications, as illustrated in Figure C.2.

The luminosity and intensity characteristics intrinsic to synchrotron beamlines are inherently rooted in the orchestrated interplay between accelerated charged particles, primarily electrons, circulating within a designated storage ring. This symbiotic relationship unfolds in the presence of specialized magnets strategically positioned along the storage ring, specifically undulators and wigglers.C.2 The ensuing interaction between these charged particles and the induced magnetic fields precipitates the emission of synchrotron radiation—an electromagnetic radiation of heightened energy and distinctive properties that render it eminently conducive to an array of scientific applications.

1. Bending Magnets: Inherent to the operational dynamics of synchrotron storage rings, bending magnets constitute an indispensable element tasked with sustaining the curved trajectory of charged particles. As electrons traverse these bending magnets, their trajectory undergoes curvature, eliciting the emission of synchrotron radiation tangentially to their course. Although bending magnets proffer a brilliance quotient comparably lower than that of undulators and wigglers, their role remains pivotal in the overall functionality of the beamline.

2. Wigglers: Paralleling undulators in function, wigglers also encompass arrays of magnets designed to induce transverse oscillations in the trajectory of charged particles. While analogous in their capacity to engender synchrotron radiation, wigglers distinguish themselves by generating spectra of broader bandwidth and heightened radiation intensity. This characteristic renders wigglers particularly efficacious in applications necessitating a heightened photon flux.

3. Undulators: Foremost among the sources of synchrotron radiation in contemporary beamlines are undulators. These intricate devices are characterized by arrays of magnets arranged in a periodic fashion, compelling electrons into a trajectory of oscillatory motion. The resultant alternating magnetic fields furnish the impetus for the emission of coherent and notably intense synchrotron radiation. Of particular significance is the tunability inherent in undulators, affording the generation of radiation across a broad and adjustable spectral range within a narrow band. This attribute renders undulators highly versatile for a multitude of experimental methodologies.

The adoption of a specific source type within a synchrotron beamline is contingent upon the particularized requisites governing the characteristics of the synchrotron beam, encompassing considerations of wavelength, flux, and coherence. Undulators and wigglers, with their tunable attributes and elevated brilliance, emerge as preferred choices amenable to a diverse spectrum of experimental endeavors. Conversely, bending magnets, while proffering a more continuous spectrum, play an integral role in the overarching operational paradigm of the synchrotron beamline. This discerning integration of diverse source typologies within the beamline framework underscores the capacity of researchers to tailor the emitted synchrotron radiation to align precisely with the exigencies inherent in a spectrum of scientific investigations across varied disciplines.

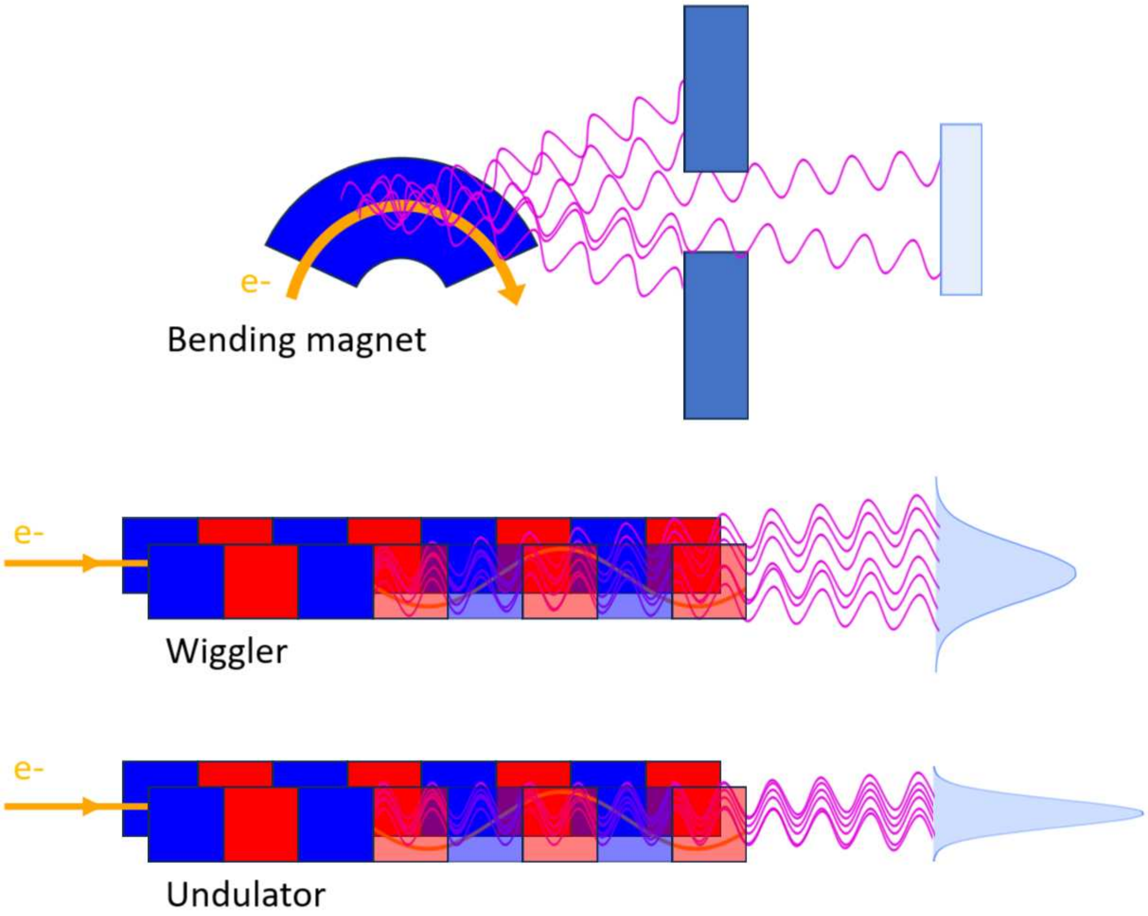

Figure C.2: Bending magnets and insertion devices. The magnets arrange are represented in blue and red for different poles. Orange lines are representative of the electrons path and the pink sinusoidal lines are the photons irradiated from the accelerated particles. The light purple profiles on the right represent the spatial distribution of the intensity generated in each kind of source.

C.4 Coherence

Coherence is the estimation of the capacity of two waves to undergo interference. During the process of interference, two waves sum themselves up, resulting in a wave with an amplitude greater than that of either individual wave (constructive interference). Alternatively, they may counteract each other, producing minima that could even reach zero (destructive interference), contingent upon their relative phase. It is essential to recognize that constructive and destructive interference represents extreme scenarios, and in all cases, two waves undergo interference, with the outcome potentially intricate or unremarkable.

Waves exhibiting a constant relative phase are named coherent. The quantification of coherence is often accomplished through interference visibility, which assesses the size of interference fringes concerning the input waves as the phase offset undergoes variation. And it is formally expressed by [156]:

$$\gamma(\vec{r}_1, \vec{r}_2) = \frac{\langle E^*(\vec{r}_1, t) E(\vec{r}_2, t) \rangle}{[I(\vec{r}_1) I(\vec{r}_2)]^{1/2}}$$

.

That is the normalization for the mutual optical intensity of the fields ($\vec{E}$) normalized by the square root of the product of its intensities (I), which measures the correlation between two points in space and time within the system's function. Consider two monochromatic waves with the same wavelength and a constant phase difference arriving at a detection plane. The resulting wave and measured intensity are functions of their phase relationship, indicating the degree of coherence.

C.5 Coherence Lengths

- **Temporal Coherence (Longitudinal):** Temporal coherence gauges the correlation of the beam's radiation along its propagation. The coherence length, represented by ξ_l, is the minimum distance for two wavefronts to transition from constructive to destructive interference. It is inversely proportional to energy resolution.

  $$\xi_l = \frac{\lambda^2}{2\Delta\lambda}$$

  This implies that a highly coherent beam demands a high energy resolution.

- **Spatial Coherence (Transverse):** Spatial coherence measures correlation in the transverse directions to the beam's propagation. The coherence length, ξ_t, is the minimum distance for destructive interference between wavefronts emitted by different points in a finite-sized source.

$$\xi_t = \frac{\lambda R}{2w}$$

The degree of coherence depends on the source size and the distance from the source, with a decrease in source size being a common solution for achieving highly coherent sources.

These coherence lengths (Figure C.3) play a crucial role in experimental setups, determining the quality of interference and influencing factors such as energy resolution, source size, and distance from the source. Achieving and maintaining high coherence often involves sophisticated instrumentation and precision optics. The main variables to define the coherence lengths are λ, the walength of the light, and $\Delta\lambda$, the energy resolution of the beam, and w, the size of its source. R is the distance between the source and the plane in which the coherence length is being calculated.

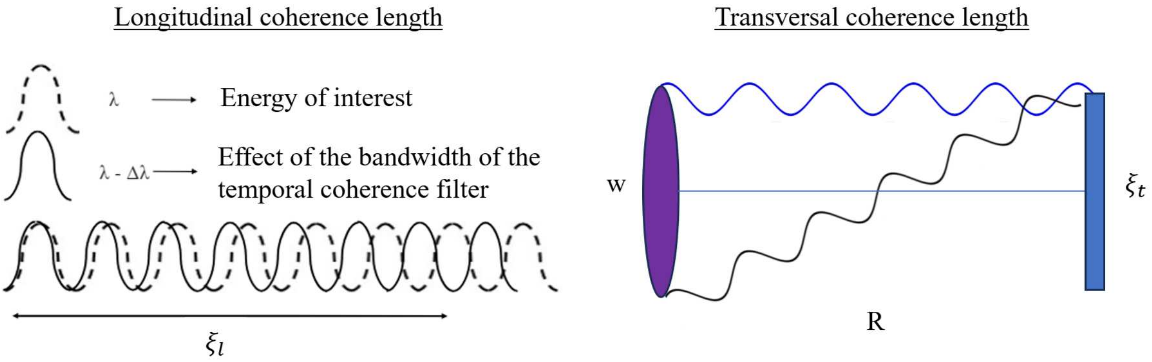

Figure C.3: Illustration of the definition of the longitudinal and transversal coherence lengths.

C.6 Synchrotron beamlines

Optical components within the beamline structure play an instrumental role in shaping and refining the synchrotron beam. Mirrors and monochromators, strategically positioned along the beamline, serve to focus, collimate, and select specific wavelengths or energy ranges, thereby affording researchers precise control over experimental parameters. [157] [158] [159] [160]

Experimental stations, situated at the terminus of the beamline, emerge as the crucible for scientific inquiry. Equipped with an array of specialized instruments and detectors, these stations cater to diverse experimental techniques, encompassing X-ray diffraction, X-ray absorption spectroscopy, X-ray fluorescence, and beyond. These stations represent the nexus where theoretical concepts materialize into empirical exploration, facilitating a broad spectrum of analyses and investigations across scientific disciplines.

A critical facet of beamline operation lies in the real-time monitoring and control of the X-ray beam position. X-ray Beam Position Monitors (XBPM) provide invaluable feedback, ensuring meticulous alignment and positioning with micrometer-level precision. [59] [62] This granular control over beam positioning is indispensable for achieving optimal experimental conditions and enhancing the reliability of scientific observations. [3]

The integration of a Kirkpatrick-Baez (KB) mirror system further refines the X-ray beam, facilitating high spatial resolution at the sample position. Monochromators [61], integral to beamline functionality, afford the selection of monochromatic X-rays, pivotal for experiments necessitating specific energy ranges. This judicious combination of mirror systems and monochromators embodies a meticulous design strategy aimed at tailoring the synchrotron beam to the precise requirements of diverse scientific investigations. [161] [162]

Sample environments within the beamline infrastructure accommodate the imposition of controlled conditions, such as temperature, pressure, and gas environments. This feature enables researchers to engage in in situ and operando studies, broadening the scope of scientific investigation. The adaptability of sample environments underscores the beamline's versatility, allowing for the exploration of diverse materials and phenomena under conditions that simulate real-world scenarios. [14] [3] [163] [73]

Detectors, ranging from CCD cameras to energy-dispersive detectors, serve as vigilant recorders of signals emanating from X-ray interactions with samples. These detectors form an integral component in the data acquisition process, capturing nuanced information for subsequent analysis. Their sensitivity and precision contribute to the fidelity of experimental results, playing a pivotal role in the generation of high-quality datasets for scientific interpretation. [164] [165] [166]

The overarching control systems govern the orchestration of beamline components, allowing for dynamic optimization of experimental parameters, seamless transitions between techniques, and the collection of high-fidelity data. [3] [161] [167] [59] Concurrently, sophisticated data analysis and visualization tools empower researchers to distill meaningful insights from the wealth of information garnered during experiments. This collaborative interplay between automated control systems and advanced data processing tools enhances the efficiency and efficacy of scientific investigations conducted at synchrotron beamlines.

APPENDIX D

FLUORESCENCE ENERGIES AND LIMITS OF INTEGRATION

Fluorescence emission lines								
A.N.	Element	Edge (eV)	Emission (eV)			Excitation (eV)	Initial (eV)	Final (eV)
82	Pb	2484 (M5)	2345			7000	2100	2500
53	I	4557 (L3)	3937	3926	4220	10000	3850	4100
55	Cs	5012 (L3)	4286	4272	4620	10000	4500	4800
82	Pb	13035 (L3)	10551	10450	12613	14000	10200	10800
35	Br	13474 (L3)	11924	11877	13291	14000	11800	12200

Table D.1: Fluorescence emission lines and initial and final values for energy ROIs integration.

APPENDIX E

LATTICE PARAMETER CALCULATION AND RECIPROCAL SPACE MODELLING

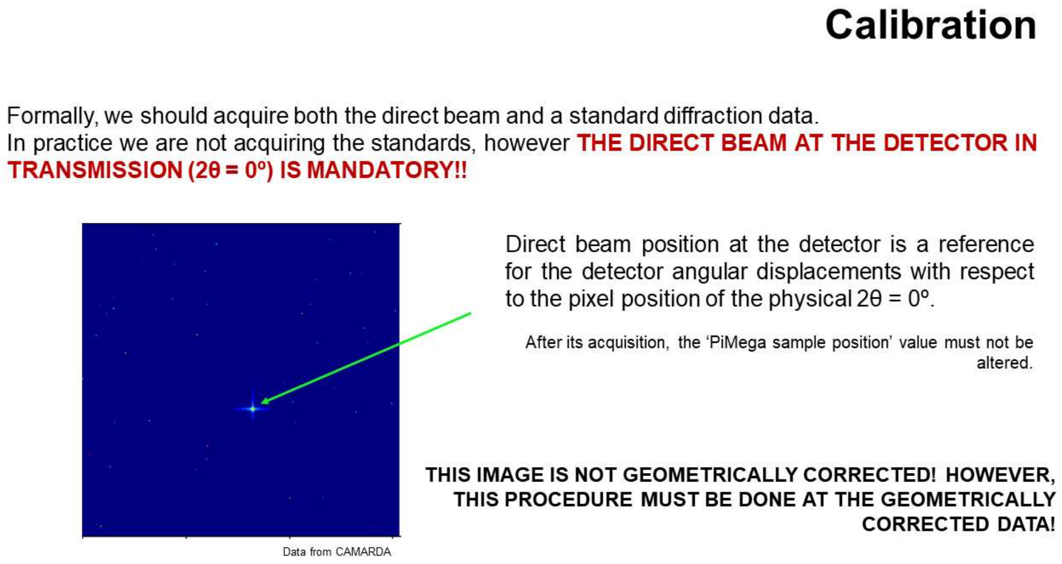

Calibration

Formally, we should acquire both the direct beam and a standard diffraction data.
In practice we are not acquiring the standards, however **THE DIRECT BEAM AT THE DETECTOR IN TRANSMISSION (2θ = 0º) IS MANDATORY!!**

Direct beam position at the detector is a reference for the detector angular displacements with respect to the pixel position of the physical 2θ = 0º.

After its acquisition, the 'PiMega sample position' value must not be altered.

THIS IMAGE IS NOT GEOMETRICALLY CORRECTED! HOWEVER, THIS PROCEDURE MUST BE DONE AT THE GEOMETRICALLY CORRECTED DATA!

Data from CAMARDA

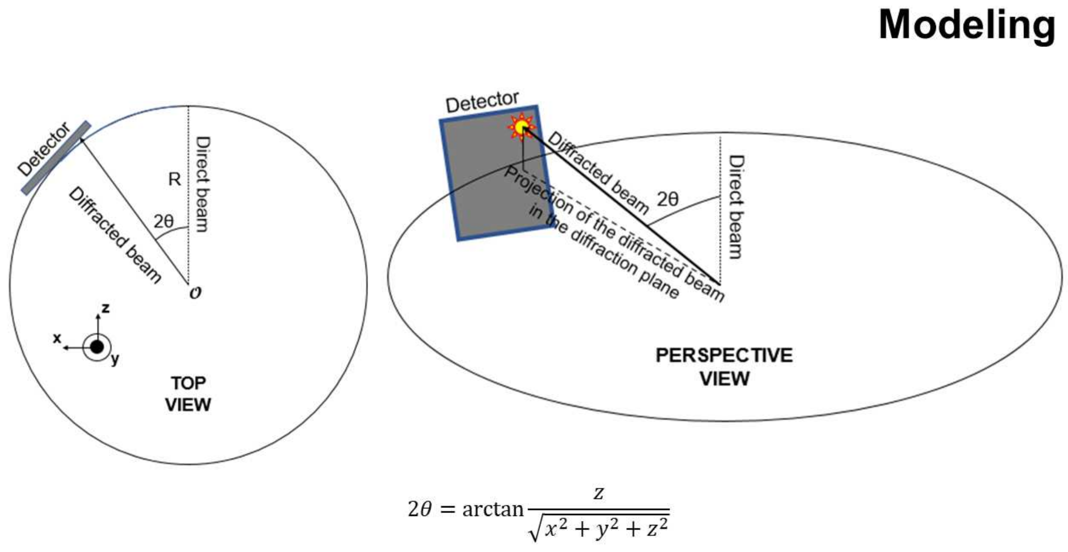

Modeling

$$2\theta = \arctan\frac{z}{\sqrt{x^2+y^2+z^2}}$$

Methodology - Modeling

We map the position of each pixel of the geometrically corrected pixel in the detector in the real and reciprocal pace

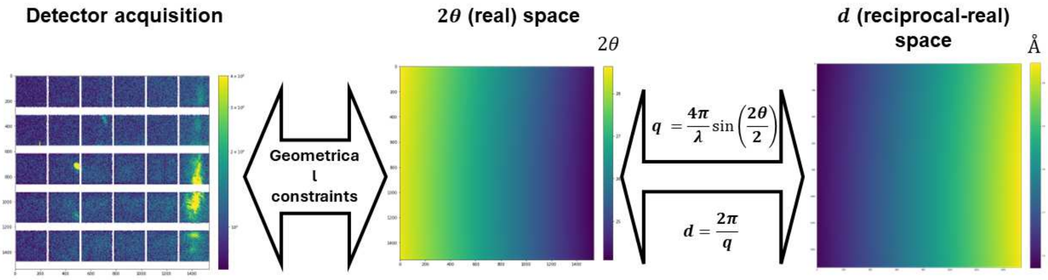

Detector acquisition

2θ (real) space

d (reciprocal-real) space

Geometrical constraints

$$q = \frac{4\pi}{\lambda}\sin\left(\frac{2\theta}{2}\right)$$

$$d = \frac{2\pi}{q}$$

Data analysis - Diffractogram

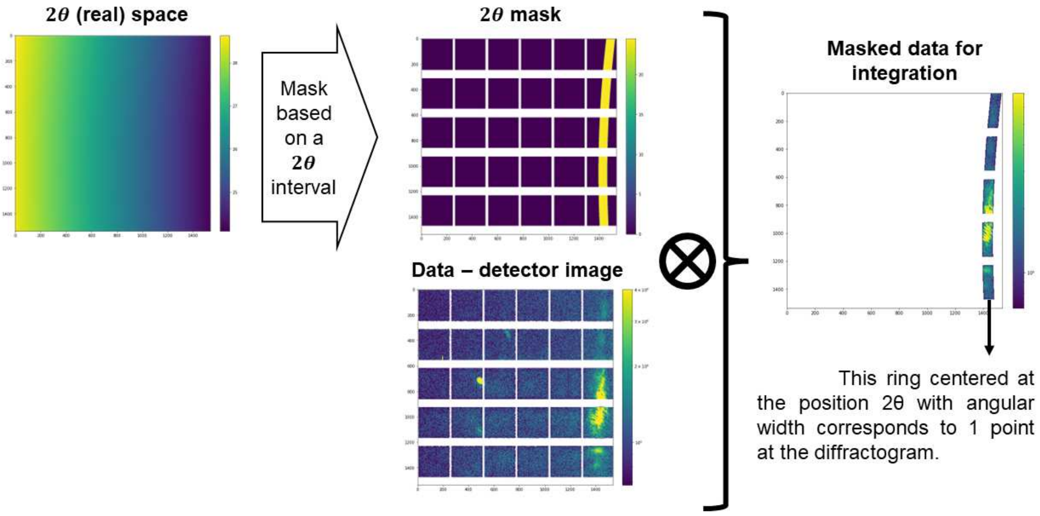

2θ (real) space

Mask based on a 2θ interval

2θ mask

Data – detector image

$\otimes$

Masked data for integration

This ring centered at the position 2θ with angular width corresponds to 1 point at the diffractogram.

Data analysis - Diffractogram

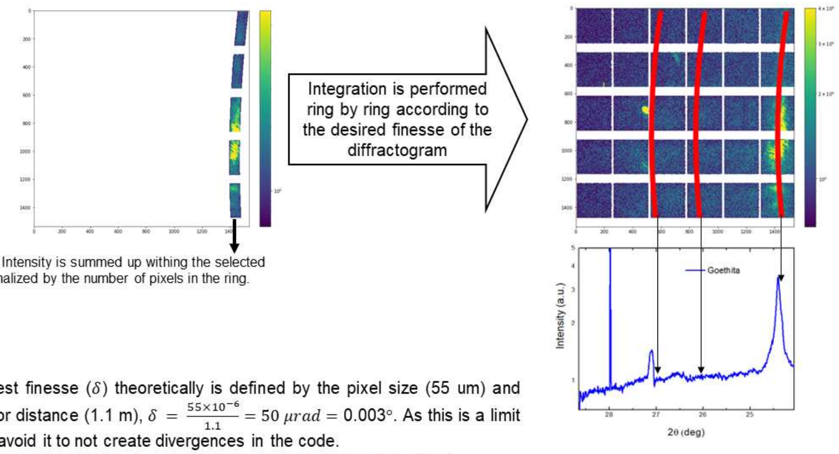

Integration is performed ring by ring according to the desired finesse of the diffractogram

Intensity is summed up withing the selected ring and normalized by the number of pixels in the ring.

The smallest finesse (δ) theoretically is defined by the pixel size (55 um) and the detector distance (1.1 m), $\delta = \frac{55\times10^{-6}}{1.1} = 50\ \mu rad =$ 0.003°. As this is a limit value, we avoid it to not create divergences in the code.
A typical good value for δ is $\delta = 0.008°$ (2 to 3 pixels for the ring width).

Data analysis – Intensity map

The total intensity in the detector is calculated and the value is then reshaped for a map with the correspondent size and coordinates of each point corresponding to a pixel, whose value is the total intensity

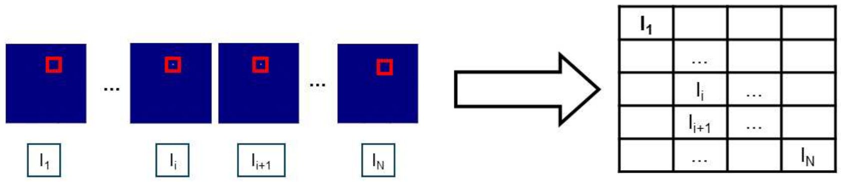

The same procedure can be done with a ROI at the detector! It is interesting when more than one family of reflections or different phases scatter at the same angular range captured by the detector!

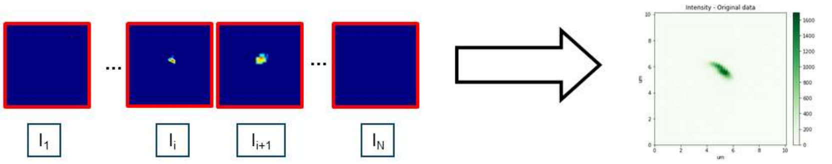

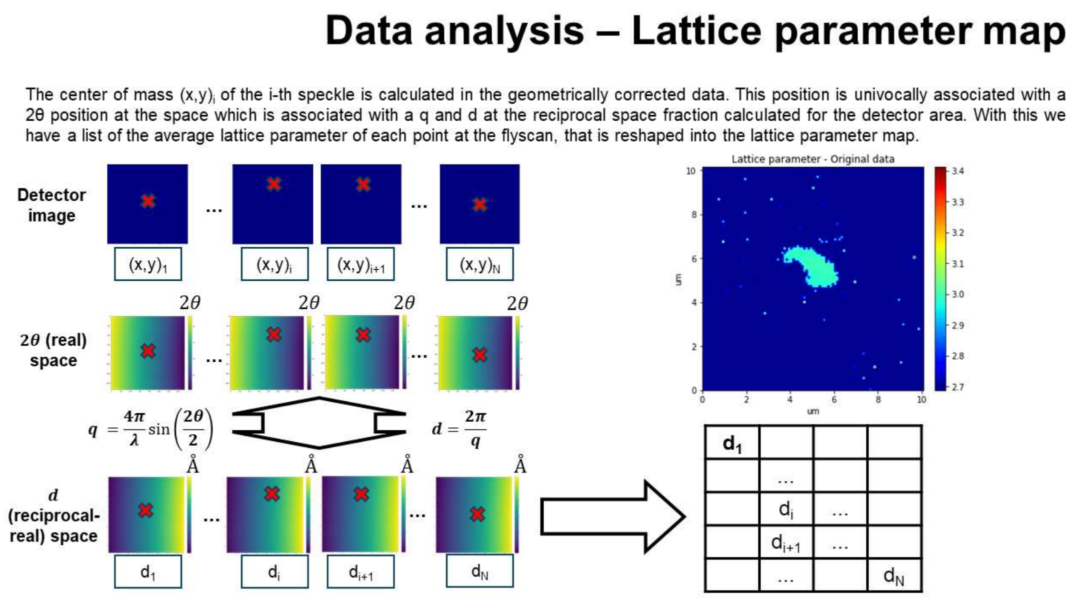

Data analysis – Lattice parameter map

The center of mass $(x,y)_i$ of the i-th speckle is calculated in the geometrically corrected data. This position is univocally associated with a 2θ position at the space which is associated with a q and d at the reciprocal space fraction calculated for the detector area. With this we have a list of the average lattice parameter of each point at the flyscan, that is reshaped into the lattice parameter map.

$$q = \frac{4\pi}{\lambda}\sin\left(\frac{2\theta}{2}\right) \qquad d = \frac{2\pi}{q}$$

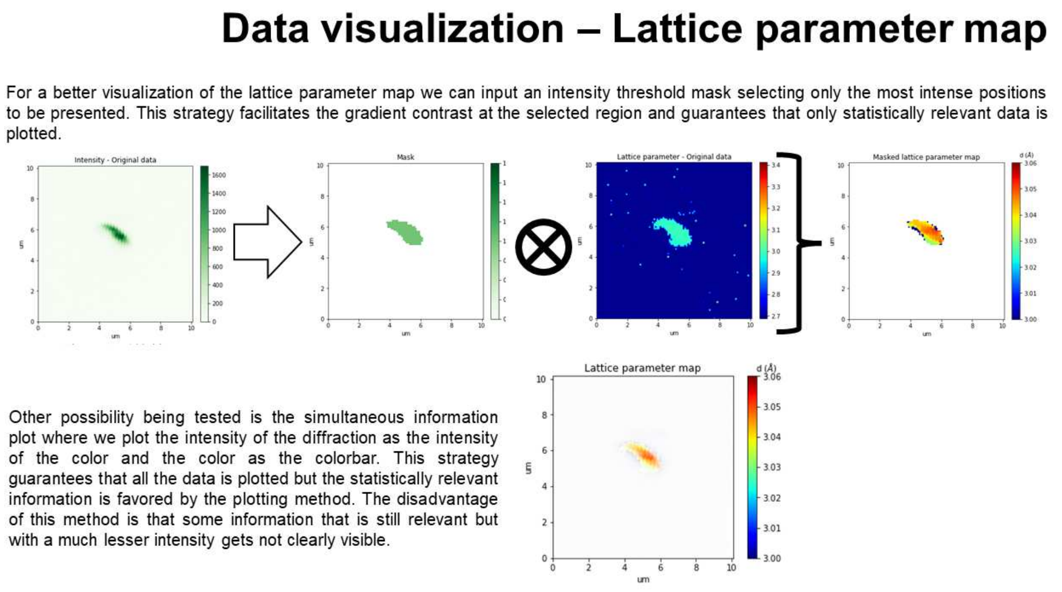

Data visualization – Lattice parameter map

For a better visualization of the lattice parameter map we can input an intensity threshold mask selecting only the most intense positions to be presented. This strategy facilitates the gradient contrast at the selected region and guarantees that only statistically relevant data is plotted.

Other possibility being tested is the simultaneous information plot where we plot the intensity of the diffraction as the intensity of the color and the color as the colorbar. This strategy guarantees that all the data is plotted but the statistically relevant information is favored by the plotting method. The disadvantage of this method is that some information that is still relevant but with a much lesser intensity gets not clearly visible.

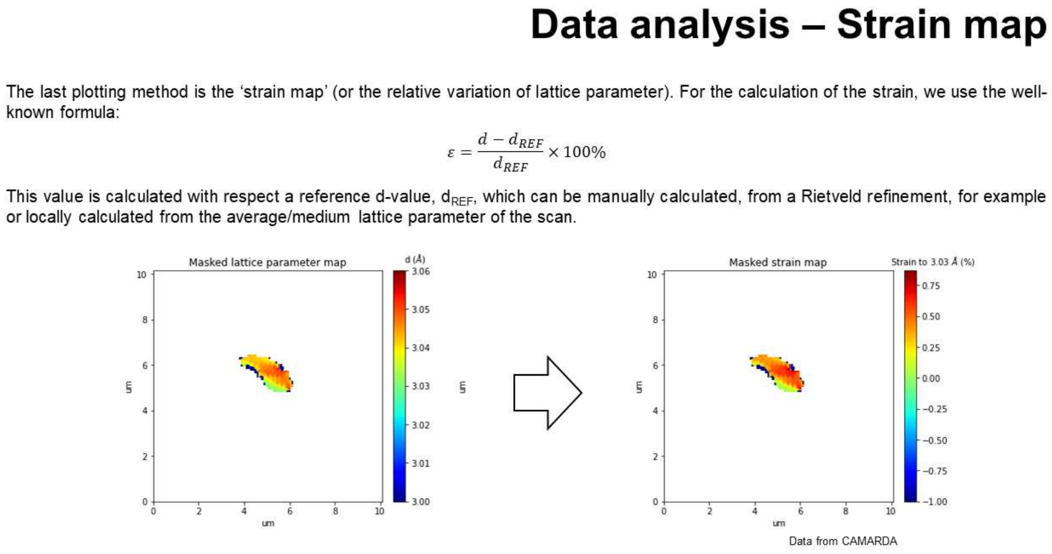

Data analysis – Strain map

The last plotting method is the ‘strain map’ (or the relative variation of lattice parameter). For the calculation of the strain, we use the well-known formula:

$$\varepsilon = \frac{d - d_{REF}}{d_{REF}} \times 100\%$$

This value is calculated with respect a reference d-value, d_{REF}, which can be manually calculated, from a Rietveld refinement, for example or locally calculated from the average/medium lattice parameter of the scan.

Data from CAMARDA

APPENDIX F

RECIPROCAL SPACE MODEL CODE

Listing F.1: Reciprocal space mapping

```
'''
Inputs:
    - Data: Stacking of the area detector acquisition in the first
       axis
    - energy: Energy value in keV
    - dThU: Nominal position of the detector in 2Theta
    - PhiU: Nominal position of the detector in the azimuthal angle
    - x, y: Pixel coordinates of the direct beam at the 0deg
       position
    - distance_det: detector distance in meters
    - pixel_size: pixel size of the detector in meters
Returns:
    - dThN: 2Theta space covered by the detector
    - Phi: Azimuthal angle space covered by the detector
    - q_map: q space covered by the detector
    - d_map: d space covered by the detector
'''

def dTh2d(dTh, energy=None, wl = None):
    return(q2d(dTh2q(dTh,energy, wl)));

def dTh2q(dTh, energy=9.75, wl = None):
    if wl == None:
        wl = 12.398425/energy;

v = np.array([distance_det * np.sin(np.deg2rad(dThU)) *
   np.cos(np.deg2rad(PhiU)), distance_det *
   np.sin(np.deg2rad(PhiU)), distance_det *
   np.cos(np.deg2rad(dThU)) * np.cos(np.deg2rad(PhiU))]);

        map_k = np.zeros((Data.shape[1], Data.shape[2], 3), dtype
```

```
           = float);
        dThN = np.zeros((Data.shape[1], Data.shape[2]), dtype =
           float);
        PhiN = np.zeros((Data.shape[1], Data.shape[2]), dtype =
           float);

        for i in range(map_k.shape[0]):
            for j in range(map_k.shape[1]):
                map_k[i,j,0] = v[0] + (x-j) * pixel_size *
                   np.cos(np.deg2rad(dThU));
                map_k[i,j,1] = v[1] - (y-i) * pixel_size;
                map_k[i,j,2] = v[2] - (x-j) * pixel_size *
                   np.sin(np.deg2rad(dThU));
                dThN[i,j] = np.rad2deg(np.arccos((map_k[i,j,2])/
                np.sqrt((map_k[i,j,0])**2 + (map_k[i,j,1])**2 +
                   (map_k[i,j,2])**2)));
                PhiN[i,j] = np.rad2deg(np.arctan(-(map_k[i,j,1])/
                (map_k[i,j,0])));

        q_map = dTh2q(dThN,energy=energy);
        d_map = dTh2d(dThN,energy=energy);
```

APPENDIX G

DOSE CALCULATION

Listing G.1: Dose calculation

```python

from xraydb import material_mu
from xraydb import atomic_mass
import numpy as np

###-------------------- input ----------------------
# Perovskite composition
Cs = 0.4
FA = 0.6
MA = 0.0
Pb = 1
Br = 1.14
I = 1.86

cubic_latt_par = 6.22 # In angustron
#I0 = 2.21e23 #photons/s
I0 = 5.35e9 #photons/s
t = np.array([135, 410, 150, 610, 172, 60]) # s
A = (50e-6*50e-6)  #m
#A = 500e-9*200e-9
E = 10000  # Energy eV

# --------------------------------------------------
formula_1 = "Cs" + str(Cs) + "FA" + str(FA) + "MA" + str(MA) +
   "Pb" + str(Pb) + "I" + str(I) + "Br" + str(Br)
print("The␣perovskite␣formula␣is:␣", formula_1)

mass_sum_FA = atomic_mass("C")+ 5*atomic_mass("H")+
   2*atomic_mass("N")
mass_sum_MA = atomic_mass("C")+ 6*atomic_mass("H")+
   atomic_mass("N")
```

```
mass_sum = (Cs*atomic_mass("Cs")) + (FA*mass_sum_FA) + (MA*mass_sum_MA)+ (Pb*atomic_mass("Pb")) + (I*atomic_mass("I")) + (Br*atomic_mass("I"))

cell_vol = (cubic_latt_par*1e-10)**3  #meters

density = (mass_sum/(cell_vol*6.02214e23))/1e6

C = round(FA+MA, 2)
N = round((2*FA)+MA, 2)
H = round((5*FA)+(6*MA), 2)

formula = "Cs" + str(Cs) + "C" + str(C) + "N" + str(N) + "H" + str(H) + "Pb" + str(Pb) + "I" + str(I) + "Br" + str(Br)
print("The␣elemental␣perovskite␣formula␣is:␣", formula)
print("Density␣is", round(density,2) , "g/cm3")

mu = material_mu(formula , energy = E, density = density)
print(mu)

#D = (((I0*t)/A)*(mu/density)*E*1.6021e-19)/10  #Wihtout unit convertion
D = ((I0*t)/A)*((mu*1e2)/(density*1e3))*E*1.6021e-19 # convert cm-1 to m-1 and g/cm3 to Kg/m3
F = ((I0*t)/A)*(mu*1e2)/(density*1e3)
print(F)

for n in range(len(D)):
    print("Dose␣=␣", ’{:.2e}’.format(D[n]), "Gy")
    print("Flux␣=␣", ’{:.2e}’.format(F[n]), "Gy")

d = 400

print("Mass", (density*1e3)*A*(d*1e-9))
print(’Volume’, A*(d*1e-9))
print(mass_sum)
```

APPENDIX H

NANODIFFRACTION PEAKS

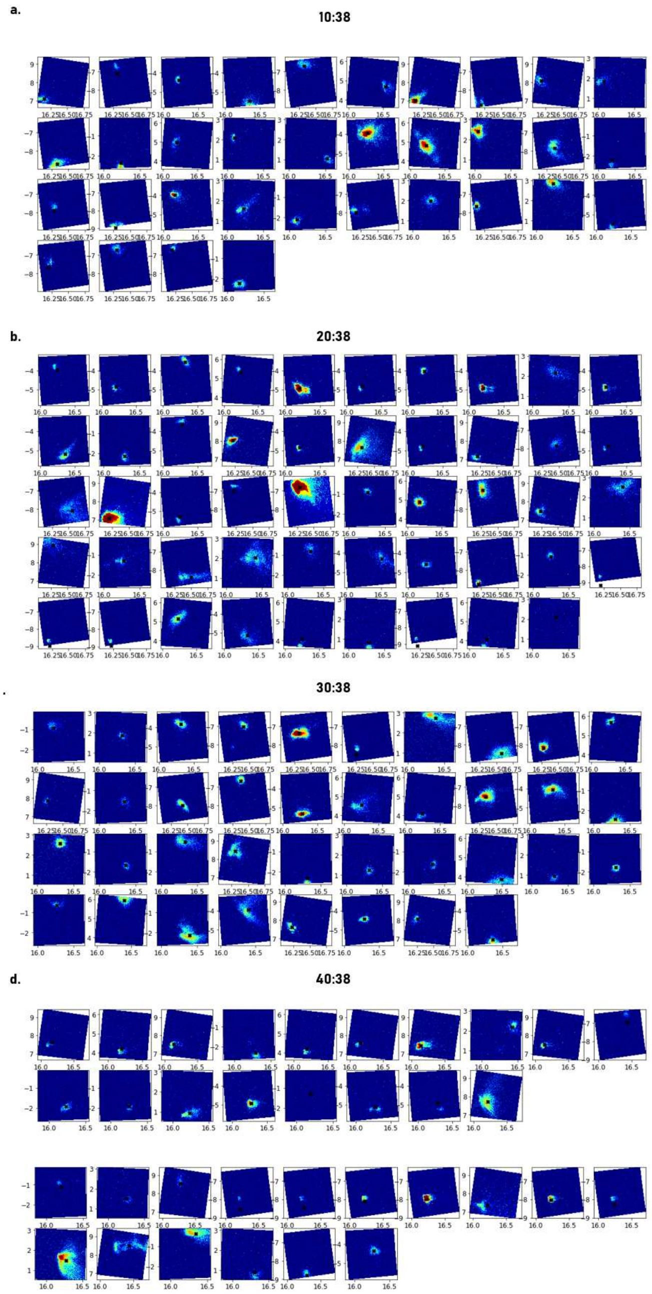

Figure H.1: Collection of the diffraction peaks for the nanodiffraction maps

APPENDIX I

RESOLUTION CRITERIA

In Fourier Ring Correlation (FRC) analysis, the 1/2-bit criterion and the 1-bit criterion are methods for determining the resolution limit of a reconstructed image or map. These criteria are defined based on the point at which the FRC curve drops to a certain threshold value, and they are commonly used to objectively quantify the spatial resolution. Here's an explanation of each:

- 1/2-**Bit Criterion:** - The 1/2-bit criterion refers to the point on the FRC curve where the correlation drops to 0.5 or 50% of its maximum value. This criterion indicates a resolution where the two independent datasets used in the analysis are considered to be resolved from each other.
- 1-**Bit Criterion:** - The 1-bit criterion is more stringent than the 1/2-bit criterion. It refers to the point on the FRC curve where the correlation drops to $1/\sqrt{2}$ or approximately 0.707. This criterion is chosen because it corresponds to the point at which two independent datasets are just statistically distinguishable from each other.

Comparison:

The 1/2-bit criterion tends to be less conservative than the 1-bit criterion. It represents a resolution limit where the two datasets are partially distinguishable, while the 1-bit criterion is a stricter threshold indicating a higher level of confidence in the resolution.

Choosing between the two criteria may depend on the specific requirements of the study and the desired level of stringency in defining resolution. In practice, the 1-bit criterion is often considered a more robust measure of resolution, especially in cases where high confidence in the separation of features is crucial.

Both criteria provide a standardized way to communicate the resolution of reconstructed images, enabling researchers to compare results and assess the quality of their structural data.

APPENDIX J

STATISTICAL APPROACH FOR LUMINESCENCE MAPS ANALYSIS

XEOL and cathodeluminescence maps performed at the samples were studied with statistical approachs in order to spatially separate the components of the luminescence excited by both x-rays and electrons. For that is was used the the CORAL library [168] that plays a pivotal role in employing techniques like Multivariate Curve Resolution with Alternating Least Squares (MCR-ALS) [169] and Principal Component Analysis (PCA) [170]. These techniques prove instrumental in separating components within XEOL and CL spectra acquired in step scan mode, providing insights into the complex interplay of luminescent features and their correlations with varying experimental conditions and spatial distribution. CORAL library, through its robust tools, contributes to unraveling the complexity of spectral data, offering a deeper understanding of materials response under investigation.

Figure J.1 summarizes the results of the minimization for the XEOL maps presented in Figure 5.6 from Chapter 5. For the results the worst decomposition with 2 components reach the figures of merit of Fitting error in % at optimum: 15.50 [PCA] and 21.45 [EXP], with variance explained (R^2) at optimum of 95.40. The choice of 2 components was led by the clear wrinkle-to-valley transition in the luminescence response of the material. Attempts with 3, 4 and 5 components were performed, but their results were not satisfactory (over-fitted). The 2 simmetric components separation separated all 4 sample in two main regions, perfectly correlated to the winkle morphology: one component more intense with redshifted emission surrounded by a less intense more energetic component. An exception rises for 40:38 which presents an asymmetry in both components a assimetry due to a second gaussian in higher energy (center at 1.82 eV for Comp0 and Comp1). The attempts to separate this third gaussian as a third component were not successful.

The separation of the spectra in two components strongly correlated to the different regions of the morphology corroborates the conclusion that morphology dominates the main variations in the optical-electronic response of the materials. The interpretation of the result components are, as expected, the consequence of the halide proportions variation from one to other region of the morphology of the material, in which the lesser quantity of the material in the valley regions with a higher proportion of Br with respect to Pb causes a blueshifted emission with lesser intensity. And the opposite for the regions with accumulation of matter, which is stoichiometrically poorer in Br.

No normalization were performed in the data before the MCR-ALS treatment.

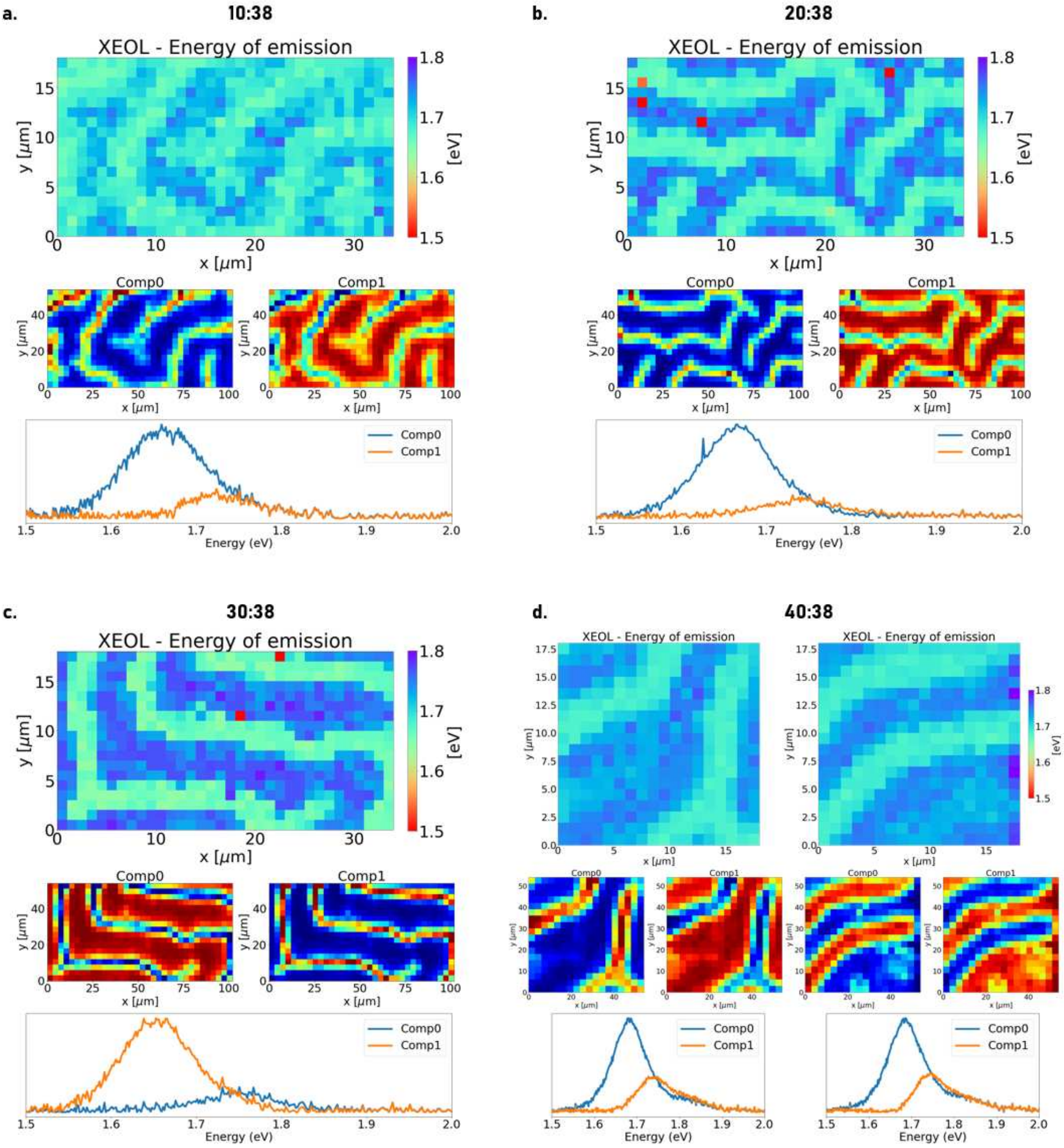

Figure J.1: MCR-ALS and PCA approach for XEOL components in XEOL maps for samples (a) 10:38, (b) 20:38, (c) 30:38 and (d) 40:38.

Similar observations follow for the cathodoluminescence set of data. The results from the minimization for the CL maps presented in Figure A.8 from Chapter A are shown in Figure J.2. For the results the worst decomposition with 2 components reach the figures of merit of Fitting error in % at optimum: 17.20 [PCA] and 24.15 [EXP], with variance explained (R^2) at optimum of 91.00.

For CL maps, the decomposition in two components also presented the best figures of merit, and led to similar conclusions to the XEOL data. Spatially the components are strongly correlated to the wrinkled morphology. The result components in this case are presented normalized, however, their intensities still follow the same tendency of the ones showed previously for the XEOL. The positions for the components in XEOL and CL minimizations are in agreement.

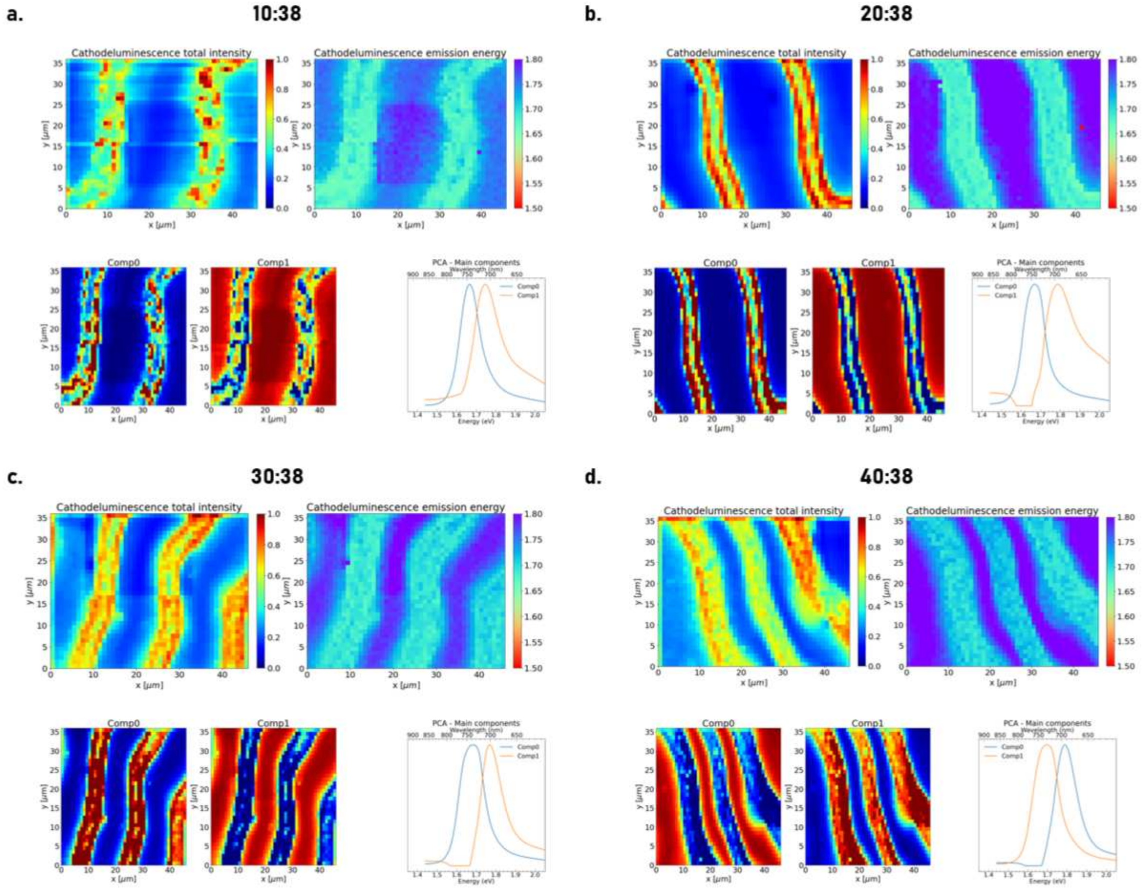

Figure J.2: MCR-ALS and PCA approach for CL components in CL maps for samples (a) 10:38, (b) 20:38, (c) 30:38 and (d) 40:38.

Investigation about the influence of different procedures for data normalization are still to be investigated.

For both XEOL and CL maps, the decomposition into two components yields the best results, showcasing strong correlations with the wrinkled morphology. The normalized results for CL maps follow similar tendencies observed in XEOL, indicating consistency in luminescent behavior between the two techniques. The spatial correlation of components with morphology reaffirms that variations in luminescence are intricately linked to the structural features of the material.

In conclusion, the integration of statistical approaches, facilitated by the CORAL library, coupled with MCR-ALS and PCA techniques, offers a systematic and robust means to explore and interpret the spatial distribution of luminescent components in Cs-rich perovskites, shedding light on the complex interplay between material morphology and optical-electronic response.